UNIVERSITÀ DEGLI STUDI DI ROMA "TOR VERGATA"

FACOLTÀ DI SCIENZE MATEMATICHE, FISICHE E NATURALI

DOTTORATO DI RICERCA IN FISICA
XXII CICLO

X-ray Absorption Spectroscopy: a powerful tool for structural studies of molecules involved in the pathogenesis of neurodegenerative diseases

Francesco Stellato

Docente Guida: Prof. Silvia Morante

Coordinatore: Prof. Piergiorgio Picozza

Contents

Preface

Just like XX century was dubbed the century of Physics, the XXI one is often claimed to be the century of Biology. It is in fact undeniable that the strong relationships already existing between the two disciplines are daily, and proficuously, increasing.

The work presented in this thesis is a good example of the fertile interaction between Physics and Biology. It is dealing with the application of X-ray Absorption Spectroscopy (XAS) to the study of the structure of certain proteins and peptides, related to severe neurodegenerative diseases - Creutzfeldt-Jakob, Alzheimer and Parkinson - and of their interaction with metals.

The material of this thesis is organized as follows. Chapter 1 is devoted to the description of the main biophysical and medical issues related to the systems studied in this work. Chapter 2 is about the theoretical basis and the main experimental aspects of the XAS technique. A special attention is devoted to the data analysis methods. Chapter 3 is focused on the description of the experimental results on the prion protein, β-amyloid and neuromelanin and of their interpretation. Finally in Chapter 4 I report the application of XAS to prolidase (a protein related to the insurgence of a very rare, fatal disease) the structure of which is also influenced by its interaction with metals. Conclusions summarizing the main results of the thesis and describing possible future perspectives are given in Chapter 5.

All the work presented in the thesis has been done within the Biophysics group in the University of Rome 'Tor Vergata' lead by Prof. Silvia Morante. Besides Prof. Morante, I would like to thank Prof. Giancarlo Rossi and Dr. Velia Minicozzi for

their scientific and practical support. Among the former group members I would like to thank Dr. Francesco Guerrieri and Dr.Stefania Alleva.

Chapter 1

The molecular basis of neurodegenerative diseases

Neurodegenerative diseases (a composite word from Greek $\nu\epsilon\upsilon\rho$o, "nerval" and Latin *degenerare*, "to decline") are a class of pathologies which affect the brain. Many of them are age related, therefore in a society in which population is getting older and older it is a very important issue to find effective therapies against them. The molecular basis of this class of pathologies is in many cases still unclear. However it is worth noticing how diseases with very different etiology show common molecular mechanisms, such as protein misfolding and aggregation processes.

This chapter starts with a short overview of neurodegenerative diseases, with particular attention to the role played in their pathogenesis by protein misfolding processes. Then it follows a more detailed description of the pathologies that are the main subject of the thesis, namely Alzheimer's disease, the spongiform encephalopathies and Parkinson's disease.

1.1 What is a protein?

Proteins are essential components of a living organism. They participate in almost every process within cells and can have several functions. Many proteins are enzymes, i.e. molecules that catalyze biochemical reactions, but they can also have structural or mechanical functions, or play roles in cell signaling and immune responses [1].

From a structural point of view, proteins are organic polymers made of a linear chain of amino acidic monomers. The most common amino acids are 20. They share a common structure (the main chain) to which a variable (one for each amino acid) side chain is bound (see upper panel in Fig. 1.1). To help the further reading, in Table 1.1, the complete names of all aminoacids and their 3- and 1-letter codes are reported. The sequence of amino acids in a protein is determined by the sequence of nucleotides in the DNA (the gene), which is transferred to the mRNA (traduction process) and then from mRNA into the peptidic sequence (translation process).

Proteins are polymeric chains in which amino acids are joined together through a peptide bond between the carboxyl and amino groups belonging to two adjacent amino acid residues (see lower panel in Fig. 1.1). The sequence of amino acids along the chain is called 'primary structure' of the protein.

After their synthesis, proteins can undergo post-translational modifications, which consists of attaching other biochemical functional groups such as acetate, phosphate, various lipids and carbohydrates, or of the creation of structural changes, like the formation of disulfide bridges between Cysteine residues.

Due to the differences in the side chains, each amino acid has different physical and chemical properties. In particular, there are charged and neutral residues, polar and non-polar side chains. An important property strictly connected to this last feature is the hydropathicity, namely the preference for the side chain of being in a polar or non polar medium.

The local arrangement of the amino acidic chain is usually characterized by regularly repeating structures (secondary structure), the most common of which are the α helix and the β sheet.

The overall shape of a single protein molecule, which is strictly related to its func-

Amino Acid	3-Letter Code	1-Letter Code
Alanine	Ala	A
Arginine	Arg	R
Asparagine	Asn	N
Aspartic Acid	Asp	D
Cysteine	Cys	C
Glutamic Acid	Glu	E
Glutamine	Gln	Q
Glycine	Gly	G
Histidine	His	H
Isoleucine	Ile	I
Leucine	Asn	L
Lysine	Lys	K
Methionine	Met	M
Phenylalanine	Phe	F
Proline	Pro	P
Serine	Ser	S
Threonine	Thr	T
Tryptophan	Trp	W
Tyrosine	Tyr	Y
Valine	Val	V

Table 1.1: The 20 Amino Acids: names, 3 and 1 letter abbreviations.

tion, is the tertiary structure. Proteins composed by more subunits have also an higher, quaternary, level of structure, which depends on the relative positions of non-covalently bound peptidic subunits.

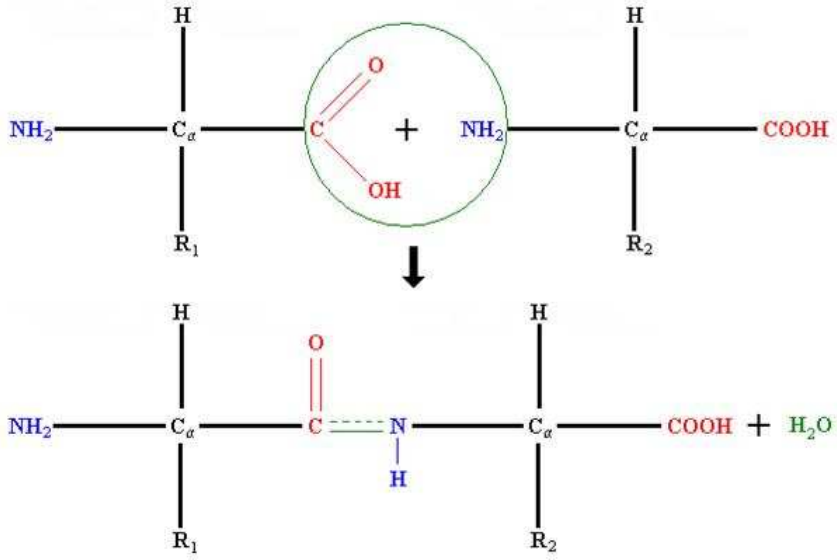

Figure 1.1: Amino Acid structure and peptide bond. R_n is the side chain that is characteristic of a given amino acidic residue.

1.2 Protein Misfolding and Neurodegenerative Diseases

It is well established that the function of a protein is strictly related to its structure. In the 1950s Anfisen showed, in a series of now classical experiments, that protein folding depends only on the aminoacidic sequence of the molecule (the so-called primary structure)[1]. This is true for an isolated proteic molecule, but in a real case the situation is more complicated, because the correct folding can be influenced and guided by several factors, such as the pH, the presence of other biomolecules, membranes or metal ions [4].
Protein folding is indeed a very complicated process, that not always ends with the 'right' three-dimensional configuration. Being protein function strictly related to its folding, it is straightforwardly understood how errors in the folding can be at the basis of pathologies. The class of diseases in which alterations in protein folding are observed is composed of about 20 pathologies (see their list in Table 1.2). They are known as Protein Conformational Disorders (PCDs) [5].

Through the folding and unfolding processes specific types of cellular activity

Disease	Fibril subunit
Alzheimer's Disease	Amyloid β peptide
Spongiform encephalopathies	Full-length prion protein
Hereditary cerebral haemorrhage	Amyloid β peptide, cystatin C
Type II diabetes	Amylin
Medullary carcinoma of the thyroid	Procalcitonin
Atrial amyloidoses	Atrial natriuretic factor
Parkinson's Disease	α synuclein
Huntingtons Disease	Glutamine
Amyotrophic lateral sclerosis	Superoxide dismutase
Primary systemic amyloidosis	Immunoglobulin light chains
Secondary systemic amyloidosis	Serum amyloid A protein
Familial Mediterranean fever	Serum amyloid A protein
Familial amyloidotic polyneuropathy 1	Mutant transthoracic
Senile systemic amyloidosis	Wild-type transthyretin
Familial amyloidotic polyneuropathy II	Apolipoprotein A-1
Haemodialysis-related amyloidosis	β2-Microglobulin
Finnish hereditary amyloidosis	Mutant gelsolin
Lysozyme amyloidosis	Mutant lysozyme
Insulin-related amyloid	Insulin
Fibrinogen α-chain amyloidosis	Fibrinogen α-chain

Table 1.2: Most common PCDs.

are generated or suppressed. Failure to correctly fold, or to remain correctly folded, will therefore give rise to the malfunctioning of living systems and hence to disease [6]. There are two main mechanism through which misfolding may affect protein function: the first one consists of directly impeding protein correct functioning, like in cystic fibrosis and some types of cancer; the second one is by giving to incorrectly folded proteins a high propensity to misfold and thus to form aggregates within cells or (more commonly) in extracellular space. Fig. 1.2 shows a schematic picture of the possible pathogenetic pathway.

Several disorders in which normally soluble proteins accumulate in the extracel-

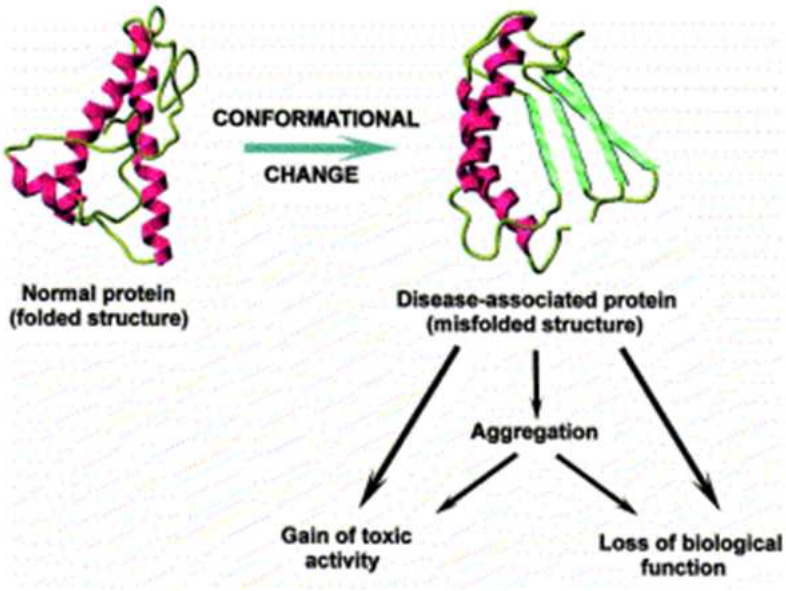

Figure 1.2: Conformational changes related pathogenetic mechanisms.

lular space of various tissues as insoluble deposits have been identified, and they are known as amyloidoses. It is worth noticing that, although the amino acidic sequence of the proteins that are the main component of the deposits are completely different in each amyloidosis, the disorders have several key features in common. In particular, amyloid deposits have characteristic optical properties, such as birefringence, on binding certain dye molecules such as Congo red. The aggregates have peculiar morphologies, as shown by X-ray diffraction patterns which indicate the presence of fibrils of about 10 nm diameter. These fibrils are rich in β sheet conformation, and the peptide strands are arranged perpendicular to the long axis of the fibre (Fig. 1.3).

Of particular significance is the finding that globular proteins with diverse sequences that are not currently associated with a protein-folding disease can undergo aggregation *in vitro* into fibrils indistinguishable from those found in the amyloidoses, thus suggesting that aggregation into β sheet rich fibrils is a generic property of polypeptide chains regardless of sequence.

Protein misfolding is thought to be connected to age-dependent neurodegeneration. During the past two decades, the pathogenesis of age related degenerations of the brain has become recognized as likely to be mediated by the progressive

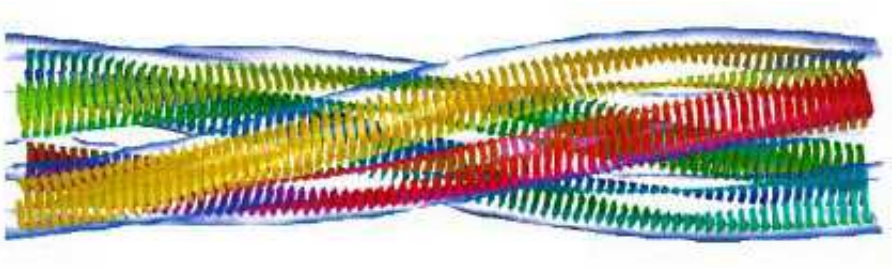

Figure 1.3: Sketch of an amyloid fibril with peptide strands perpendicular to its long axis.

accumulation of β sheet rich protein aggregates. The most common neurodegenerative disease, Alzheimer, is the main example of this mechanism.
The second most common, Parkinson disease, is increasingly considered to involve a protein-folding problem. For this reason, researches focused on understanding the mechanisms at the basis of protein misfolding and aggregation have become of great scientific, biomedical, social and economical interest.

1.3 Alzheimer's Disease and Aβ Peptides

In 1906 Alois Alzheimer gave a lecture at a congress in Tübingen, Germany, on the first case of the disease that Kraepelin some years later named Alzheimer's disease (AD). In that single case, Alzheimer described typical clinical characteristics with memory disturbances and instrumental signs, and the neuropathological picture with miliary bodies (plaques) and dense bundles of fibrils (tangles), which today are considered the hallmarks of the disease [7].

Nowadays, AD is defined as an irreversible, progressive, neurodegenerative disorder clinically characterized by memory loss and cognitive decline with impaired activities of daily living and a range of behavioral and psychological symptoms. It is the most common form of dementia, accounting for 50-60% of all cases. Dementia is indeed a generic term that describes chronic or progressive dysfunction of cortical and subcortical function that results in complex cognitive decline. These cognitive changes are commonly accompanied by disturbances of mood, behavior, and personality. A distinction is often made between primary degenerative dementias such as AD, dementia with Lewy bodies, frontotemporal dementia, and dementia secondary to another disease process, such as AIDS dementia.

AD shows an almost exponential increase with age, so that in people aged 85 years or older the prevalence is between 24% and 33% in the western world (see Fig. 1.4 for United States statistics). AD is thus very common and it is becoming

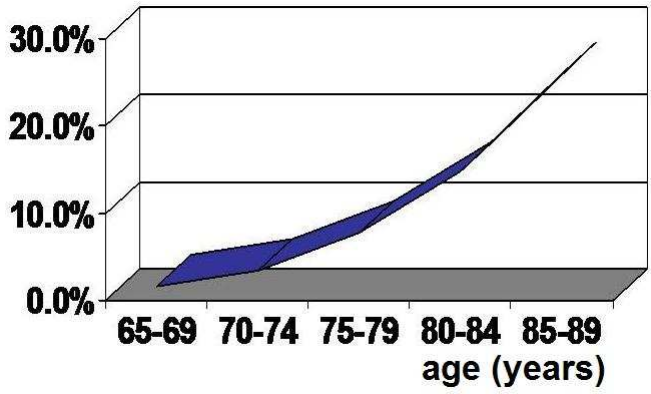

Figure 1.4: Percentage of U.S. population diagnosed with AD, versus age.

one of the major public health problems.

Besides ageing, which is the main risk factor for the disease, epidemiological studies have suggested several further tentative associations. Some can be linked to a decreased reserve capacity of the brain, including reduced brain size, low educational and occupational attainment, low mental ability in early life, and reduced mental and physical activity during late life. The brain reserve capacity is determined by the number of neurons and their synaptic and dendritic arborization together with lifestyle-related cognitive strategies. Brain reserve can not only influence the incidence of the pathology, but also modulate the brain response to it.
Finally, it is worth recalling that the AD overall pathogenetic mechanism is still unknown, and that no effective therapies are up to now available.

1.3.1 Physiology and Pathology of AD

At a microscopic level, AD brains show two peculiar lesions, namely senile (or neuritic) plaques and neurofibrillary tangles, which are mainly found in the medial temporal lobe structures and cortical areas of the brain. These alterations can also be found in the brain of old people who do not show any symptom of the disease, but in AD patients they are definitely more relevant than in these people.
The two lesions may also occur independently one from the other. In particular, there are people who clearly show the symptoms of AD and have many neuritic plaques, but few or no neurofibrillary tangles. This last form of pathology development is characterized by a different kind of intra-neuronal inclusion, the Lewy body, and it is therefore known as Lewy variant of AD.

-Neuritic Plaques
Neuritic plaques contain extracellular deposits of amyloid-β peptide (Aβ) that occur principally in a filamentous form, i.e. as star-shaped masses of amyloid fibrils [8]. Electron microscopy studies (see Fig. 1.5) have shown that the fibrils in the plaques are 4-8 nm in diameter and are composed of 2-4 nm long filaments. X-ray fiber diffraction has recognized a β sheet structure with repeat distance in the fibers of 4.8 and 10.6 Å. The finding that exists a correlation between plaque

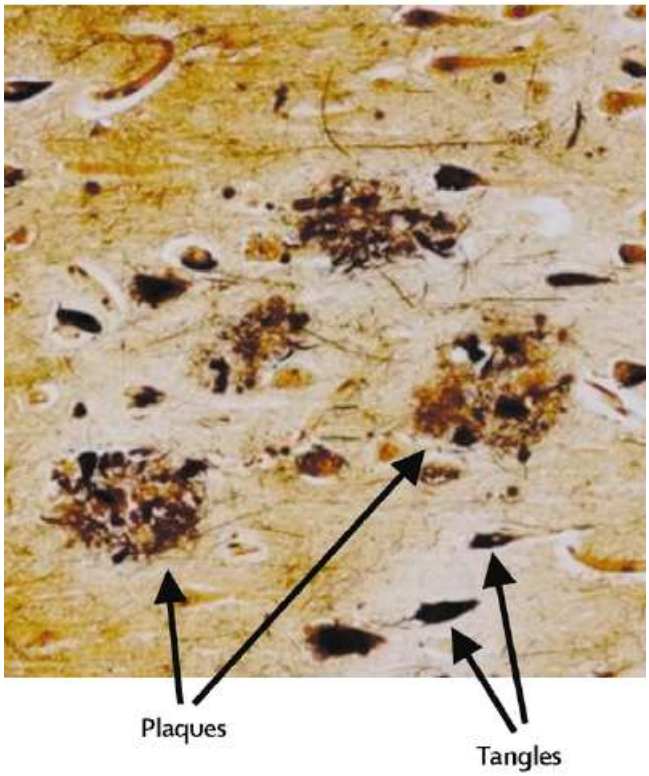

Figure 1.5: Plaques and tangles in the cerebral cortex of an AD patient. Plaques are extracellular deposits of Aβ surrounded by dystrophic neurites, reactive astrocytes, and microglia, whereas tangles are intracellular aggregates composed of a hyperphosphorylated form of the microtubule-associated protein τ [7].

amount and dementia severity strongly suggested the involvement of plaques in the pathogenesis of the disease.

The Aβ peptide found in senile plaques was initially thought to be an abnormal protein, but in 1992 it was discovered [9] that it is produced during normal cell metabolism. The Aβ is originated from the proteolytic cleavage of a long transmembrane protein, the so-called amyloid precursor protein (APP). APP is highly conserved in evolution and it is expressed in all mammals in the genome of which it is codified. In humans, APP is coded in chromosome 21.

The overall function of APP is unclear; however, it is believed to be important during the development of the Central Nervous System (CNS) and in response to stress or injury [10]. APP is a heterogeneous group of ubiquitously expressed

polypeptides mainly found in 3 isoforms of 695, 751, and 770 residues originated by alternative splicing. The APP splice forms containing 751 or 770 aminoacids are widely expressed in non-neuronal cells throughout the body, while the 695 form is mainly expressed in neurons.

The APP is cleaved by the proteolytic enzymes (or enzymatic complexes) α, β and γ secretases. As shown in Fig. 1.6, when the cut is operated by the α and γ secretases the non pathological peptide P3 is originated, while when it is operated by β and γ secretases Aβ peptides of different length are originated. The protein BACE (β site APP cleaving enzyme) has been identified as β secretase, while the γ secretase is a multiprotein complex consisting of presenilin, nicastrin, Aph-1, and Pen-2, with presenilin containing the two catalytic aspartates that mediate peptide bond scission [14].

The major component of amyloid plaques associated with AD are the Aβ(1-40) and Aβ(1-42), although also other forms of the peptide (Aβ(1-39) and Aβ(1-43)) have been sometimes observed. It has been shown that the Aβ(1-40) fibrils consist of dimeric units of Aβ stacked as in crossed β-sheets. Fibrils of Aβ(1-42) have an identical structure except that the two monomers that make up the dimeric propagating unit of the fibril are shifted relative to each other by two residues [13].

The hypothetic pathogenic mechanisms associated to $A\beta$ peptides is known as amyloid cascade theory [15]. It proposes that Aβ is protein junk that spontaneously self-aggregates into amyloid fibrils that are somehow neurotoxic and cause dementia. The self-aggregation hypothesis leaves unanswered important questions about the biology of AD, e.g. it does not explain why does Aβ, which is ubiquitous, precipitate only in the neocortex and why rats and mice, unlike other mammalian species, do not develop Aβ neuropathology with advancing age.

As pointed out in more details in paragraph 1.3.4, some answers to these questions can be given by studying the metallochemical properties of Aβ, that is possibly connected with the neurobiology of metal ions metabolism in the brain. An important point that has still to be clarified is whether the amyloid plaques are one of the causes of AD or just its byproduct. It has been proposed indeed that Aβ oligomers are the proper pathogenetic agents, because they are known to

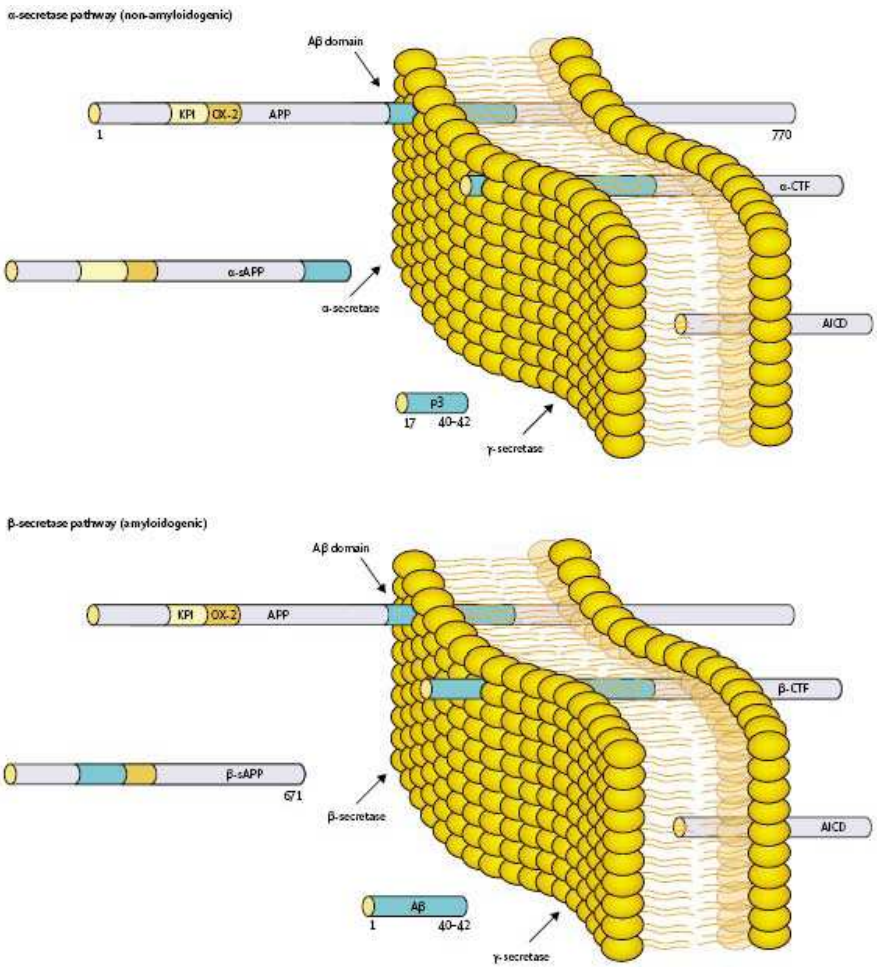

Figure 1.6: Metabolism of APP with Aβ generation [7].

inhibit hippocampal long-term potentiation and disrupt synaptic plasticity [7]. It has been also suggested that Aβ oligomers composed of no more than 12 Aβ peptides are related to memory disturbances in AD transgenic mice. This idea has been somehow confirmed by the work of Shankar *et al.*[11], who extracted soluble Aβ oligomers directly from the cerebral cortex of subjects with AD. They show that Aβ oligomers, dimers in particular, are significantly correlated with AD symptoms, while insoluble amyloid plaque cores from AD cortex do not have pathological effects unless they are first solubilized to release Aβ dimers, thus suggesting that plaque cores are inactive, but they sequester Aβ dimers that are synaptotoxic.

-Neurofibrillary Tangles

Neurofibrillary tangles are the second class of lesions characteristic of AD. They are composed of abnormally hyperphosphorylated τ protein. τ is a normal axonal protein that binds to microtubules through its microtubule-binding domains. τ phosphorylation is regulated by balancing multiple kinases and phosphates, and in AD patients the equilibrium of this process is found to be shifted toward an higher phosphorylation degree with respect to the healthy subjects. The process starts intracellularly and leads to sequestration of normal τ and other microtubule-associated proteins. Phosphorylated τ also becomes prone to aggregation into insoluble fibrils in tangles, further compromising neuronal function. Anyway, it is still unclear whether τ hyperphosphorylation and tangle formation are a cause or consequence of AD.

Genetics and Risk Factors

From a genetic point of view, AD is a heterogeneous disorder with both familial and sporadic forms. Familial AD is a rare autosomal dominant disorder with onset before 65 years. The first identified mutations causing the familial form of the disease are located in the APP gene on chromosome 21[12]. It has been observed that the overexpression of structurally normal APP due to the Down's syndrome trisomy of chromosome 21 almost invariably leads to the premature, during middle adult years, occurrence of classical AD neuropathology. However Down's patients develop their first diffuse plaques at the end of the first or the beginning of the second decade of life and yet do not show full-blown AD histopathology until the end of the third or fourth decade. The study of AD development in these subjects could therefore help to obtain dynamic information about the disease cascade and understand the sequence of pathogenic events in the disorder [8].

However, APP mutations explain only a few familial cases, instead mutations in the presenilin genes (PSEN1 and PSEN2) account for most cases of familial disease. More than 160 different missense mutations have been identified within these two presenilin genes that cause an aggressive, early-onset form of AD, largely by producing longer and thus more aggregation prone species of Aβ.

The sporadic form of AD as well has been shown to have a significant genetic background. In particular, a study based on twins showed that heritability for the sporadic form is around 80%. In 1993 an association between the apolipoprotein E $\epsilon 4$ allele and AD was reported. This allele increases the risk of the disease by 3 times in heterozygotes and by 15 times in homozygotes. The apolipoprotein E is a cholesterol transporter in the brain, and the $\epsilon 4$ allele is less efficient than other variants in reuse of membrane lipids and neuronal repair. In addition, apolipoprotein E is essential for the deposition of Aβ peptide, promoting its fibrilization and plaques formation.
Besides genetic causes, there are some risk factors which have been demonstrated to increase the risk of developing AD. Epidemiological studies have demonstrated that risk factors for AD include age, sex (females are at greater risk), head injury and cardiovascular and cerebrovascular diseases. The link between cerebrovascular pathology and AD is clearly demonstrated in the case of cerebral amyloid angiopathy (CAA)[16], where deposition of Aβ in the vascular media and adventitia leads to loss of integrity of the vessel wall with resulting brain hemorrhages. CAA is also recognized as a cause of brain ischemia and cognitive impairment independent of stroke. Moreover, experimental data show that soluble Aβ can cause vascular reactivity in the absence of vascular deposition or vessel wall dysfunction and suggest that vascular dysfunction can be an early step in Aβ diseases and could even precede significant Aβ deposition.

1.3.2 Diagnostic and Therapeutic Strategies in AD

The first problem in AD therapy is the diagnosis, which is still mainly based on the clinical assessment of patients, as diagnostic markers remain elusive. Standard criteria are used to determine the diagnosis of AD, which can be established at 3 different levels of certainty (definite AD, probable AD and possible AD). The clinical diagnostic accuracy for AD depends on the stage of disease and can overcome 90% in mid or late stages.
Laboratory techniques are also widely used to help in the AD diagnosis. In particular, neuroradiology plays an important role in the investigation, because it allows to exclude alternative causes of dementia. Another useful technique is

magnetic resonance imaging (MRI), which has been used to examine atrophy of brain regions which are more affected by AD, such as temporo-mesial cortical regions, entorhinal cortex, perirhinal cortex, hippocampus and amygdala. However, the low sensitivity of MRI makes it unsuitable to perform early diagnosis of degenerative disease.
Also Positron Emission Tomography (PET) has revealed a powerful tool in detecting early stages of the disease. In particular, PET images acquired using the so-called Pittsburgh Compound-B allowed to obtain an *in vivo* detection of the amyloid plaques formations [17] (see Fig. 1.7).

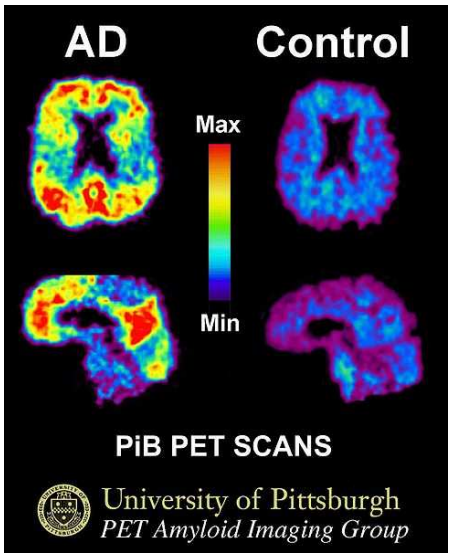

Figure 1.7: PET image showing amyloid plaques concentration in healthy and AD brain.

Once the AD diagnosis is made, the physiopathology of the disease suggests to try a few different therapeutic strategies. From a physiological point of view, AD is associated to a deficit in neurotransmission systems [18]. In particular, in the '70 it was observed that there is a strong decrease (60%-90%) in acetyl-cholintransferase in the cerebral cortex and in the hippocampus in AD patients. Acetyl-cholintransferase is an enzyme indispensable to the nervous system, because it catalyzes the synthesis of acetylcholine, which is an important neurotransmitter. The presence of cholinergic deficit in AD suggested the administration of acetylcholine precursors to improve the overall mental state of

patients, but the tests did not lead to significant results.
However still today the only somehow effective AD therapy is based on the acetylcholinesterase inhibitors that, decreasing the acetylcholine catabolism, increase its biodisposability. Due to its strong side effect, acetylcholine can not be directly administrated. In any case, this drugs class increases the cognitive behavior and slows down the AD evolution, but it is not able to completely remove the symptoms nor to stop the pathology evolution. In addition, the effect of these drugs lasts for few months, and about one half of the treated patients does not have any improvement.
Other strategies have therefore to be developed. Possible targets can be the Aβ peptides and the τ protein, which are both involved in the development and progression of AD. However, pharmacological strategies directed at these targets have not yet proven to be able to modify the disease evolution in human studies. In particular, in large-scale clinical trials no correlations have been found between a reduction in amyloid burden and improvement in cognitive functions. AD therapy is presently moving in various directions. Here below a short list of the main strategies nowadays followed is given [19]:
1: Administration of drugs able to inhibit the $A\beta$ synthesis by decreasing, without blocking, β and γ secretases activities. This approach is found to be successful mainly in the first stage of the pathology, namely with patients with low cognitive disorders.
2: An alternative strategy under study consists of administrating drugs which bind $A\beta$ monomers, thus preventing their aggregation and the formation of potentially toxic complexes. This approach requires a better understanding of the behavior of $A\beta$ peptides alone and in association with the drugs. In particular, metastable oligomers formation, which are thought to be more dangerous than fibrils, has to be avoided. The great advantage of this strategy is that its target is a purely pathologic event, therefore it does not interfere with the normal metabolic reactions catalyzed by β and γ secretases.
3: Administration of drugs which protect neurons from $A\beta$ accumulation effects. The problem in this case is that the $A\beta-$neurons interaction mechanisms are still unclear, so it is difficult to act on them without causing strong collateral effects on neuronal cells.

4: Metal ions levels are significantly elevated in AD patients' brain, and it has been demonstrated that APP is able to bind zinc and copper, that may influence Aβ aggregation level and associated toxicity. Therefore therapies based on the administration of metal chelators, i.e. of molecules that bind strongly to metal ions converting them into an inert form and decreasing the total pool of bioavailable metals, is used. Tests made with Al, Cu, Fe and Zn chelators have shown that these molecules are indeed able to slow down the cognitive decline [20]. It has been also suggested that different metal ions can play different roles in the pathogenesis of AD. In particular, Crouch *et al.* [21] have shown that increased Cu bioavailability inhibits Aβ oligomers and τ phosphorylation.
5: τ aggregation inhibitors. Hyperphosphorylation of the microtubule-associated $\tau-$protein is likely to result from an imbalance in kinase and phosphatases activities, and leads to destabilization of microtubules, loss of neuronal cytoskeletal architecture and/or plasticity, impaired neuronal transport, dystrophy and ultimately neuronal cell death. Based on these findings, small molecules that interfere with the formation of τ-aggregates, selectively inhibit $\tau-$kinases and/or activate $\tau-$phosphatases are being pursued as therapeutic targets

1.3.3 Sequence and Structure of Aβ Peptide

As recalled in section 1.1, a peptidic sequence is characterized by three (or four) structural levels. In the following, details are given about primary and secondary structure of $A\beta$ peptides.

-Primary Structure:
The primary structure of the Aβ peptide in the 42 aminoacids form is the following

1——————— 11——————— 21——————— 31——————— 41
DAEFRHDSGY EVHHQKLVFF AEDVGSNKGA IIGLMVGGVV IA

There are six negatively charged residues (D1, E3, D7, E11, E22, D23) and three positively charged ones (R5, K16, D23), yielding a net charge of -3. The long

hydrophobic tail (G29-V40) considerably reduces the solubility and enhances membrane adhesion.

An interesting analysis of the primary structure consists in looking at the hydropathicity profile of the peptide (Fig. 1.8), because it provides information on its aggregation tendency, being hydrophobic peptides more prone to aggregation in aqueous solution. In the case under analysis, there are two hydrophilic regions, namely (1-16) and (22-28), while the C-terminal region (29-42) is highly hydrophobic. The presence of this latter region is one of the causes of Aβ aggregation propensity in physiological conditions.

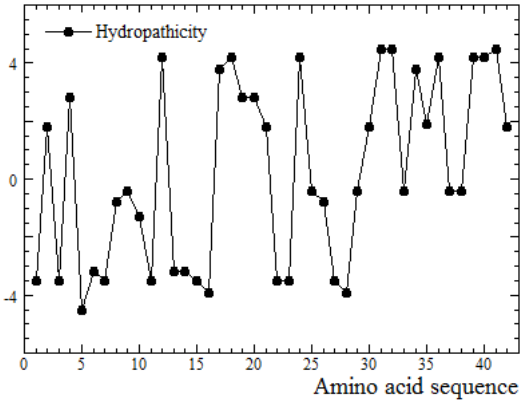

Figure 1.8: Aβ hydropathicity profile. Hydropathicity values reported here are calculated as the differences between the hydropathicity of the considered residue and that of glycine. Glycine is used as a standard because it has the smallest side chain (which consists of a single O atom) and its hydropathicity is therefore due essentially only to the main chain. Positive values indicate therefore a residue more hydrophobic than glycine, while negative ones a residue more hydrophilic than glycine.

-Secondary Structure:

The secondary structure is strictly related to the peptide behavior in solution, e.g. to its aggregation propensity and to the structure of possible aggregates. In particular, amyloid fibrils are composed by aggregates of Aβ peptide in β sheet secondary structure.

Different techniques, mainly Circular Dichroism (CD) and Fourier Transform Infrared spectroscopy (FTIR), have been applied to study the Aβ secondary

structure in different conditions, both *in vivo* and *in vitro*. In particular two regions, (10-20) and (29-42) have been identified where the structure is a β sheet. The study of Aβ fragments of different length is therefore useful in order to understand the role played by each region in the aggregation process. Many examples are provided in the following sections.

1.3.4 Interaction of Aβ Peptide with Metal Ions

A very important step in understanding the behavior of $A\beta$ peptides in physiological conditions is the study of their interactions with metal ions. The transition metal ions Cu^{2+}, Fe^{3+} and Zn^{2+} are present at total dry weight concentrations of 70, 340, and 350 μM, respectively, in the neocortical parenchyma of healthy brain [22], but it has been observed in 1998 [23] that senile plaques associated with AD contain higher concentration of these metal ions, in particular 0.4 mM Cu^{2+}, 1 mM Fe^{3+} and 1 mM Zn^{2+}, thus suggesting a severe unbalance in their homeostasis.

A recent work by Miller *et al.* [24] has used synchrotron FTIR to image the in situ secondary structure of the amyloid plaques in brain tissue of AD patients and synchrotron X-ray fluorescence (SXRF) microprobe to measure the metal ions concentration in the same sample. The authors observed that there is a strong spatial correlation between elevated β-sheet content in Aβ plaques and accumulated Cu and Zn ions, thus showing an association of metal ions with amyloid formation in AD.

It is interesting to note that non transgenic rats and mice do not develop AD, probably because of three differences in their Aβ sequence with respect to the human homologue. Significantly, all these mutations are in the 1-16 region of the peptide ($Arg^5 \rightarrow$ Gly, $Tyr^{10} \rightarrow$ Phe, $His^{13} \rightarrow$ Arg), which, as discussed more in details below, is thought to be the main metal binding region. Another observation which supports this hypothesis is the fact that the non pathological peptide P3 corresponds to the Aβ(17-40) peptide, and therefore does not comprehend the 1-16 region.

It has also been demonstrated that Cu^{+2} and Zn^{+2} chelators can be used to solubilize Aβ aggregates [25]. The administration of these drugs to transgenic mice

is accompanied by a modest increase in soluble Aβ and slows down the development of AD in these animals, thus supporting the connection among metal ion concentrations, amyloid plaques formation and AD development.
All together, the experimental evidences collected until now strongly increased the interest in elucidating the role of metal ions and many efforts have been made during the last years to study the structure and the behavior of Aβ peptides in complex with metal ions. It is important to recall that neither Aβ(1-40) nor Aβ(1-42) crystallize so there is no X-ray structure of the monomer of either form. However, several experimental techniques have been used in order to identify the peptide structure, both in the absence and in the presence of metal ions: among them, Electron Paramagnetic Resonance (EPR) [26], Nuclear Magnetic Resonance (NMR) [29] [28] [27], CD [26] [29] and XAS [38] [33] are the most common.
Extensive reviews on metal-Aβ interaction are available [30] [31] [32], however in the following a short resume of the main experimental results, focused in particular on Cu- and Zn-$A\beta$ complexes which are of particular interest for this thesis, will be given. It is important to note that the studies described below are performed on various fragments of the $A\beta$ peptide and in different experimental conditions (nature and concentration of buffer, pH, incubation time). This can be one of the reasons why there is no uniform consensus on the metal ions coordination modes. Nevertheless, some major indications have emerged.

Cu studies:
Syme *et al.* [26] use a multi-technique (EPR, NMR, CD) approach to study the Cu binding mode of $A\beta$(1-28) peptide. They come to the conclusion that Cu coordinating ligands include the N-terminal amino group and the imidazole rings of His6, His13, and His14 in a square-planar geometry.
Ma *et al.*[35] obtain a slightly different result for Cu-$A\beta$(1-16) complex. A combination of CD and NMR measurements leads them to suggest that His6, His13, His14 and Tyr10 are involved in the square-planar coordination of Cu.
Another important work has been published by Strelstov and coworkers [33]. Their model, based on a combined XAS and Density Functional Theory (DFT) analysis, suggests a distorted six-coordinated (3N3O) geometry involving the

three histidines, glutamic or aspartic acid and axial water molecules.
The work of Karr *et al.* [34] is mainly focused on elucidating the role of the N-terminal region of the peptide in Cu binding. In their model, based on EPR experiments performed on Aβ fragments of different length, the Cu is bound to 2 histidine residues, a nitrogen atom belonging to a residue in the N-terminal region of the peptide and an oxygen atom (not belonging to Tyrosine10). A similar model had been previously proposed by Kowalik-Jankowska *et al.* [35], who, analyzing UV-Vis, CD and EPR data, reported for both $A\beta$(1-16) and $A\beta$(1-28) the binding of His13, His 14, N-terminus and an oxygen atom.
It is interesting to note how there is, with the remarkable exception of the two papers above [34][35], a consensus on the binding of the 3 His residues to the Cu, while the identity of the other residues involved in Cu binding is still debated. In conclusion, it appears that the nitrogen rich coordination sphere around the metal may include the three histidine residues, a fourth ligand which is most likely an oxygen donor atom [36] and possibly oxygen atoms belonging to water molecules.

Zn studies:
The situation in the presence of Zn ions is significatively less clear. The experimental findings can roughly be divided into two groups: many works suggest models where Zn coordination modes are definitely different from Cu coordination mode, other studies indicate for Zn a binding mode which is essentially identical to the one found for Cu.
To the former group belong an interesting work by Syme *et al.*[28], who studied by NMR, UV and CD the binding mode of Zn in complex with $A\beta$(1-28). Their NMR data indicate that His6, His13 and His14 residues are implicated in Zn-Aβ binding. They show that high molecular weight polymeric species are formed, thus suggesting that Zn coordination is dominated by inter-molecular coordination with consequent formation of polymeric species. In addition, they note that the UV spectra acquired either in the presence of Cu or in the presence of Zn ions are quite different, thus indicating that the coordination modes of these two metal ions are significantly different. A schematic model of the Zn coordination modes (taken from [28]) is represented in Fig. 1.9.

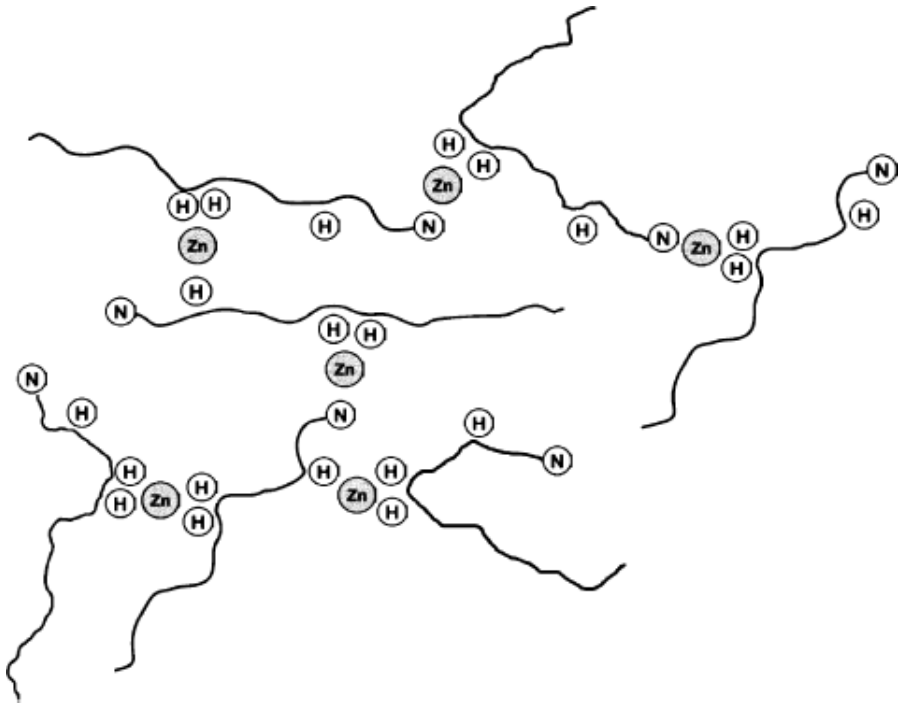

Figure 1.9: Intermolecular Zn^{2+} binding by Aβ peptide. Conjectural model showing how various histidine (H) residues and the N-terminus (N) of the Aβ peptide may be binding Zn.

The model described above is consistent with the fluorescence and VIS-UV experiments of Tõugu *et al.* [37]. They show that Aβ(1-40) forms a stable complex with Cu ions, while Zn promotes the partial aggregation of the peptide and the formation of polymeric species.
The possible role of Zn in promoting Aβ aggregation and fibrils formation has also been investigated. In particular, in a combined NMR, FTIR and XAS study Dong *et al.* [38] show that the Aβ(13-21) fragment reveals a β-sheet structure where parallel peptides are arranged in fibrils. They suggest a model where His13 residues on two different peptides chelate the metal, thus promoting fibrils formation.
To the latter group belong, among the others, the work of [27] and [39]. Danielsson *et al.* suggest for Zn-Aβ(1-40) peptide a model similar to that of [26] for Cu, where Zn binding involves the three histidines and the N-terminus. Zirah *et al.* study by NMR the Zn-Aβ(1-16) complex and identify the residues His6, His13, His14 and Glu11 carboxylate as ligands that tetrahedrally coordinate the

Zn cation. Both these works suggest therefore a monomeric state of the Zn-Aβ complex.

Even though the role played by Aβ oligomers and/or fibrils in the AD pathogenesis is not completely understood, it is clear how a detailed knowledge about Cu and Zn binding sites, and in particular the behavior of these ions with respect to Aβ polymerization is very important. The XAS study presented in section 3.1 is indeed aimed at determining the metal coordination modes.

1.4 Transmissible Spongiform Encephalopathies and the Prion Protein

In 18th century England, a disease affecting the behavior of sheep was identified. This disease, which was recognized to be highly contagious, was termed scrapie because it caused the sheep to rub themselves against fences, trees and other hard objects scraping off their own wool. It also caused the sheep to walk poorly, display tremors, go blind, fall down and, at its last stage, die. When the brains of the sheep were dissected, the presence of many tiny holes, which made the tissues look like a sponge, was noticed. In addition to this characteristic sponge-like feature, the brains also showed shrunken nerve cells and proliferation of glial cells, known as astrogliosis.

In 1920, the German neurologists Hans Creutzfeldt and Alfons Jakob described a human disease with symptoms that included dementia, change in gait, posture and movement, personality change, problems with speech and balance, and memory loss. This progressively degenerative disease always led to death. Upon autopsy, the brains of the affected individuals showed astrogliosis, the same characteristic as in scrapie brains. This human disease was called Creutzfeldt-Jakob disease (CJD), but no knowledge of its link to scrapie or its underlying cause was known.

In 1957, the American neurologist Gajdusek made a trip to Papua New Guinea and got in contact with a peculiar, apparently infectious disease who affected a local population, the Fore people, called kuru. It primarily infected women and children and its symptoms included unsteadiness of gait, hands, eyes and voice, tremor and shivering. The apparent source of transmission to the Fore people was through the practice of cannibalism. The Fore people, especially the women and children, did not have many sources of protein and had begun to cannibalize their dead as a way to conserve protein. The women and children, as lesser members of the Fore society, often received less desirable body parts. This included the brain and spinal cord. The theory of kuru transmission was that women and children ate the bodies, including the brains, of the kuru-afflicted people and the disease was passed on. A similarity between the kuru-infected brains and the description of the brains of patients with Creutzfeldt-Jakob disease was noticed:

they both showed astrogliosis and spongiform degeneration [40].
Nowadays all these pathologies are known to belong to the same class, the so-called Transmissible Spongiform Encephalopathies (TSEs), which comprise a group of fatal infectious neurodegenerative diseases that affect several animal species including mammals. They are all PCDs pathologies characterized by a fatal degeneration of the CNS.
In animals, the most common TSE is the scrapie observed in sheep. In the last decade of the XX century the bovine form of the disease (Bovine Spongiform Encephalopathy, BSE) has gained much attention because of the possible relevance for human safety. In particular, because of the epidemic of BSE, clinical surveillance of the most common occurring TSE in humans, the CJD, was established in several countries.

1.4.1 Physiology and Pathology of the TSEs

All TSEs are characterized by spongiform degeneration (formation of fluid-filled holes in the brain tissue) and astrocytic gliosis (proliferation and branching of glial, structural non-neuronal, cells in the brain) of the CNS (see Fig. 1.10), that invariably lead to death. Interestingly this fatal process is accompanied by no febrile or immune system response, nor by the other common reactions shown by an organism which comes into contact with a pathogen. This observation suggests the presence of a peculiar infectious mechanism [41] the details of which will be given in the following paragraph 1.4.2.
There are at least three forms of TSE disease which affects humans [42]:
-Sporadic form, which is the most common form (about 85% of cases) of the disease;
-Heritable form, which is associated with mutations within the prion protein (PrP) gene (about 10% of cases). More than 20 mutations of the PrP gene are now known to cause in humans the inherited form of the diseases;
-Acquired form, which is a result of ingestion or inoculation of TSE-contaminated materials.
TSEs are unique among protein misfolding diseases because they have also a transmissible form. In fact, these diseases have all of the characteristics of more

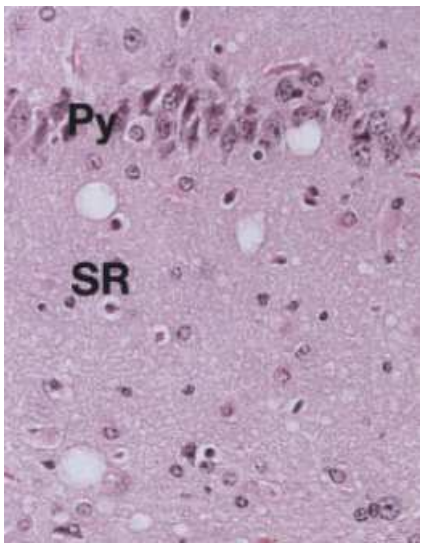

Figure 1.10: Neuropathologic changes in Swiss mice brain following inoculation with scrapie prions. Spongiform degeneration is clearly visible in the left and upper parts of this section of the hippocampus [41]. Py is the pyramidal cell layer, SR is the stratum radiatum.

conventional viral or bacterial agents in the sense that they can replicate, have different strains of agent which are associated with different prion disease phenotypes in vivo, and demonstrate very strong species specificities.
The annual incidence of the disease is uniform and accounts for about one case per million. The mean onset age of the disease is 65 years [43]. Main symptoms are: rapidly progressive dementia with myoclonus (rapid muscular contractions); cortical blindness (i.e. blindness due to cerebral damage); pyramidal and extrapyramidal signs (paralysis, anomalous muscular tone and rigidity).
From the physiological point of view, the disease hallmarks are characteristic pseudoperiodic sharp complexes of peaks in the electroencephalogram, associated with cerebellar ataxia (non-coordination of movements). The accumulation of plaques in the brain (typical of the 'kuru' form of the disease) is observed only in a small minority of cases (5% of total cases). The death usually occurs within 3-4 months from the first manifestation.

1.4.2 The Structure of PrP

The discovery of the source of CJD and of all the other TSEs has been complex and still presents some uncertainty. However, TSEs are nowadays one of the best understood neurodegenerative disorders [43]. At the beginning of the XX century only the familial forms of the TSEs were recognized, while the infectious form of the pathology was unknown[44]. The discovery that apes inoculated with brain extracts from CJD patients would develop the disease was crucial in clarifying that some sort of pathogen was the cause of the disease, but the nature of this pathogen was unclear, since the responses typical of a organism in the presence of a pathogen was missing.

The main advance in understanding the nature of the pathogen agent was obtained by Stanley B.Prusiner's, who was able to purify and quantify the amount of infective agent in a given sample, thus determining that scrapie infectivity could be reduced by procedures which hydrolyze or modify proteins. These observations were interpreted by postulating that a proteic macromolecule was the pathogen agent for scrapie and CJD. Following Prusiner's proposal, this pathogen was named prion, which defines a proteinaceous infectious particle that lacks nucleic acid.

Nowadays there are many experimental data that allow to conclude that prions are entirely made by a single protein, the PrP, although the possible involvement of other types of molecules or small proteins cannot be completely ruled out.

The pathogenetic form of the protein is called PrP^{Sc} (Scrapie Prion Protein). It has been shown that the infectivity titre is proportional to PrP^{Sc} concentration [45]. Infectivity is retained also in the presence of highly purified preparations of PrP^{Sc}. Once the discovery that infective diseases can be mediated by a proteic pathogen is accepted, it is necessary to understand the origin of the involved proteic material. It turns out that the PrP^{Sc} gene is contained in the genome of all the species that can develop TSE. PrP is coded in a single gene, and the physiological protein, called Cellular Prion Protein (PrP^{C}), is commonly expressed [46] in the CNS, the brain, the heart, the lungs and the lymphoid system. It is also expressed at lower level in other tissues such as muscles, and very small traces can be found in blood.

In humans, the expressed protein is a 254 amino acids long glycoprotein. The

N-terminal region of PrP, up to residue 120, is unstructured and highly flexible in solution. A characteristic hallmark of this region is the so-called octarepeat domain composed of a number of repeats of the fundamental eight-residue sequence PHGGGWGQ. The C-terminal domain contains three α-helical segments, two short α-strands, two Cysteine residues linked by a disulfide bond, and a glycosylphosphatidylinositol anchor that tethers PrP to the membrane surface. A diagram with the main features of the primary structure of the PrP is given in Fig. 1.11.

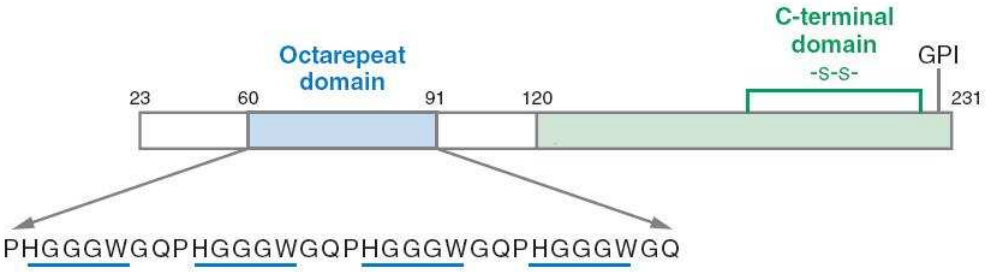

Figure 1.11: A schematic diagram of PrP [51].

The octarepeat region is particularly interesting, because it is one of the more conserved regions of the PrP protein, thus proving that there is a selective pressure on it and suggesting that PrP should have a physiological role. The octarepeat region has been proved to be a binding site for metals[51]. The number of octarepeats depends on the organism in which the protein is expressed. For what concerns the more studied organisms, in cows there are five or six octarepeats [48], while in humans there are five octarepeats. In humans, mutations in the PrP that lead to the synthesis of mutant PrP with 6-14 octarepeats is one of the causes of the genetic form of CJD [49].
The two forms, PrP^C and PrP^{Sc}, have identical primary structures, but exhibit significant differences in their secondary structure [47]. PrP^C contains $\sim$40% α-helix and has a minimal β-sheet content, whereas a 43% β-sheet and a reduction of α-helix contents are found in PrP^{Sc}. The PrP^C-PrP^{Sc} conversion may occur without any chemical modification, but the two isomers have considerably different physicochemical properties [50]. Fig. 1.12 shows a schematic picture of

both forms of the protein.

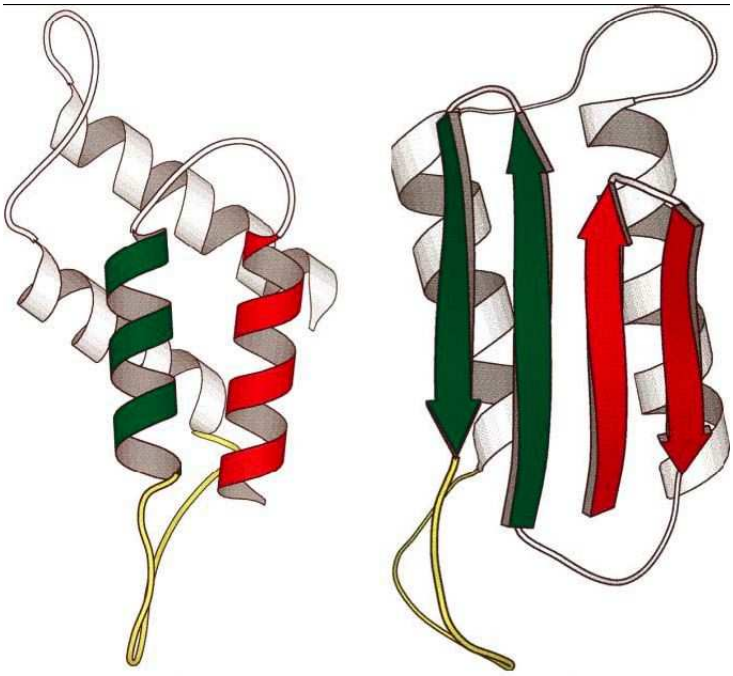

Figure 1.12: Secondary structure of PrP^{C} (left panel) and PrP^{Sc} (right panel).

The finding that the brain of CJD patients contains deposits of PrP protein in its scrapie form lead to the theory that the disease is caused, at least in part, by the aggregation of PrP^{Sc}. Although the presence of deposits of PrP in the brain is an indication of prion disease, it is now widely accepted that the real toxic species are the PrP oligomers. It has been shown that low molecular weight oligomers of the PrP are neurotoxic *in vitro* on cultures of neurons and *in vivo* after subcortical stereotaxic injection. On the contrary, monomeric PrP is not toxic, and large aggregates of PrP exhibits no toxicity *in vitro* and are less toxic than their oligomeric counterparts *in vivo* [52].

1.4.3 Interaction of PrP with Metal Ions

Observations from *in vivo* and *in vitro* studies using full-length recombinant PrP or its fragments led to important findings regarding PrP-metal interaction and its significance to prion disease pathogenesis [53]. It has been shown that recombinant PrP binds several divalent cations, including Cu, Fe, Zn, Mn and Ni.

The octarepeat region of PrP is the principal metal binding site, and it has the highest affinity for Cu, followed by Ni, Zn and Mn [54].
The interaction of PrP with metals has been widely studied looking for the physiological and pathological implications of their association. For example, PrP is believed to mediate the uptake of Cu and Fe, suggesting a role in their cellular metabolism.
The association of PrP with Cu is better characterized than its interaction with other metals. Four Cu binding sites have been identified within the octapeptide repeat region of PrP with additional sites on the two histidine residues that do not belong to the octarepeat region [56] [102]. A drawing of PrP with its Cu binding sites is given in Fig. 1.13.

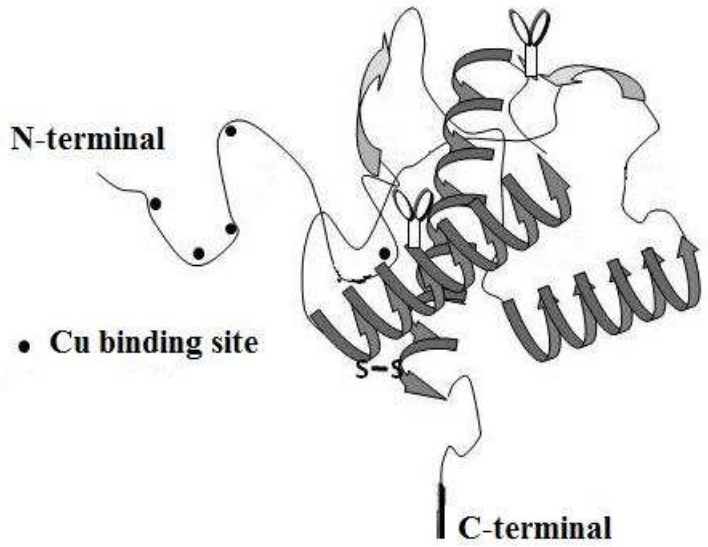

Figure 1.13: A model of PrP demonstrating the known copper binding sites in the octarepeat region and histidine residues 96 and 111 [53].

The interaction of PrP with Cu has also been studied using XAS [102]. Both the Cu-bovine PrP complexes and smaller Cu complexes of peptides containing one, two, and four copies of the octarepeat have been studied. Peptides containing one and two-octarepeat copies in sub-stoichiometric Cu complexes showed the direct binding to a single His compatible with can intra-repeat geometry. Alternatively, the Cu-bovine PrP complex and Cu in complex with a four-octarepeat peptide at half-site-occupancy showed Cu directly bound to two His residues,

consistent with an inter-repeat binding mode.

In addition to Cu, other metals have been shown to bind PrP. Among them, zinc is the one with the highest affinity [54]. Zinc is also the only metal other than copper that induces PrP endocytosis. Zinc, inhibits fibril formation and promotes intermolecular interactions. It has been suggested that in vivo PrP may actually bind zinc rather than copper given the abundance of available zinc in the brain, with peak levels up to 300 μM in the synaptic cleft of glutaminergic neurons. However, even large excesses of zinc are unable to displace copper from either the octarepeat region or the full-length protein, but EPR reveals that physiologically relevant levels of zinc significantly alter the distribution of copper among the available binding modes [55]. These observations suggest that the interaction of PrP with Zn may be significant given the relative abundance of this metal in the brain.

From the physio-pathological point of view, observations from neuroblastoma cells suggest that PrP binds extracellular copper ions and delivers them to endocytic compartments, thus possibly functioning as a copper uptake protein [57]. The octarepeat region of PrP is essential for this process since its deletion inhibits Cu uptake. Although in transgenic mice lacking PrP expression there is just a minimal difference in the Cu content of brains from wild type, it has been suggested that PrP may be a major Cu delivery protein [58].

1.5 Parkinson's Disease and Neuromelanin

Parkinson's disease (PD), which was first described by James Parkinson in 1817 in the book entitled 'An Essay of the Shaking Palsy', is the second most prevalent neurodegenerative disorder in the Western world. It is clinically defined as a neurological pathology characterized by 4 cardinal signs: resting tremor, bradykinesia, rigidity, and postural instability [59]. From a physiological point of view, it is characterized by depigmentation of the substantia nigra (SN), which is caused by the selective and progressive loss of dopaminergic neurons, and by the presence of intraneuronal proteinaceous inclusions known as Lewy bodies within the surviving neurons of the SN and other brain regions. These inclusions are enriched in filamentous α-synuclein and other proteins that are often highly ubiquitinated. In addition to the loss of $\simeq$50% of neurons in the SN, there is widespread neurodegeneration in the CNS with the *pars compacta* and the *locus coeruleus* (LC) being involved in midstages of the disease.
The incidence of the disease rises steeply with age, the median age of onset is 60 years and the mean duration of the disease from diagnosis to death is 15 years. The precise mode of death is difficult to identify in most cases, but pneumonia is the most common cause. PD is not related to race or religion, and literary and historical precedents before the publication of Parkinson's monograph make it unlikely to be a postindustrial condition. The percentage of affected individuals within a population rises from 1% at 65 years to 5% at 85 years, making age the main risk factor for PD. The majority of cases are thought to be idiopathic, however, in 5-10% of cases there is a clear genetic component with both recessive and dominant modes of inheritance [60].
The molecular pathways leading to PD are still unclear, but the discovery of genes linked to rare familial forms of the pathology during the last decade have provided vital clues in understanding molecular pathogenesis of the more common sporadic illness [61].

1.5.1 Physiology and Pathology of Parkinson's Disease

PD commonly presents itself with impairment of dexterity or with a slight dragging the feet. The onset is gradual and the earliest symptoms might be unnoticed

or misinterpreted for a long time. Fatigue and stiffness are common but non-specific complaints. The early physical signs are often erroneously ascribed to old age, misery, introspection, or rheumatism, and a lag of 2-3 years from the first symptoms to diagnosis is not unusual. In the late stages of the disease, the face of patients is masked and expressionless, the speech is monotonous and slightly slurred, and posture is flexed with a severe tremor of the hands. Risk of dementia exists, particularly in those patients who show prominent gait and speech disorders or depression. The greatest risk factor for dementia, however, seems to be the age of the patient and not the duration of the disease.

Although PD is considered a sporadic disorder, remarkably few environmental causes or triggers have so far been identified. Similar to other neurodegenerative diseases, ageing is the major risk factor, although 10% of people with the disease are younger than 45 years of age. Never smokers are twice as likely to develop PD, and men and postmenopausal women who are not taking hormone replacement, who take no or very low quantities of daily caffeine, seem to be at increased (about 25% more) risk. These findings are probably related to dopamine's role in reward pathways rather than to any neuroprotective effect of tobacco smoke, nicotine, or caffeine. Weak associations between PD and head injury, rural living, middle-age obesity, lack of exercise, well-water ingestion, and herbicide and insecticide exposure have also been reported.

From a genetic point of view, PD hereditary forms with autosomal dominant or autosomal recessive inheritance have been identified. They include autosomal dominant point mutations or gene duplications or triplications in the $\alpha-$synuclein gene, and point mutations in the ubiquitin-C-terminal hydrolase-L1 and the leucine-rich repeat kinase genes, and also autosomal recessively inherited mutations in Parkin, PINK1, DJ-1 and the ATPase13A2 genes. By taking the biochemical function of these genes and mutations into account, it is possible to have an idea of the possible pathogenetic pathways which are at the basis of PD also in its more common sporadic form [62]. Essentially 3 mechanisms have been proposed:

1-Altered protein quality control

Accelerated protein aggregation or a dysfunction of the ubiquitin proteasome

system leads to a disturbance in protein quality control. In particular, point mutations or gene duplications lead to the aggregation of $\alpha-$synuclein and to the formation of $\alpha-$synuclein fibrils. The misfolded protein can be either refolded by chaperone proteins, thereby regaining their normal function or have to be degraded. They are marked by ubiquitin and are then directed to the proteasome. Dysfunction of one of these proteasome proteins therefore leads to a dysfunction of the ubiquitin-proteasome system and to an accumulation of aggregated $\alpha-$synuclein in the cytosol of dopaminergic cells (see Fig. 1.14). $\alpha-$synuclein

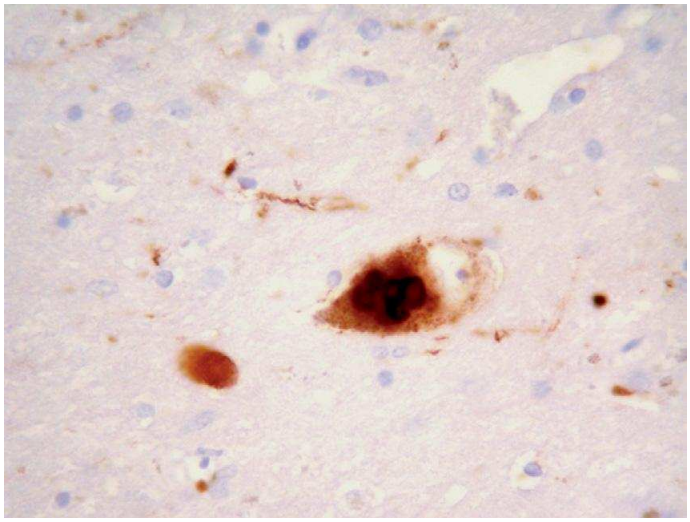

Figure 1.14: Light microscopy of a surviving neuron in the *substantia nigra* of a PD patient. The neuron is full of α-synuclein Lewy bodies.

aggregation mainly occurs in the SN neurons, but it has been found also in the motor part of the *nucleus vagus*, in the olfactory bulb and in the LC.
$\alpha-$synuclein is a small (14 kDa) natively unfolded presynaptic protein believed to play a role in synaptic vesicle recycling, storage and compartmentalization of neurotransmitters and associates with vesicular and membranous structures. Structurally, it consists of an N-terminal amphipathic region, a hydrophobic middle region (containing the non-amyloid-β component domain) and an acidic C-terminal region. Three missense mutations in α-synuclein gene are associated with autosomal dominant PD [63].
$\alpha-$synuclein has an increased propensity to aggregate due to its hydrophobic non-amyloid-β component domain. The presence of fibrillar α-synuclein as a

major structural component of Lewy bodies in PD suggests a role of aggregated α-synuclein in disease pathogenesis. As in the case of AD, however, most evidence indicates that oligomers but not the fibrils of $\alpha-$synuclein that are deposited in the Lewy bodies, are the real toxic species [64]. This would also imply that the rapid conversion of $\alpha-$synuclein from an oligomeric to an aggregated state, deposited in Lewy bodies, may help to detoxify the oligomeric form of $\alpha-$synuclein. That the formation of Lewy bodies might be a protective response following the disturbance of protein quality control is also substantiated by the finding that at the end stage of the disease almost all of the few remaining and surviving dopaminergic neurons contain Lewy bodies. Interestingly, dopamine tends to stabilize the oligomeric form and prevents the aggregation of $\alpha-$synuclein. This may be one reason for the selective vulnerability of dopaminergic neurons.

2-Mitochondrial dysfunction

Biochemical findings at autopsy as well as animal models studies suggest an altered mitochondrial function in PD, in particular a deficiency of complex I of the mitochondrial electron transport chain. Autosomal recessively inherited forms of PD with mutations in the PINK1 and the DJ-1 genes, which are related to mitochondrial activity, strongly support this hypothesis.

3-Altered kinase activity

Several aberrant kinase (enzymes that transfer phosphate groups from high-energy donor molecules) activities have been identified as contributing to the PD pathogenesis. Kinase related mutations represent indeed the most common monogenetic form of PD, affecting up to 16% of all patients of European origin and up to 40% in specific ethnic groups.

1.5.2 Diagnostic and Therapeutic Strategies in PD

The main symptom used for PD diagnosis is the unequivocal bradykinesia. Other indications are the facial expression, which can be immobile and rigid, the reduced ability to express emotions, the speech which becomes slow, quiet, and lacking in rhythm and melody. PD is also characterized by a coarse, slow, pill

rolling tremor of the hands (4-6 cycles/s) and muscular rigidity.
Diagnostic techniques may also be used, in particular MRI shows extensive subcortical white-matter ischaemic changes. However, the ultimate diagnosis is the one done with *post mortem* analysis by detecting the presence of Lewy bodies and the loss of dopaminergic neurons in the *substantia nigra* pars compacta.
From a therapeutic point of view, PD is still an incurable progressive disease, but treatments substantially improves quality of life and functional capacity. Several options exist for the symptomatic treatment of the pathology: oral treatment with L-Dopa, dopamine agonists, monoamine oxidase-B inhibitors and catechol-o-methyl-transferase inhibitors, continuous delivery of L-Dopa and dopamine agonists via transcutaneous or subcutaneous infusion, and deep brain stimulation. However, none of these therapies modifies the natural course of the disease[62]. Therapies aimed only at the execution of cell death, although possibly able to slow down the pathology development, are indeed unable to restore the function of neurons. Effective therapies may be found by interfering with the main pathogenetic mechanisms. A therapy with chaperones, small molecules that inhibit protein aggregation, and are able to enforce the ubiquitin- proteasome degradation pathway, could stop the $\alpha-$synuclein aggregation process and the formation of oligomers. Furthermore, mitochondrial dysfunction, oxidative stress and inflammation can be addressed. Also some kinases may prove to be a promising target.

1.5.3 The Structure of Neuromelanin

The origin of the name melanin, from the Greek word $\mu\epsilon\lambda\alpha\varsigma$, black, is usually attributed to the Swedish chemist Berzelius [65]. Melanin in the brain has a similar appearance and structure to cutaneous melanins, and has thus been designated neuromelanin (NM).
Based on their precursor molecules, melanins are classified into four groups [66]:
1. Eumelanin is formed from L-3,4-dihydroxyphenylalanine (L-dopa).
2. Pheomelanin is formed by oxidative polymerization of 5-S-cysteinyl-dopa or 2-S-cysteinyl-dopa.
3. Neuromelanin is thought to be formed by oxidative polymerization of dopamine

or noradrenaline, with the possible involvement of cysteinyl-derivatives.
4. Allomelanin is formed by the oxidation of polyphenols, such as catechols and 1,8-dihydroxynaphtalene.
Although much is known about melanins outside the CNS, to which NM is thought to be related, many basic questions remain to be answered about NMs. It is unclear why some human dopamine neurons produce an insoluble pigment within their cytoplasm and others do not. Neurons rich in NM are indeed found especially in the SN and LC. (see Fig. 1.15). The structure and role of NM have

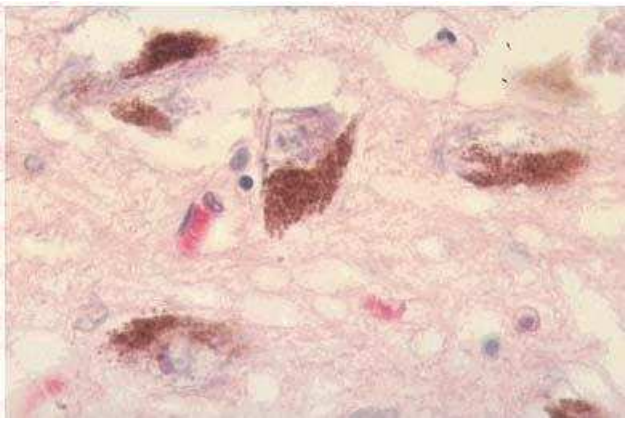

Figure 1.15: SN neurons containing NM.

been only partially characterized and are still a matter of investigation because of the possible involvement in brain aging and PD [67]. In fact, this pigment first appears in humans at 2-3 years of age and accumulates with aging.
The NM of SN shares some characteristics of melanins such as redox activity and chelating ability for metals. In NM isolated from SN and LC, a significant amount of iron was found. Due to its strong chelating ability for iron and other metals (cadmium, mercury and manganese), NM could play an important protective role in neurons.
The process of neuromelanin formation is obscure, although some steps have been elucidated [69]. It has long been debated whether the synthesis of NM is enzymatically mediated or whether it is a pure auto-oxidation process of dopamine derivatives. For the enzymatic synthesis, the enzyme tyrosinase catalyzes the conversion of tyrosine to L-dopa and then to dopa-quinone. Some authors proposed that tyrosinase could also be involved in neuromelanin biosynthesis, but

also other enzymatic mechanisms have been suggested, including tyrosine hydroxylase mediated oxidation of dopamine. Alternatively, NM could derive from non-enzymatic oxidation. A dopamine-melanin can indeed be synthesized *in vitro* by the auto-oxidation of dopamine, although there are several structural differences between synthetic melanins and the natural one isolated from the *substantia nigra*.

The proper melanic component of NM contains two classes of molecules in rather well-determined proportions. One is a benzothiazine-based molecule characteristic of pheomelanin that is formed through the incorporation of cysteine with dopamine; it constitutes 20-25% of the total melanic component of human NM. The other one is an indole-based molecule characteristic of eumelanin that is formed through the oxidation of dopamine [70]. The identification of dopamine and cysteinyl-dopamine as building blocks of natural NM lends support to the idea that its synthesis plays a detoxifying role, preventing an otherwise toxic intraneuronal accumulation of dopamine compounds.

NM has also been show to have high affinity for biomolecules, in particular lipids [68] and proteins. The lipidic component is mainly constituted by high molecular weight lipids, while the peptide component of NM amounts to about 15% of its weight and is composed by several aminoacids found in fairly well preserved proportions. NMR studies [71] have shown that different $\alpha-$synuclein immunoreactive components are present in patients with Lewy bodies, thus suggesting a possible covalent bond between $\alpha-$synuclein and NM.

From a structural point of view, X-ray diffraction studies [72] have shown that NM has a multilayer (graphite-like) three-dimensional structure made of planar overlapping sheets of molecules containing indolebenzothiazine rings. Scanning probe and photoelectron emission microscopies have demonstrated that NM can be also found in spherical structures with a diameter of about 30 nm with pheomelanin at the core and eumelanin at the surface [73].

Several hypotheses have been proposed for the role of NM in the protection or degeneration of dopaminergic neurons in the SN. NM may play a cytoprotective role by sequestering redox active metals (Fe, Cu, Mn and Cr), toxic metals (Cd, Hg and Pb) and/or organic toxic compounds such as pesticides, which have been reported to be environmental risk factors for PD [70]. In contrast, it has been

proposed that NM increases the vulnerability of SN neurons and that it can be a source of free radicals by reaction with hydrogen peroxide.
A possible approach to this problem is to consider NM in terms of what is known about the better-characterized and more prominent peripheral melanins. Clearly, an increased understanding of the normal development of NM in the human substantia nigra and changes that occur in PD will advance our understanding of this disorder and may provide targets for the development of novel interventions or treatments for the disease.

Chapter 2

X-ray Absorption Spectroscopy

X-ray absorption spectroscopy is a technique which consists in extracting structural information from the study of the absorption coefficient behavior as a function of the photon energy. After the edge, the oscillatory structure of the x-ray absorption coefficient depends on the detailed atomic structure around the absorbing atom. For this reason, XAS is a very important probe in many scientific fields, from biology to chemistry, electronics, geophysics, metallurgy, and materials science, where the knowledge of local atomic structure is essential.
In this chapter, a short description of XAS theory and of the experimental setup is followed by an overview of data processing and analysis strategies, focusing on those used for the work presented in this thesis. A particular attention will be given to theoretical and experimental aspects which are particularly relevant for the biological XAS applications described in this work.

2.1 Theory of XAS

The XAS theoretical basis was given in 1932 by Krönig, who first explained the X-ray spectrum oscillation as the modulation of the ionized photoelectron final state wavefunction due to the interference with the back-scattered waves from neighboring atoms. The XAS technique, however, became popular many years later the discover of its potentialities, that is when synchrotron accelerators became available as radiation sources. Nowadays this technique is widely used for the structural and dynamical study of many different systems, and it is one of the election techniques for soft and amorphous matter investigations.

2.1.1 X-ray Absorption

X-ray absorption spectroscopy measures the absorption of x-rays as a function of their energy $E = \hbar\omega$. Absorption processes are governed by the well known Lambert-Beer law:

$$I = I_0 e^{-\mu(E)d} \tag{2.1}$$

where I_0 is the intensity of the radiation impinging on the system, $\mu(E)$ is the absorption coefficient and d is its thickness.

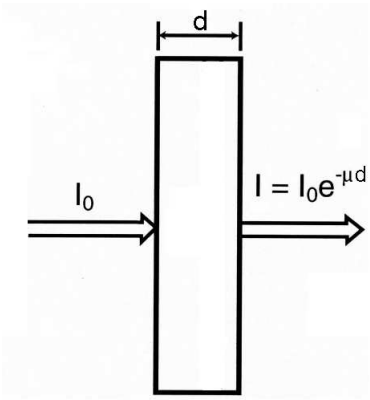

Figure 2.1: Lambert-Beer law.

The absorption coefficient can be therefore determined from the decay in the x-ray beam intensity I with distance d. The behavior of $\mu(E)$ as a function of the photon energy E shows three general features (see Fig. 2.2)
(1) an overall decrease in x-ray absorption with increasing energy;

(2) the presence of a sharp rise at certain energies called edges;
(3) above the edges, an oscillatory structure that modulates the absorption, typically by a few percent of the overall absorption coefficient.

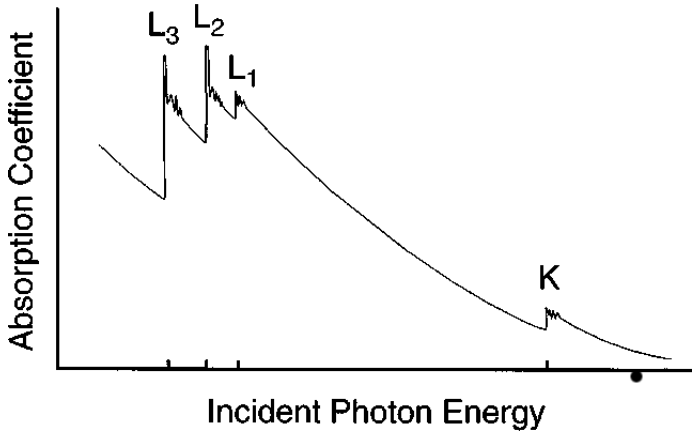

Figure 2.2: Sketch of the typical behavior of the x-ray absorption coefficient as a function of incident photon energy for K, L_1, L_2, L_3 edges.

The first feature is due to the well-understood quantum-mechanical phenomenon of x-ray absorption by atoms, and the energy position of the second feature is unique to a given absorption atom and corresponds to the ionization energy of inner-shell electrons. The third feature is due to the presence of atoms surrounding the absorber and depends on their interatomic distances and coordination numbers[74].
Before going into the details of a complete quantitative description of the oscillatory structure, its origin can be explained at a qualitative level. When a photon in the x-ray energy range is absorbed by an atom, a core electron is ejected. The kinetic energy of this photoelectron is given by the difference between the photon energy and the electron ionization energy. The photoelectron can be described as an outgoing spherical wave, which, if the absorbing atom is not isolated, is back-scattered by nearby atoms giving rise to incoming spherical waves. The absorption coefficient μ depends, at the first level approximation, on the dipole matrix element between the initial core state and the photoelectron final state. From a qualitative point of view, this matrix element is dependent on the interference between the outgoing wave and the incoming backscattered waves. The phase relationship between these waves is sensitive to the distance, number and

chemical nature of nearby atoms. Because of the limited length of photoelectron mean free path only the atoms located at a small distance from the absorber will affect this process. This is why XAS is a technique which is sensitive only to the local geometrical and chemical structure around the absorber, while it is insensitive to long range order.

Once the photoelectron is emitted, an hole in the core level is left and so an excited state is created. This excited state can decay via two mechanisms, namely radiative (fluorescence emission) and non-radiative (Auger emission). In the radiative mechanism, an electron from an outer shell fills the core hole and a fluorescence photon with energy characteristic of the involved transitions is emitted. In the non-radiative mechanism, this photon scatters with another outer electron which is emitted (Auger electron). The two de-excitation mechanisms are in competition. Their relative weight depends on atomic number and it is measured by the fluorescence yield η_s

$$\eta_s = \frac{X_s}{X_s + A_s} \tag{2.2}$$

where s labels the absorption edge and X_s and A_s are the emission probabilities of fluorescence photons and Auger electrons, respectively. As shown in Fig. 2.3, the fluorescence yield is low for low-Z elements, and increases till 100% for K-edge absorption in high-Z elements. For the same element fluorescence yield is higher for K shell than for L shells.

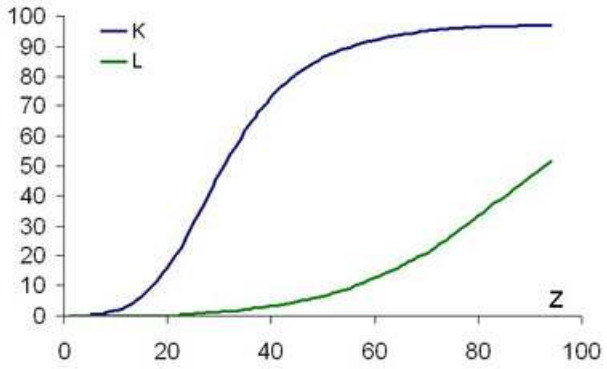

Figure 2.3: Fluorescence Yield as a function of atomic number Z.

The total de-excitation rate gives the core-hole lifetime τ_h, which represents the upper limit to the time allowed to the photoelectron for probing the local

structure around the absorbing atom. τ_h decreases as Z increases, because for larger atomic numbers the core-hole is deeper and so there are more upper level from which an electron can drop to fill the hole. The typical order of magnitude for τ_h is 10^{-15} s. Because of Heisenberg's uncertainty principle, τ_h is naturally associated with an energy width of the excited state $\Gamma_h = \hbar/\tau_h$, which contributes to the energy resolution of XAS spectra.

In order to give a quantitative description of the absorption coefficient oscillation, a quanto-mechanical calculation is necessary. At a first level, a semiclassical approach, where the electromagnetic radiation is described as a classical field and the matter as a quantic system, is sufficient [75]. In the non-relativistic case, the Schrödinger equation holds:

$$H = \frac{1}{2m}(\mathbf{p} - \frac{e\mathbf{A}}{c}) + V(\mathbf{r}) = \frac{\mathbf{p}^2}{2r} - \frac{e}{mc}\mathbf{A}\cdot\mathbf{p} + \frac{e^2}{2mc^2}\mathbf{A}^2 + V(\mathbf{r}) = H_0 + H' \quad (2.3)$$

where H_0 is the unperturbed Hamiltonian and the electromagnetic field has been described via the minimal substitution $\mathbf{p} \rightarrow (\mathbf{p} - \frac{e\mathbf{A}}{c})$. Using the time-dependent perturbation theory, at the first order approximation the transition rate between an initial state Ψ_i and a final state Ψ_f is given by

$$\tau_{if} = \frac{2\pi}{\hbar}|\langle\Psi_i|H'|\Psi_f\rangle|^2\delta(E_f - E_i - \hbar\omega) \quad (2.4)$$

where $\hbar\omega$ is the energy of the incident radiation, E_i and E_f are the energies of the initial and final states and H' is the perturbed hamiltonian

$$H' = -\frac{e}{mc}\mathbf{A}\cdot\mathbf{p} + \frac{e^2}{2mc^2}\mathbf{A}^2 + V(\mathbf{r}) \quad (2.5)$$

Omitting the quadratic term in e, the expression of the transition rate becomes

$$\tau_{if} = \frac{2\pi}{\hbar}(\frac{e}{mc})^2|\langle\Psi_i|\mathbf{A}\cdot\mathbf{p}|\Psi_f\rangle|^2\delta(E_f - E_i - \hbar\omega) \quad (2.6)$$

Considering that

$$\mathbf{A} = -\frac{c\mathbf{E}}{\omega} \text{ and } E = E_0 e^{ikr}\widehat{e}, \quad (2.7)$$

where $\widehat{e}$ is the electric field versor, it is possible to write the (2.6) in the following form

$$\tau_{if} = \frac{2\pi}{\hbar}(\frac{eE_0}{m\omega})^2|\langle\Psi_i|e^{ikr}\widehat{e}\cdot\mathbf{p}|\Psi_f\rangle|^2\delta(E_f - E_i - \hbar\omega) \quad (2.8)$$

The (2.8) allows to obtain a quantitative expression for the power absorbed by the matter, W, in the unitary volume, which is given by the sum of all transition energies multiplied for the respective transition rate:

$$\frac{dW}{dV} = \frac{1}{V}\sum_f \hbar\omega\tau_{if} = \frac{1}{V}\sum_f \pi\omega(\frac{eE_0}{m\omega})^2|\langle\Psi_i|e^{ikr}\widehat{e}\cdot\mathbf{p}|\Psi_f\rangle|^2\delta(E_f - E_i - \hbar\omega) \quad (2.9)$$

In order to extract physical information from an x-ray absorption spectrum, it is necessary to relate the microscopic description of the system to macroscopic measurable quantities such as the absorption coefficient. To this purpose, it is worth writing the power dissipated by a cylinder of electromagnetic radiation of section $d\sigma$ and length dl which is in $x = x_0$ at $t = t_0$ and moves with velocity c/n (where n is the medium refraction index) along the x-axis. Being u the density of energy, the energy contained in the radiation cylinder is $u(x_0)d\sigma dl$. After a time dt, the cylinder will be in the position $x = x_0 + (c/n)dt$, and its energy will be then $U(x)d\sigma dl$. The difference between $U(x)$ and $U(x_0)$ corresponds to the energy dissipated during the motion. The Lambert-Beer law (2.1) holds, then

$$U(x) = U(x_0)e^{-\mu(E)(x-x_0)} \quad (2.10)$$

and the dissipated power during dt can be written as

$$dW = -\frac{U(x) - U(x_0)}{dt}d\sigma dl \simeq U(x_0)\frac{\mu dx}{dt}d\sigma dl \Rightarrow \frac{dW}{dV} \simeq U(x_0)\mu(E)\frac{c}{n} \quad (2.11)$$

The energy associated to the electromagnetic field is given by

$$U(x_0) = \frac{E_0^2}{4\pi}, \quad (2.12)$$

so the expression of the dissipated power from the macroscopic point of view can be finally written as

$$\frac{dW}{dV} \simeq \frac{E_0^2}{4\pi}\mu(E)\frac{c}{n} \quad (2.13)$$

It is now possible to compare the microscopic (2.9) and macroscopic (2.13) expression of the dissipated power in order to obtain the relationship between the absorption coefficient μ and the quanto-mechanical properties of the system:

$$\mu(E) = \mu(\hbar\omega) = \frac{n}{U(x_0)c}\frac{dW}{dV} = \sum_f \frac{4\pi^2e^2n}{m^2\omega c}|\langle\Psi_i|e^{ikr}\widehat{e}\cdot\mathbf{p}|\Psi_f\rangle|^2\delta(E_f - E_i - \hbar\omega) \quad (2.14)$$

When the wavelength of the radiation is higher than the characteristic length of initial and final state, it is possible to write the expression of μ (2.14) in the dipole approximation, obtaining:

$$\mu(\hbar\omega)_{dipole} = \sum_f \frac{4\pi^2 e^2 n}{m^2 \omega c} |\langle \Psi_i | \widehat{e} \cdot \mathbf{p} | \Psi_f \rangle|^2 \delta(E_f - E_i - \hbar\omega) \tag{2.15}$$

In the x-ray region, the dipole approximation is satisfactory for light atoms, but becomes less accurate for heavy atoms. In these cases, it is necessary to take into account also quadrupole terms. In the following, the dipole approximation is used. Considering that,

$$\langle \Psi_i | \mathbf{p} | \Psi_f \rangle = \langle \Psi_i | m \frac{d\mathbf{r}}{dt} | \Psi_f \rangle = \frac{m}{i\hbar} \langle \Psi_i | H\mathbf{r} - \mathbf{r}H | \Psi_f \rangle = \frac{m\omega_{if}}{i} \langle \Psi_i | \mathbf{r} | \Psi_f \rangle \tag{2.16}$$

a simpler form of the (2.15) can be written (when n=1):

$$\mu(\hbar\omega)_{dipole} = \sum_f 4\pi^2 \alpha \hbar\omega |\langle \Psi_i | \widehat{e} \cdot \mathbf{r} | \Psi_f \rangle|^2 \delta(E_f - E_i - \hbar\omega) \tag{2.17}$$

where $\alpha = e^2/\hbar c$ is the fine structure constant. Introducing the density of final states $\rho_F(E)$ such that $\rho_F(E)dE$ gives the number of final states with energy comprised between E and E+dE the expression of the absorption coefficient μ (2.17) can be rewritten as

$$\mu(\hbar\omega)_{dipole} = \sum_f 4\pi^2 \alpha \hbar\omega |\langle \Psi_i | \widehat{e} \cdot \mathbf{r} | \Psi_f \rangle|^2 \rho_F(E) dE|_{E_f = E_i + \hbar\omega} \tag{2.18}$$

If during the absorption process only the emitted photoelectron changes its state, while the other N-1 (so-called passive) electrons simply relax around the hole (sudden approximation), the N-body wavefunctions Ψ_i and Ψ_f can be factorized as the products

$$\langle \Psi_i | = \langle \Psi_i^{N-1} \psi_i |; | \Psi_f \rangle = | \Psi_f^{N-1} \psi_f \rangle \tag{2.19}$$

where Ψ^{N-1} are the Slater determinants of the N-1 passive electrons and ψ_i and ψ_f describe the initial and final state of the photoelectron. The interaction hamiltonian acts only on the active electron wavefunction, so the (2.18) can be written as

$$\mu(\hbar\omega)_{dipole} = \sum_f 4\pi^2 \alpha \hbar\omega |\langle \psi_i | \widehat{e} \cdot \mathbf{r} | \psi_f \rangle|^2 S_0^2 \rho_F(E) dE|_{E_f = E_i + \hbar\omega} \tag{2.20}$$

where

$$S_0^2 = |\langle \Psi_i^{N-1} | \Psi_f^{N-1} \rangle|^2 \tag{2.21}$$

is the overlapping integral among passive electron wavefunctions. If relaxation effects are negligible, the initial and final states of the N-1 passive electrons will be very similar thus giving $S_0^2 \simeq 1$; in real cases, S_0^2 is smaller than 1 and usually $0.8 < S_0^2 < 1$.

In order to evaluate the matrix element in the expression (2.20) it is necessary to define the initial $\psi_i(r) =< r|i >$ and final $\psi_f(r) =< r|f >$ state of the system. They both are eigenfunctions of the general unperturbed Hamiltonian (2.22)

$$H = -\frac{\hbar^2}{2m}\nabla^2 - \frac{Ze^2}{r} + V(\mathbf{r}) \tag{2.22}$$

The first term of (2.22) is the kinetic energy of the electron, the second one is the electrostatic interaction with the nucleus and the third one describes the potential in the surrounding region. Therefore an explicit form of $V(\mathbf{r})$ has to be written. Almost all practical calculations currently rely on a muffin-tin geometry (see Fig. 2.4), which consists of a spherical scattering potential centered

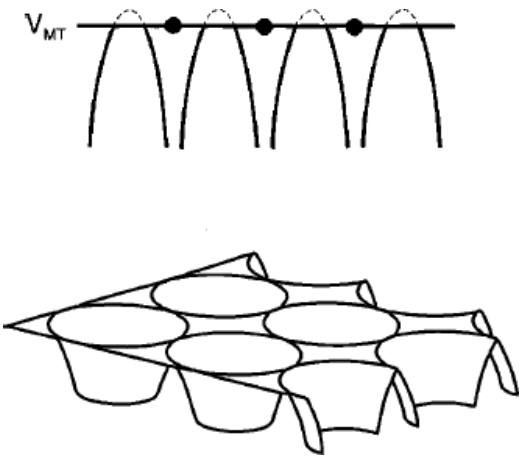

Figure 2.4: Schematic drawing of a one- (upper panel) and two-dimensional (lower panel) muffin-tin potential.

on each atom and a constant value in the interstitial region between atoms. In the multiple-scattering approach that most directly connects to the underlying atomic structure of a material, the muffin tin approximation provides atomic scattering centers that are described completely by the corresponding atomic

phase shifts, which are calculated from spherically symmetric atomic-like potentials inside the muffin tins. Green's-function propagators are then employed to connect these scattering centers.
The actual potential in a material (solid or cluster of atoms) is, of course, more complicated, but in the high energy region, where the kinetic energy of the excited electron is large, the electron is less sensitive to the details of the potential at the outer edges of the atom and in the regions between the atoms. The electron is mainly scattered by the inner parts of the atomic potential and moves almost freely in the average potential within the flat interstitial region. It is for this reason that a spherical muffin-tin potential is sufficient in this part of the spectrum. In the near-edge region (XANES, X-ray Absorption Near Edge Spectroscopy) and for ground state total-energy calculations, the details of the shape of the interatomic potential are much more important. Therefore, many efforts are put in developing methods which do not require this rough approximation [76]. Within a muffin-tin approximation it is important to optimize the calculation by adjusting the size of the muffin tins surrounding each atom (both the central atom whose core electron is being excited and neighboring atoms).
Two classes of muffin-tin approximations are mainly used: overlapping and non-overlapping. The use of overlapping spheres is the less common, and it is usually driven by the need to deal with large interstitial regions that can occur in open structures with large atom-size differences. Overlapping the spheres can decrease the amount of interstitial volume and hence reduce the effects of potential inhomogeneity in the interstitial volume. The non-overlapping case usually tries to maximize the radii so that the muffin tins touch or nearly touch. This is done to minimize the amount of interstitial region, where the potential is treated less accurately than inside the muffin tins. The overlapped case requires criteria for the definition of the muffin tins radii. Three approaches are usually employed:
(1) Empirical radii based on experimental considerations of tabulated radii, such as Pauling, covalent, metallic.
(2) The muffin tins can be adjusted until the ground state potentials at the boundary of neighboring atoms are approximately equal. This approach is based on the intuitive idea that the potential should not jump discontinuously across boundaries.

(3) Norman [77] has suggested counting charge to determine relative radii. In this prescription the atomic charge densities are overlapped, and the radii around the atoms are chosen such that the spherically averaged charge within each radius contains an amount equal to the neutral atom.
Once an expression of $V(\mathbf{r})$ has been chosen, it is possible to go back to (2.22). The problem can be treated separately for the initial and the final state [78]. In the initial state, the photoelectron is bound to the nucleus, therefore it will be not much sensitive to the potential in the surrounding region and the term $V(\mathbf{r})$ can be neglected. The Schrödinger equation can be written as

$$H|i>=(-\frac{\hbar^2}{2m}\nabla^2-\frac{Ze^2}{r})|i>=E|i> \tag{2.23}$$

Limiting the description to K shell electrons (corresponding to the 1s orbital), the lowest energy solution of (2.23) is the hydrogenlike wave function

$$\psi_i(r)=<r|i>=N\exp^{-Zr/a_0} \tag{2.24}$$

In the final state the attractive potential of the central atom's nucleus, together with the influence of the other bound electrons, becomes negligible, and the Schrödinger equation reduces to

$$(-\frac{\hbar^2}{2m}\nabla^2+V(r))|f>=(H_0+V)|f>=E|f> \tag{2.25}$$

where H_0 is the free-particle Hamiltonian. This equation can be inverted by writing the final state wavefunction as a sum of a plane wave $|k>$ plus a perturbed term $|rest>$,

$$|f>=|k>+|rest> \tag{2.26}$$

$|k>$ is the free-electron wavefunction, therefore

$$H_0|k>=E|k>\Rightarrow(E-H_0)|k>=0 \tag{2.27}$$

The (2.25) can be thus rewritten as

$$(E-H_0)|k>+(E-H_0)|rest>=V|f>\Rightarrow(E-H_0)|rest>=V|f> \tag{2.28}$$

The (2.28) gives

$$|rest>=(E-H_0)^{-1}V|f> \tag{2.29}$$

The (2.26) can be then written as

$$\Rightarrow |f>=|k>+(E-H_0)^{-1}V|f> \tag{2.30}$$

and $|f>$ can be found by solving (2.30) iteratively

$$|f>=|k>+(E-H_0)^{-1}V|k>+(E-H_0)^{-1}V(E-H_0)^{-1}V|f> \tag{2.31}$$

In terms of the Green's function $G_0=(E-H_0)^{-1}$, the matrix elements of (2.20) can be finally written as

$$\begin{aligned} M_{if} &= |\langle\psi_i|\widehat{e}\cdot\mathbf{r}|\psi_f\rangle| = \\ &= |\langle k|\widehat{e}\cdot\mathbf{r}|i\rangle| + |\langle k|G_0V\widehat{e}\cdot\mathbf{r}|i\rangle| + |\langle k|G_0VG_0V\widehat{e}\cdot\mathbf{r}|i\rangle| + ... = \\ &= A_0 + A_1 + A2 + ... \end{aligned} \tag{2.32}$$

Considering the first two terms in the (2.32), one gets

$$|\langle\psi_i|\widehat{e}\cdot\mathbf{r}|\psi_f\rangle|^2 = |A_0|^2 + |A_1|^2 + 2Re(A_0A_1^*) \tag{2.33}$$

The first term in (2.33) is due to the absorption of the isolated atom, the other ones to the presence of the surrounding scatterers, and gives rise to the oscillations in the XAS spectrum.

2.1.2 Single Scattering Approximation and EXAFS Equation

The XAS spectrum, in the high energy region, the so-called EXAFS (Extended X-ray Absorption Fine Structure), is usually analyzed in terms of the $\chi(k)$ function

$$\chi(k)=\frac{\mu(k)-\mu_0(k)}{\mu_0(k)}, \tag{2.34}$$

which is the difference between the measured absorption coefficient $\mu(k)$ and the absorption of the corresponding isolated atom $\mu_0(k)$, normalized to $\mu_0(k)$. It is possible to show that in the single scattering (SS) approximation $\chi(k)$ can be written in the following form

$$\chi(k)=S_0^2\sum_i\frac{N_i}{kr_i^2}A_i(k)\exp(-2k^2\sigma_i^2)\exp(-2r_i/\lambda(k))\sin[2kr_i+\phi_i(k)] \tag{2.35}$$

where the sum is over each shell.
In the following, a simple heuristic derivation of this formula will be given [79] in order to highlight the physical meaning of each term. Considering the EXAFS qualitative picture, the oscillations in the absorption coefficient are produced by the interference between the outgoing and backscattered waves. The spherical outgoing wave is proportional to

$$\frac{\exp ikr}{r} \tag{2.36}$$

The wave outgoing from the i-th atom located in $\mathbf{r}_i$ is spherical as well

$$\frac{\exp ik|\mathbf{r}-\mathbf{r}_i|}{|\mathbf{r}-\mathbf{r}_i|} \tag{2.37}$$

The backscattered wave will then be proportional to (2.36), (2.37) and to a backward scattering amplitude $T_i(2k)$

$$T_i(2k)\frac{\exp ik\mathbf{r}_i}{\mathbf{r}_i}\frac{\exp ik|\mathbf{r}-\mathbf{r}_i|}{|\mathbf{r}-\mathbf{r}_i|} \tag{2.38}$$

In the origin, the backscattered wave will then be proportional to

$$T_i(2k)\frac{\exp 2ik\mathbf{r}_i}{\mathbf{r}_i^2} \tag{2.39}$$

The factor $2kr_i$ is the phase shift introduced by the wave traveling the distance $2r_i$ from the origin and the backscatterer. The electron does not move in a constant potential, so an additional phase shift, which is usually written in the form $[\delta_i(k)-\pi/2]$ has to be taken into account. The expression for the backscattered wave in the origin (2.39) becomes

$$T_i(2k)\frac{\exp 2ik\mathbf{r}_i+\delta_i(k)-\pi/2}{\mathbf{r}_i^2} \tag{2.40}$$

The real part of (2.40) is proportional to the $\chi_i(k)$:

$$\chi_i(k)=K\frac{T_i(2k)}{\mathbf{r}_i^2}\sin[2ik\mathbf{r}_i+\delta_i(k)] \tag{2.41}$$

This expression can be rewritten by imposing

$$\frac{m}{2\pi\hbar^2k^2}t_i(2k)=KT_i(2k), \tag{2.42}$$

thus giving

$$\chi_i(k) = \frac{m}{2\pi\hbar^2} t_i(2k) \frac{\sin[2ik\mathbf{r}_i + \delta_i(k)]}{(kr_i)^2} \tag{2.43}$$

In the single scattering approximation the effect of many scatterers is simply the sum of single $\chi_i(k)$, therefore

$$\chi(k) = \sum_i \chi_i(k) = \sum_i \frac{m}{2\pi\hbar^2} t_i(2k) \frac{\sin[2ik\mathbf{r}_i + \delta_i(k)]}{(kr_i)^2} \tag{2.44}$$

In order to write expression (2.35), a few more phenomena have to be taken into account. First, the lifetime of the excited photoelectron state, which depends on the lifetime of the hole in the atom (τ_h), which is usually in the range of femtoseconds) and on the finite lifetime of the photoelectron itself (τ_f) which is due to scattering from surrounding atoms. The sum of τ_h and τ_f represents the average time to lose coherence, e.g. the time during which interference phenomena giving rise to the EXAFS oscillation are present. It is naturally connected to a mean free path distance λ

$$\tau = \frac{\lambda}{v}, \tag{2.45}$$

where v is the electron velocity and is thus given by $v = \hbar k/m$. The effect can therefore be phenomenologically taken into account by inserting a mean free path term in the form $\exp(-2r_i/\lambda)$.

Another important point is the structural and thermal disorder. Given a structure, the contributions of the single atoms of a given shell will therefore not be exactly in phase. Under the hypothesis of a small gaussian disorder, a radial distribution of atoms centered on the average distance r_i is given by

$$f(r_i) \mid r_j = (2\pi\sigma_i)^{-1/2} \exp[-\frac{(R_i - r_j)^2}{2\sigma_i^2}] \tag{2.46}$$

This gives a further $N_i \exp(-2k^2\sigma_i^2)$ factor in the $\chi(k)$ expression.

Finally, the relaxation effect giving S_0^2 described in (2.21) has to be considered. By putting these elements together one finally obtains

$$\chi(k) = S_0^2 \frac{m}{2\pi\hbar^2} \sum_i N_i \frac{t_i(2k)}{r_i^2} \exp(-2k^2\sigma_i^2) \exp(-2r_i/\lambda(k)) \sin[2kr_i + \phi_i(k)], \tag{2.47}$$

which is, a part from constant terms, identical to (2.35). The terms N_i and r_i are directly connected with the coordination number and distances of the considered system, while the amplitude and phaseshift (respectively $t_i(2k)$ and $\phi_i(k)$ in this formula) are related to the chemical nature of the scatterers. DW factors are connected with the static and thermal disorder; they are usually assigned according to standard values, but also *ab initio* approach for their evaluation have been developed [80] [81]. When multiple scattering (MS) events have to be taken into account, an expression equivalent to (2.35) holds, but the sum is performed in this case over all the MS paths.

2.2 Experimental Overview

In this section, a general description of the experimental apparatus necessary for a XAS experiment is given. Here below there is the scheme of a typical beamline (Fig. 2.5). A brief description of the photon source is followed by the analysis of optical components and detectors. A paragraph is dedicated to the analysis of

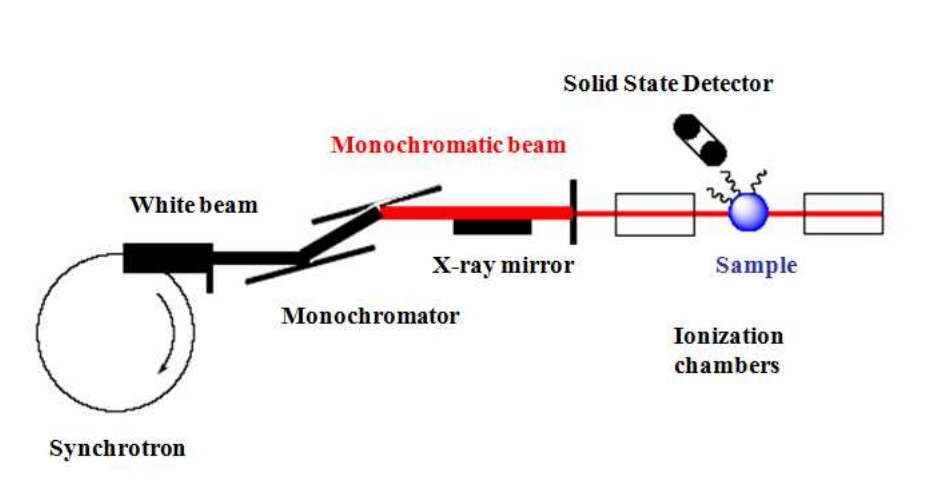

Figure 2.5: Scheme of a standard XAS beamline.

different experimental geometries and to the description of their main features.

2.2.1 Synchrotron Radiation

Two are the features of synchrotron radiation (SR), generated by the accelerated motion of electrons, that make it very powerful to measure the absorption coefficient μ as a function of the energy of incoming photons: the broad energy spectrum and its high intensity in the x-ray region.
SR was observed for the first time in 1947 as a dissipation effect in the General Electric synchrotron in the USA. In the fifties it was considered just a problem for particle physics experiment since it is a source of energy loss in accelerators, but in the sixties it was understood that SR could be a powerful tool for condensed matter research. At the beginning SR was used in a parasitic way during high energy physics experiments (first generation radiation facilities). The second generation machines, which were dedicated to the production of synchrotron

light by bending magnets, were built in the '70. The machines widely used nowadays, in which the light is produced not only by bending magnets, but also by insertion devices such as wigglers and undulators, belong to the third generation. A wiggler is a multipole magnet made up of a periodic series of magnets which force the electrons to wiggle around a straight path. Electrons follow in this way a curved trajectory with a smaller local radius of curvature with respect to a bending magnet. The emitted radiation is the incoherent sum of the radiation emitted by each individual pole, therefore the total intensity linearly depends on the number of poles.
Undulators are very similar to wigglers, but in this case the wiggling angle is close to the photon natural emission angle. There are therefore interference phenomena between the photons emitted at different points along the orbit. The emitted radiation is mainly composed by a fundamental wavelength whose intensity is proportional to the square of the number of poles.
Insertion devices highly improve the brilliance of synchrotron radiation, but many efforts are still being taken to develop a new generation of synchrotron radiation sources with vastly enhanced performance. The candidate with the best scientific case for a fourth generation source is the hard x-ray free-electron laser (FEL) based on a very long undulator in a high-energy electron linear accelerator. Such a device can have a peak brightness many orders of magnitude beyond that of the third generation sources, as well as pulse lengths of 100 fs or shorter, and can be fully coherent. However, the application of FELs to the XAS and other spectroscopical techniques is not straightforward. Among other difficulties, the photon energy cannot be easily tuned to obtain an absorption spectrum. On the other side, the very high brilliance and short pulse length of FEL radiation could allow to perform new experiments using other standard synchrotron radiation based techniques, for example by push towards the single molecule limit the X Ray Diffraction, as shown by recent pioneristic experiments [83] [84].
As already mentioned, the main properties of synchrotron radiation, which make it ideal for the XAS experiments, are the high intensity, the broad and continuum spectral range and its narrow angular collimation. These features are quantitatively represented by a parameter, the brilliance [85], which is directly proportional to the number of emitted photons (F) and indirectly proportional

to source size (S_x, S_y) and angular spreads (θ_x, θ_y).

$$Brilliance \propto \frac{F}{S_x S_y \theta_x \theta_y} \tag{2.48}$$

Therefore a source can be made brighter by increasing the flux, by decreasing the size or enhancing the angular collimation. The brilliance of a few exemplary sources is reported in Fig. 2.6.
Furthermore SR is polarized and has a pulsed time structure. This last property is not of immediate interest for standard XAS measurements, but allows to design time-resolved experiments, which are nowadays getting more and more common because they allow to explore a variety of phenomena in different branches of science.
The detailed properties of the emitted beam depend on the characteristics of the storage ring, therefore for each experiments the best source, among the many (about 70) which are nowadays available, has to be carefully chosen.

2.2.2 X-ray Optics and Detectors

A beamline for x-ray spectroscopy is usually composed of the optical apparatus, namely the monochromator and the x-ray mirrors, and the measurement apparatus, namely the sample holder and the detectors[86].
The monochromator is used to select the appropriate beam energy, $E = \hbar\omega$, from the synchrotron radiation spectrum, and to scan over the required energy range (which is usually of the order of 800 eV). The most common kind of monochromator is a crystal where the energy is selected by exploiting the Bragg law

$$2d_{hkl} sin\theta_b = n\lambda \tag{2.49}$$

where d_{hkl} is the distance between the (hkl) crystallographic planes, θ_b is the incidence angle, n is an integer and λ is the wavelength. The energy scan is obtained by rotating the crystal around an axis parallel to the Bragg planes and normal to the beam direction. For x-ray with energy higher than 2keV, the crystals most frequently used are Si and Ge. In order to have the outgoing beam in the same direction of the incoming one, a geometry with two Bragg reflections

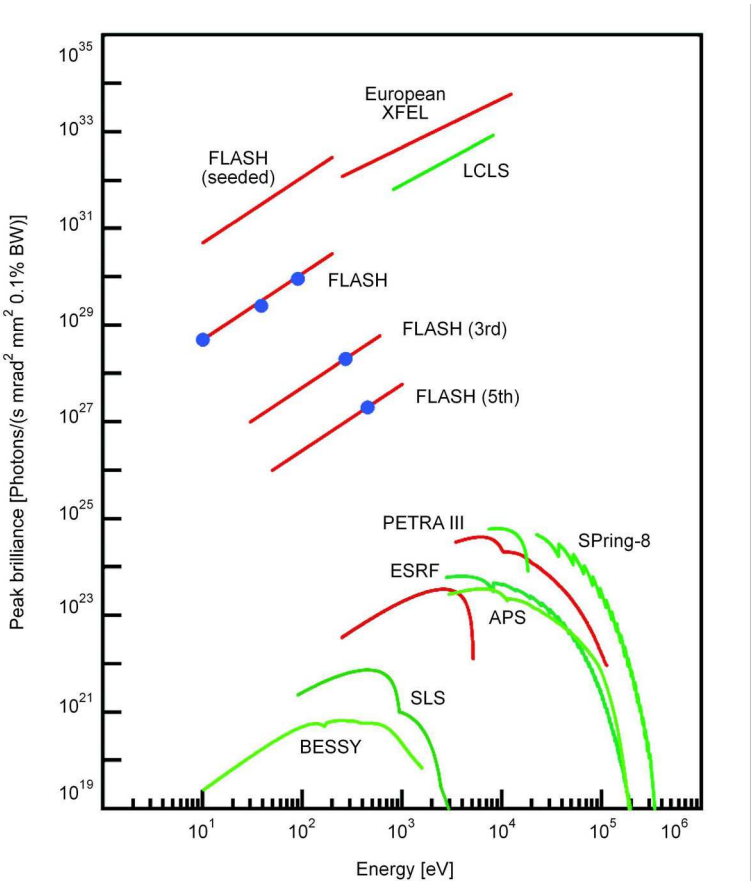

Figure 2.6: Brilliance of storage ring and FEL light sources.

is usually used (see Fig. 2.7).

Equation (2.49) tells that also harmonics higher than the fundamental ($n > 1$) are reflected, and this is a source of noise for the XAS. This problem is present when channel-cut monochromators (Fig. 2.8), i.e. single monocrystals machined in order to have two perfectly parallel reflecting faces, are used. They are however sometimes used because they are relatively simple to realize and mechanically stable.

To overcome this problem, independent crystal monochromators, made of two different crystals, although being more expensive and difficult to set up, are widely used. They exploit the fact that the X-ray beam is diffracted by the crystal within a finite angular interval around the Bragg angle. The profile of the diffracted intensity as a function of the angle is called rocking curve, and its profile depends on the wavelength. In particular, the longer λ is, the larger

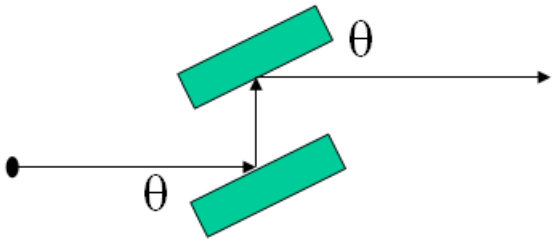

Figure 2.7: Scheme of a typical monochromator.

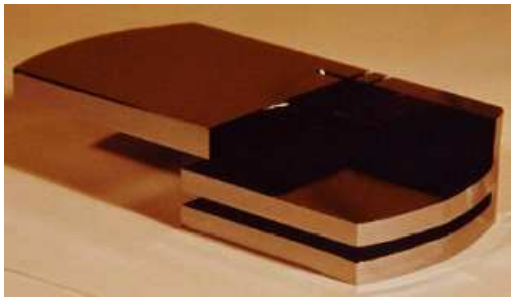

Figure 2.8: A channel-cut monochromator.

the interval around θ_b (Darwin width, ω_d, see Fig. 2.9) over which the beam is reflected is. Therefore a slightly detuning of the parallelism between the Bragg planes of the two crystal allows to reflect only the fundamental harmonic, which has the smallest Darwin width.

The radiation reflected by the monochromator is usually focused using x-ray mirrors, which work exploiting the phenomenon of total reflection. The critical angle for total reflection is a growing function of the wavelength, therefore by properly choosing the incidence angle of the beam on the mirror it is possible to operate the higher harmonics rejection.

In order to measure the absorption coefficient, the intensity of the focused beam has to be measured before it impinges on the sample. The intensity of incoming radiation is usually measured using ionization chambers. Depending on the energy range in which the chamber have to work, it is filled with appropriate gas mixtures and pressures. In particular, the higher the energy is, the higher gas pressure has to be to compensate for the decreased efficiency. It is worth noting that, being placed before the sample, this ionization chamber should not absorb

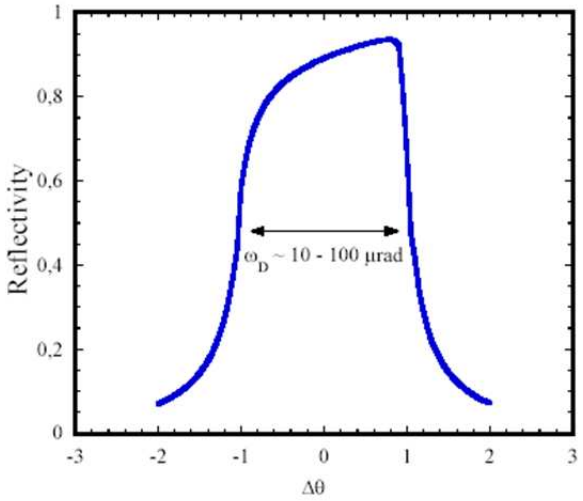

Figure 2.9: Darwin width put in evidence in a typical rocking curve.

too many photons. Usually it is set to absorb about 20% of the incident radiation. An example of typical gas mixtures and pressure used is given in Table 2.1.

After the I_0 detection, the monochromatic x-ray beam impinges on the sample.

Metal	K-edge Energy (eV)	Pressure (mBar)	Gas Mixture
Mn	6539	150	$70\%Ne + 30\%CO_2$
Fe	7112	250	$70\%Ne + 30\%CO_2$
Zn	9660	600	$70\%Ne + 30\%CO_2$
Br	13500	950	$70\%Ne + 30\%CO_2$
Sr	16100	600	$70\%Ar + 30\%CO_2$

Table 2.1: Gas mixtures and pressures used at the EMBL D2 beamline for different metals K-edge.

The XAS spectrum can then be acquired in different experimental setups, each one allowing to measure a quantity related to the absorption coefficient.

Transmission

The intensity of transmitted radiation is usually measured by a second ionization chamber. In order to maximize the absolute efficiency of this second detector, the I ionization chamber is usually longer than the I_0 one and it is filled with gases at higher pressures.

Fluorescence

Fluorescence radiation is usually measured by solid state detectors. This kind of detectors is used because a good energy resolution is required in order to separate fluorescence contributions form backscattered radiation. In addition, solid state detectors have higher efficiency than gas detectors. They exploit semiconductors band structure. An n-doped region is created next to a p-doped region; in between there is a depletion region without any charge carrier. Applying an inverse polarization to the np junction (p-, n +), the depletion region width can be increased thus increasing the sensible volume of the detector. The ionizing radiation impinging on this zone generates electron-hole couples which are accelerated towards the sides of the junction. An electric current proportional to the ionization obtained in the depletion region (and therefore to the number and energy of impinging photons) is then generated.

The average energy required to generate an electron-hole pair is 3.6 eV for Si and 2.98 eV for Ge. At $T > 0K$ there is a thermal generation of electron-hole couples, therefore the concentration of electrons (or holes), n, is not zero and it is given by:

$$n = \sqrt{N_C N_V}\ e^{\frac{-E_{gap}}{2kT}}, \tag{2.50}$$

where E_{gap} is the energy gap between the conduction and valence band of the considered semiconductor and N_C and N_V are the density of electron in the conduction and valence band, respectively. The detector has to be kept at low temperature (usually at liquid nitrogen temperature) in order to reduce the thermal background.

Another problem of solid state detector is the relatively low rate of counts they can deal with. Usually they can measure in the range of $1 - 2 * 10^5$ photons/s. To usefully exploit the high counting rates available with synchrotron radiation, multi-element arrays of 4-30 elements have been developed and are widely used. Solid state detectors are usually placed at 90° with respect to the beam in or-

der to minimize the number of backscattered photons. Anyway, the signal is usually dominated by backscattered photons, which are the main responsible of detector saturation (see Fig. 2.10). In order to deal with this problem, detectors are mounted on slits in a way that their distance from the sample can be adjusted, thus allowing to remain just below the saturation limit in each experiment. In order to separate the signal (fluorescence radiation) from the back-

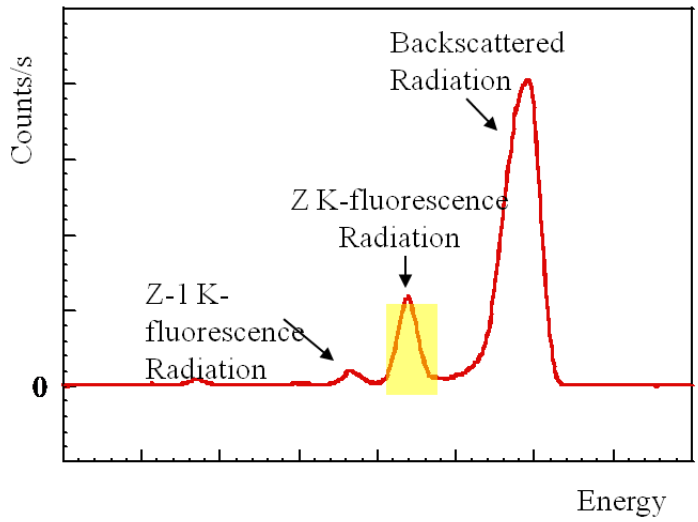

Figure 2.10: Typical behavior of the number of photons revealed by the detector as a function of detection energy.

ground (backscattered radiation), the energy resolution has to be significantly smaller than the energy difference between the backscattered and the fluorescence radiation. For relevant biological metals this difference is usually smaller than 1 keV, e.g. in the case of Mn the K-edge is located at 6539 eV and the Kα_1 emission is 5899 eV. K-edge and Kα_1 energies for some relevant metals are reported in Table 2.2.

Electron yield

In electron yield measurements the flux of electrons emitted by the sample, which is proportional to the absorption coefficient, is measured. It is possible to detect only the Auger electrons emitted for non-radiative decay (Auger Electron Yield, AEY) or all the electrons emitted by the sample (Total Electron Yield, TEY). To this purpose, electrometers are widely used.

Element	K-edge (eV)	Kα_1(eV)
Mn	6539	5899
Fe	7112	6404
Co	7709	6930
Ni	8333	7478
Cu	8979	8048
Zn	9659	8639

Table 2.2: K-edge and Kα_1 energies for some relevant metals [87].

Since electrons have a short mean free path, only those generated in the vicinity of the surface are detected (i.e. the sampling depth of XAS in this configuration is small). For this reason, electron yield is usually used to study surface properties, but it is not common to study bulk properties. However, in XAS experiments with light atoms electron yield measurements can be preferred, because in this Z-region the fluorescence yield is low (see Fig. 2.3).

2.2.3 Experimental Setup

Each of the detection modes described in the previous section 2.1.1 can be used to acquire a XAS spectrum[88]. The choice among them is determined by sample features, in particular by the energy of the considered absorption edge, by it concentration, by its geometrical structure (e.g. thickness), and by the information one is interested in (e.g. bulk or surface information)[89].

Transmission Geometry

According to equation (2.1), in the transmission geometry the intensity of the transmitted radiation, I, is given by

$$I = I_0 \exp(-\mu_t d) = I_0 \exp(-(\mu_A + \mu_B)d) \tag{2.51}$$

where the total absorption coefficient μ_t is given by the sum of solute, μ_A, and solvent, μ_B, absorption coefficients.

$$\mu = \mu_A + \mu_B \tag{2.52}$$

I varies with μ_A as

$$|\Delta I| = I_0(1 - e^{(\mu_A+\mu_B)d})\Delta\mu_A d \tag{2.53}$$

Therefore, if one wants to have I/I_0 ratio $\simeq 1/10$, the condition

$$\mu_t d \simeq 2 \tag{2.54}$$

must be satisfied, thus finally giving

$$\frac{I}{|\Delta I|} \simeq \frac{\mu_t}{2}\frac{1}{\Delta\mu_A} \tag{2.55}$$

Statistically the error on I can be estimated by

$$|\Delta I| \simeq \sqrt{I} \Rightarrow \frac{I}{|\Delta I|} \simeq \sqrt{I} \tag{2.56}$$

Using equations (2.51), (2.54) and (2.56) one gets

$$\frac{I}{|\Delta I|} \simeq \frac{\sqrt{I_0}}{e} \tag{2.57}$$

By comparing (2.55) and (2.57) one obtains

$$[\frac{\mu_A}{|\Delta\mu_A|}]_T = \frac{2\sqrt{I_0}}{e}\frac{\mu_A}{\mu_t} \tag{2.58}$$

Under the assumption that the absorbance cross sections of the solute, σ_A, and solvent, σ_B, molecules are of the same order of magnitude one has

$$[\mu_A = \sigma_A n_A \Rightarrow \mu_t = \sigma_t n_t \approx \sigma_A n_t \tag{2.59}$$

and

$$[\frac{\mu_A}{|\Delta 1\mu_A}]_T \approx \frac{2\sqrt{I_0}}{e}\frac{\mu_A}{\mu_t} = \frac{2\sqrt{I_0}}{e}R \approx R \tag{2.60}$$

where $R = n_a/n_t$ is the so called dilution ratio. Equation (2.60) shows that the accuracy, $\frac{\Delta\mu_A}{\mu_A}$ gets better as R increases.

Fluorescence Geometry

The intensity of the fluorescence is given by [90]

$$I_F = I_0(1 - exp[-\mu_t(E) - \mu_t(E_F)]d)\epsilon\frac{\Omega}{4\pi}\frac{\mu_A(E)}{\mu_t(E) + \mu_t(E_F)} \tag{2.61}$$

where $I_0(1 - exp[-\mu_t(E) - \mu_t(E_F)]d)$ is the absorbed intensity, ϵ is proportional to the fluorescence yield, Ω is the solid angle over which the photons are acquired, E and E_f are the energies of the absorbed and fluorescent photon respectively. It is interesting to study the behavior of fluorescence equation in two limit cases: -High concentration, thin sample, namely:

$$[\mu_t(E) + \mu_t(E_F)]d << 1 \tag{2.62}$$

thus having

$$I_F \approx I_0 \epsilon \frac{\Omega}{4\pi} \mu_A(E) d \tag{2.63}$$

By using (2.56) one gets

$$\frac{\mu_A}{\Delta\mu_{A\,F}} \approx [I_0 \epsilon \frac{\Omega}{4\pi} \mu_A(E) d]^{1/2} \tag{2.64}$$

-Low concentration, thick sample, namely:

$$[\mu_t(E) + \mu_t(E_F)]d >> 1 \tag{2.65}$$

one has

$$\frac{\mu_A}{\Delta\mu_A} \approx [\frac{I_0 \epsilon \frac{\Omega}{4\pi} \mu_A d}{2\mu_T}]^{1/2} = [\frac{I_0 \epsilon \frac{\Omega}{4\pi}}{2}]^{1/2} [\frac{n_A}{n_T}]^{1/2} \sim R^{1/2} \tag{2.66}$$

By using again (2.56) one gets

$$\frac{\mu_A}{\Delta\mu_A} \approx [I_0 \epsilon \frac{\Omega}{4\pi} \mu_A(E) d]^{1/2} \tag{2.67}$$

The accuracy of absorption geometry and fluorescence geometry is similar when

$$[\frac{\mu_A}{\Delta\mu_A}]_T = [\frac{\mu_A}{\Delta\mu_A}]_F \Rightarrow R = \frac{e^2}{8\pi} \epsilon \frac{\Omega}{4\pi} \tag{2.68}$$

In order to see which geometry is better at a given concentration, it is useful to use realistic numerical values for the efficiency of the detector, e.g. $\epsilon \approx 0.4$, and for the solid angle used for the acquisition, e.g. $\epsilon \approx 0.1$. One gets

$$R \approx 10^{-2} \Rightarrow [\frac{\mu_A}{\Delta\mu_A}]_T / [\frac{\mu_A}{\Delta\mu_A}]_F \approx 2 \tag{2.69}$$

$$R \approx 10^{-3} \Rightarrow [\frac{\mu_A}{\Delta\mu_A}]_T / [\frac{\mu_A}{\Delta\mu_A}]_F \approx 6 \tag{2.70}$$

$$R \approx 10^{-4} \Rightarrow [\frac{\mu_A}{\Delta\mu_A}]_T / [\frac{\mu_A}{\Delta\mu_A}]_F \approx 20 \tag{2.71}$$

This easily leads to the conclusion that fluorescence geometry has to be preferred when dealing with low concentrated (less than 10^{-2}) samples.

Electron Yield Geometry

The considerations made for the fluorescence geometry also hold for non-radiative (Auger or total electron yield) detection, except that in the latter case the sampling depth is determined by the electron escape depth, which is typically much smaller than the total sample depth.

2.3 XAS data Analysis

As shown in the previous sections, an XAS spectrum essentially consists in the value of the absorption coefficient μ measured at different energies. In order to perform qualitative and quantitative analysis, it is necessary to put the raw spectra in a form which is independent on experimental setup. After this step, both the low- and high-energy regions can be analyzed to extract the structural and chemical information about the local environment around the absorbing atom.
The data reduction can be performed following many different strategies; in the first paragraph the procedures used for the work presented in this thesis are described. In the last two paragraphs a basic description of XANES and EXAFS regions, focused on possible data analysis strategies, will be given.

2.3.1 Signal Extraction and Data Reduction

In order to obtain a quantitatively analyzable signal, or simply to compare spectra acquired in different conditions or with different absorber concentration, a data reduction procedure is necessary [91].
First of all, the edge energy E_0 has to be identified, and this can be done by locating the energy point which corresponds to the maximum of first derivative. In the cases when the edge shape is sharp, this procedure allows to obtain rather unambiguous results, while the situation is more complicated when there edge region is more structured.
A linear fit of the pre-edge region is then calculated and subtracted from the spectrum. This operation allows to isolate the main contribution to the absorption coefficient from all the other excitations of the selected element and from the excitation of the other elements of the compound. The region below the edge is indeed affected by lower energy absorption edges, Compton scattering and other processes that are not of immediate interest. The value of the fitted straight line evaluated at E_0, $\mu_1(E_0)$ is also extrapolated.
Then, the post-edge region is fitted with a quadratic polynomial, and the value

of this polynomial is extrapolated at E_0, $\mu_2(E_0)$. The difference

$$\delta = \mu_2(E_0) - \mu_1(E_0) \tag{2.72}$$

is then computed. δ is proportional to the concentration of the absorbing atom in the samples. Therefore, in order to compare spectra with different concentrations it is necessary to normalize them. This is done by dividing each point of the spectrum by δ, thus obtaining a jump between the pre-edge and the post-edge region equal to 1. An example of this procedure is given in Fig. 2.11.

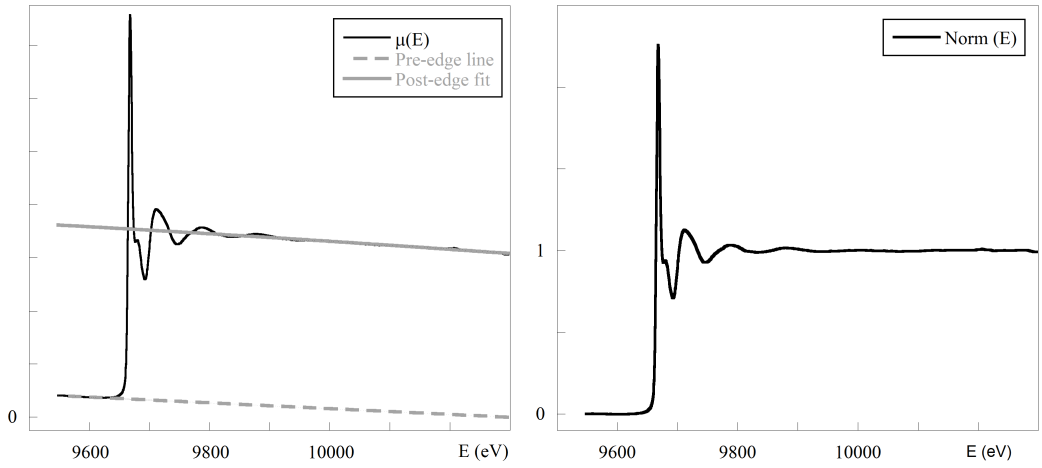

Figure 2.11: Left Panel: Pre-edge and post-edge fits - Right Panel: Normalized spectrum.

The normalization procedure allows therefore to get information on the concentration of the absorbing atom in the sample. Indeed the measured absorption coefficient is proportional to the number of atoms which absorb the incoming photons and therefore to the jump δ. If a standard sample with a known concentration of the absorbing atom is measured in exactly the same geometry (i.e. with sample and detector left in the very same position), it is then possible to give an estimation of the concentration of the absorber concentration in other samples:

$$[unknown] = [standard]\frac{\delta(unknown)}{\delta(standard)} \tag{2.73}$$

A further step in data reduction is the extraction of the $\chi(k)$ function (2.34),

which is by definition the oscillatory part of the signal not due to the isolated atoms. The absorption of the isolated atom is usually approximated by a smooth fit of the post-edge region. The most common approach is to use a few (4-6) cubic splines to fit this region, assuming that they well represent the behavior of $\mu_0(E)$. Of course, this definition of $\mu_0(E)$ is somehow arbitrary, so it is necessary to carefully check that this background subtraction operation does not add spurious components to the $\chi(k)$ signal. A typical $\chi(k)$ is plotted in Fig. 2.12

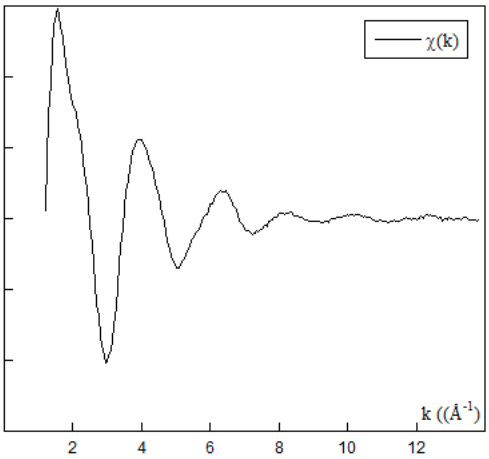

Figure 2.12: Typical $\chi(k)$.

2.3.2 XANES Region

The XANES region is dominated by MS processes because of the low kinetic energy of the photo-electron, which therefore undergoes more than one scattering event either with different scatterers or more than once with the same scatterer. In principle the XANES contain detailed information about the local atomic structure around the absorber. Unfortunately these potentialities can not yet be fully exploited, because of the difficulty of setting up a reliable theoretical analysis of this energy region. There is, in fact, quite a number of reasons why it is problematic to describe this part of the spectrum or extend to it the procedure used in discussing the EXAFS region (see below). Among them one may mention the inadequacy of the muffin-tin approximation to the inter-atomic potential at low photoelectron energies, the lack of a satisfactory description of screening and

relaxation processes following the sudden creation of a core hole, the need of including electronic correlations and, in particular, two-electron excitations, etc.. Because of the difficulties in modeling in an adequate way these complicated processes, the analysis of the XANES region has remained for a long time at a semi-qualitative level. Nevertheless many theoretical and computational progresses have been made in the last few years, and many programs are nowadays available which are able to calculate a XANES spectrum (MXAN [92], Feff [93], FDMNES[76]). The application of these programs is getting wider and wider and it has given valuable results also in selected biological cases[94].
A strong limitation for the use of this fully quantitative approach is the requirement of a reliable structural starting model in order to start the calculation. When a good starting model is not available, a qualitative analysis of the XANES region can still be performed, which provides useful information on the oxidation state and on the local symmetry around the absorber.
A semi-quantitative analysis of the XANES can be also used when dealing with samples in which the absorbing atom is present in more than one structure. The key observation is that in this situation the spectrum can in principle be obtained as the sum of model compound spectra, weighted by the percentage of the absorbing atom present in each component [95]. Of course, care must be taken to ensure the use of model systems which reflect as nearly as possible the chemical nature of the sites to be investigated. If carefully used, this approach allows therefore to obtain quantitative information on the composition and structure of in principle any non homogenous system.
A similar approach is possible when, although a fully quantitative XANES calculations is not feasible, the local geometry around the absorbing atom is not completely unknown. In this case, it is possible to perform XANES calculations for a few models with selected structural features (e.g. distances, bond angles, coordination numbers). Then, a fit of the experimental spectrum can be made using the calculated theoretical spectra as components. In this way, it is possible to obtain an estimation of the local atomic structure parameters reducing the number of time-consuming calculations which are in principle required to find optimal values of the parameters[96].

2.3.3 EXAFS Region

The EXAFS region contains information on the type, number, distance and in principle geometry around the absorber. The kinetic energy, E_k, of the photoelectron in this region is larger than in the XANES region, therefore single scattering events are dominant and the photoelectron is a less sensitive probe for geometrical parameters.
At these comparably higher energies, however, MS contributions, that are richer in structural information, are still present and can be taken into account in analyzing experimental data. In particular, Teo [97] and Boland [78] pointed out that when three atoms are aligned, the associated MS contribution become important. This forward-scattering configuration, called shadowing (or focusing) effect, can be therefore used to determine geometries where three atoms are aligned or almost aligned. Main MS contributions associated with this geometry are shown in Fig. 2.13.

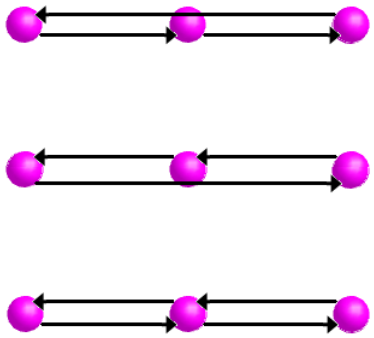

Figure 2.13: Double and Triple (lower graph) scattering paths for 3 aligned atoms.

Theoretical approaches giving a rigorous quantum-mechanical description of the EXAFS signal, including both single and multiple scattering terms, have been implemented in a number of packages among which gnXAS [98], FEFF [93] and Excurve [99] [115].
The inclusion of MS terms in the analysis of XAS data is especially important in investigating the structure of the active site in a metal-protein. Amino acidic residues are, in fact, almost completely composed by light atoms (i.e. nitrogen,

oxygen and carbon atoms) and their contributions to the total XAS signal are indistinguishable from one another. Including MS contributions can help in some cases to overcome this limitation. The magnitude of the contributions coming from the presence of amino acids around the metal absorber, in fact, turns out to depend not only on the kind and mean distance of the atomic scatterers, but also on their specific geometrical arrangement.
A well known and biologically relevant example is represented by the case of the Histidine (His). The presence of this residue bound to a metal may be identified in a XAS spectrum because the contribution it gives to the signal through MS events is strongly enhanced owing to the interference (focusing effect) resulting from the collinearity of the atoms belonging to the His imidazole ring with the absorbing atom [101], see Fig. 2.14.
XAS is often the ideal tool for the study of metal-protein complexes in general, and in particular in those cases where crystal structures are not available [104] [102] [103]. As in the case of XANES, in order to get a quantitative interpreta-

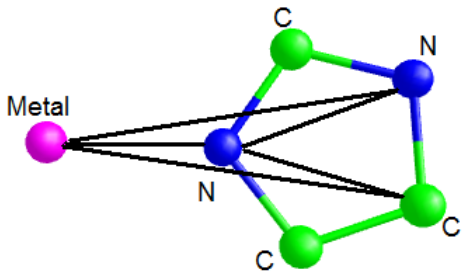

Figure 2.14: Main MS contribution associated with the Histidine imidazole ring.

tion of an EXAFS signal, a reasonable starting model has to be built. Starting from the chosen model, the physical parameters which are present in the EXAFS equation can be computed. The structural parameters are obtained by letting them vary while the difference between the theoretical and experimental spectrum is minimized.
The total number of parameters which can be determined depends on the energy range in which the $\mu(E)$ is registered. Namely, the maximum number n_{ind} of independent parameters is computed through the formula

$$n_{ind} \simeq \frac{2}{\pi}\Delta k \Delta r, \tag{2.74}$$

where $\Delta k = k_{max} - k_{min}$ is the interval in k and $\Delta r = r_{max} - r_{min}$ is the interval of the r space in which valuable signal is present.

When dealing with biological samples where, due essentially to the presence of only light scatterers, the $\chi(k)$ oscillations rapidly and monotonically decrease with k. The spectrum is therefore normally multiplied by a k^n, with n ranging between 1 and 3 [105].

In order to have a qualitative view of an EXAFS spectrum, it is worth looking at its Fourier transform (FT), which is obtained as

$$F(r) = \int_{k_{min}}^{k_{max}} \chi(k) W(k) k^n \exp(2ikr) dk, \tag{2.75}$$

where W(k) is a window function which reduces the spurious oscillations induced by the finite k range. The modulus of F(r) is characterized by the presence of peaks centered around the distance of each coordination shell or MS paths. In particular, a qualitative inspection of the FT could help in the definition of the local environment around the metal. For example, the presence of His residues can be suggested by the presence of peaks at characteristics distance in the FT, whose shape and relative intensity is also sensitive to the orientation of the imidazole ring with respect to the absorbing atom [106].

It should be noted that peaks positions do not correspond to the physical distance and this is due to the presence of a phaseshift term, ϕ_i, in the EXAFS equation (2.35). The shift amounts to few tenths of Å (0.2-0.5Å) toward lower r values. Qualitatively, the height of each peak is related to the number of atoms present in each shell and to the corresponding DW factor.

Chapter 3

Experimental Results

In this chapter I will describe the main experimental results of my thesis work. The chapter is subdivided in three sections that correspond to the three classes of studied systems.
The first section of the chapter is focused on the of Aβ peptides in complex with Cu and Zn ions.
The second one is about the effect of Zn ions on the Cu coordination mode in PrP octarepeat subdomain.
The last section is about XAS measurements performed at sulfur K-edge on human neuromelanin and synthetic analogous compounds.

3.1 Cu and Zn Aβ complexes

The work presented in this section [107] is aimed at identifying the Cu and Zn binding sites in $A\beta$ peptide. In particular, an important issue is to understand wether these metal ions have the same binding site and how their binding mode is related to the peptide oligomerization and/or aggregation properties, e.g. by promoting inter- or intra-peptide coordination modes. In designing the experiment and analyzing its results data available in the literature, coming from other techniques, are taken into account (see paragraph 1.3.4).
Sample preparation and characterization are done in collaboration with people from CNR-Trento, in particular Cristina Potrich and Mauro Della Serra. XAS data were acquired (at the EMBL Hamburg BioXAS dedicated beamline D2) and analyzed in collaboration with Wolfram Meyer-Klaucke.

3.1.1 Sample Description

Fragments of Aβ peptides of various lengths have been considered in order to identify the metal binding sites, to determine the minimal sequence able to bind metal ions and to clarify the role played by the different regions of the peptide. Aβ(1-16), Aβ(1-28), Aβ(1-40) and Aβ(17-40) have been bought from AnaSpec Inc. (purity index $> 95\%$). Aβ(5-23) has been synthesized by the Trento group by solid phase synthesis using a ResPep synthesizer (Intavis), further purified by reverse phase high pressure liquid chromatography on a C18 column (Phenomenex), and checked for its molecular mass by electrospray ionization-mass spectrometry. All peptides are solubilized in hexafluoroisopropanol (HFIP) to obtain stock solutions at the concentration of 2 mg/m, that have been frozen and stored at -20°C.
As reported in section 1.3.1, the peptides with the highest biological relevance are Aβ(1-40) and Aβ(1-42), namely those found in amyloid plaques. However, Aβ(1-42) peptide is known to aggregate very quickly and therefore it is not suitable for the kind of study presented here, which is mainly focused on the early steps in the aggregation process. The following fragments have been studied:
-The full length Aβ(1-40) peptide, which is one of the main components of amyloid plaques;

-The fragment Aβ(1-16) which, according to various studies, should represent the minimal metal binding sequence;
-The fragment Aβ(1-28) which, besides including the minimal binding sequence, has a long hydrophobic region that is believed to be relevant in the aggregation processes;
-The fragment Aβ(5-23) that still includes the minimal binding sequence, but is deprived of the first 4 residues of the Aβ and is then useful to check wether those latter are involved in metal binding;
-The fragment Aβ(17-40) which does not include the minimal metal binding site. Note that this fragment corresponds to the non pathological peptide P3 (see 1.3.1).
All the peptides have been subjected to measurements using various (standard) techniques in order to study their aggregation propensity and their secondary structure, both in the absence and in the presence of metal ions, and finally to XAS experiments to determine the structure of Cu and Zn binding sites.

3.1.2 Optical Density Measurements

The aggregation propensity of the peptides has been studied by measuring the absorbance at 220 nm, which is the wavelength characteristic of the peptide bond. At this wavelength the absorbance is proportional to the concentration of the peptide dissolved in solution and decreases when a fraction of the peptide precipitates [108] [109].
The peptides are dissolved in Tris-HCl 20 mM at pH=7.4, then centrifuged at 4°C, 10000g for 15 minutes (using a fixed angle rotor in an Optima TL100 Beckman Centrifuge), in order to remove from the solution any possible preexisting complex. Then the concentration of the peptide in the supernatant is estimated. The supernatant containing soluble Aβ peptide is then mixed with Tris buffer alone or buffer containing 70 μM concentration of Cu or Zn ions. The final concentration of peptide in each test sample is about 20 μM. After this operation, the supernatant is subdivided into 4 aliquots. The optical density of the first aliquot, OD_0, is immediately measured. The remaining 3 aliquots are incubated for 30 minutes at 37°C and then centrifuged at 4°C and 10000g for 15 minutes.

The optical density, OD, of the supernatant is then read. The OD of the sample that was kept refrigerated on ice is successively measured to estimate the amount of aggregation occurring at 0°C, which is found to be negligible. The aggregation percentage is then calculated using the simple following formula

$$\%Aggregation = 100\frac{OD_0 - OD}{OD_0} \tag{3.1}$$

The results of the experiments above are shown in Fig. 3.1. The aggregation

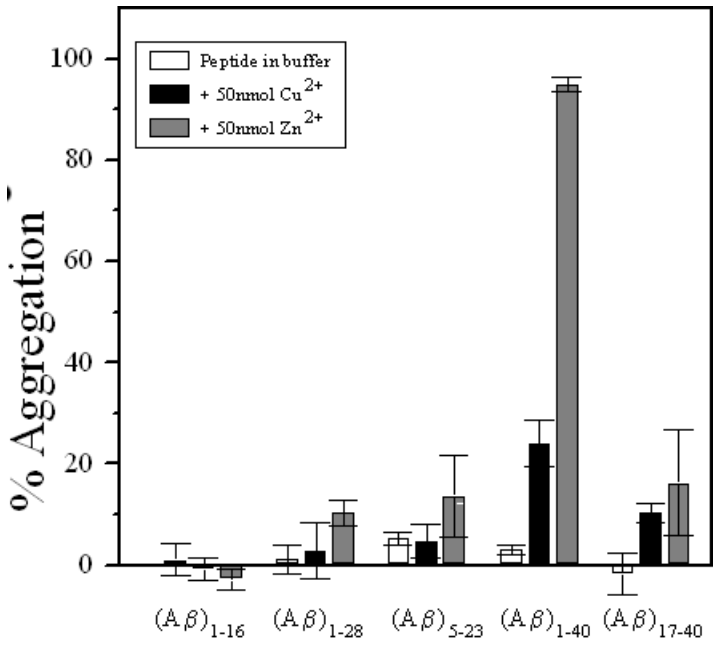

Figure 3.1: Aggregation of $A\beta$ in the absence (white boxes) of metal ions and in the presence of either Cu(black boxes) or Zn(gray boxes) ions.

propensity strongly depends on the considered fragment. In the absence of metal ions (white boxes), the aggregation level is zero in the peptides Aβ(17-40) and Aβ(1-16) and it is barely outside the error bars in the peptides Aβ(1-40) and Aβ(5-23).

Either in the presence of Cu (black boxes) or Zn (grey boxes) ions (see Fig. 3.1), data show a significant increased aggregation propensity. This behavior is particulary evident for the full length Aβ(1-40) peptide, but it is observable also for the shorter fragments, with the exception of Aβ(1-16). It is worth noting that

Zn is always more effective than Cu in promoting aggregation. For example, in the case of Aβ(1-40) the peptide aggregation is found to be about 25% in the presence of Cu and this percentage increases till 90% in the presence of Zn.
These data clearly show that both Cu and Zn ions have an effect (even if at different levels) on the Aβ aggregation process.
In order to better understand the effect of metal ions in Aβ aggregation, the OD measurements have been performed also in the presence of metal chelators. The Aβ peptide used in these experiments is Aβ(1-42), which has been chosen because it is the one which has the highest aggregation propensity both in the absence and in the presence of metal ions. In this kind of experiments, both the metal ions (Cu or Zn) and the chelating agents are co-added to the samples before starting the incubation. The chelating agents are chosen among molecules of therapeutic use already tested in the case of poisonings from heavy metals: DETPA (diethylentriaminepentaacetic acid), that is active on Cd, Zn and Cu; succimer (dimercaptosuccinic acid), that is useful in the cases of saturnism and hydrarginism; penicillamine, which is a wide range chelator [110]. As shown in

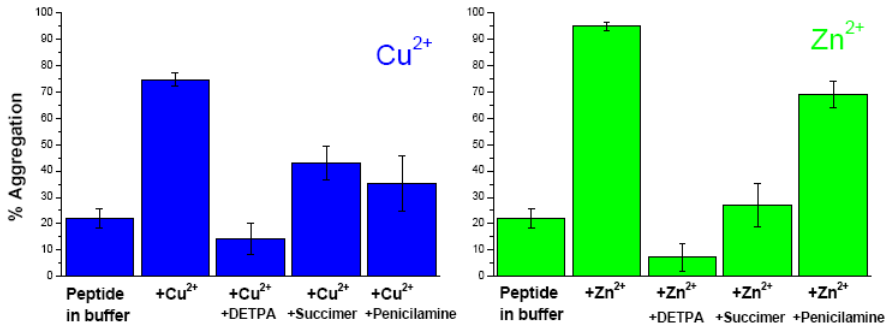

Figure 3.2: Preventive effects of three different chelators on Cu (left panel) and Zn (right panel) induced Aβ peptide aggregation.

Fig. 3.2, DETPA turns out to be the best chelator for preventing aggregation, succimer has intermediate effectiveness, while penicillamine is only effective with Cu. An important observation which can be derived from these measurements is that Cu is always withheld more strongly than Zn.

3.1.3 FTIR Measurements

$A\beta$ peptides secondary structure is determined by FTIR, as described in [111]. FTIR spectra are collected by using a Bio-Rad FTS 185 instrument. Typically 64 interferograms are acquired for each sample, Fourier transformed, and averaged. Absorption spectra in the region between 1690 and 1600 cm^{-1}, at a resolution of one data point every 0.25 cm^{-1}, are obtained using a clean crystal as background. 100μg of peptide in HFIP, dried under nitrogen flux and then resuspended in 10 mM Hepes, pH 7.4, are deposited and gently dried again under nitrogen in a thin layer on one side of the crystal.
All measured spectra are plotted in Fig. 3.3. In the absence of metals, the

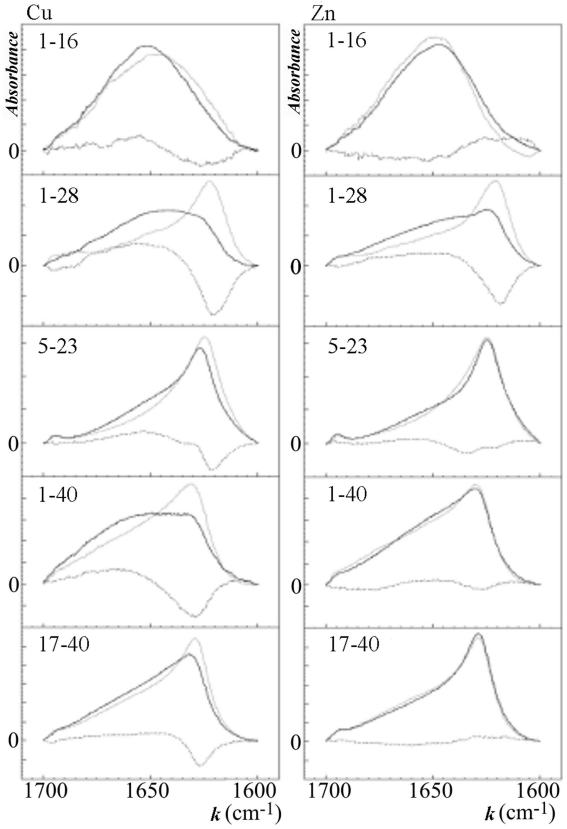

Figure 3.3: FTIR spectra of various Aβ fragments, both in the absence (gray lines) and in the presence (black lines) of Cu (left panels) or Zn (right panels) ions.

FTIR spectra collected at the amide I'band of $A\beta$(1-28), $A\beta$(5-23), $A\beta$(1-40)

and $A\beta$(17-40) show a peak at a wavenumber (k$\simeq$ 1630 cm^{-1}) typical of a β-sheet secondary structure, whereas for the $A\beta$(1-16) sample the peak is located at a wavenumber (k$\simeq$ 1654 cm^{-1}) typical of an α-helix structure.
In the presence of Cu ions, a conformational change from β-sheet to α-helix is observed in the cases of Aβ(1-40) and Aβ(1-28), while the secondary structure of Aβ(5-23) and Aβ(17-40) samples does not change. The fragment Aβ(1-16) is already in an α-helix and, as expected, Cu does not affect its secondary structure. It is interesting to note that, despite their strong ability of promoting aggregation, Zn ions have almost no influence (with perhaps the exception of a small effect in the case of the Aβ(1-28) fragment) on peptide conformation.

3.1.4 Sample Preparation and Data Collection

Aliquots of all Aβ peptides fragments are dissolved in a 10 mM N-ethylmorpholine (NEMO) buffer, that has been proven not to interfere with metal binding [26]. Final 0.5-1 mM peptide concentrations at pH$\approx$7 are obtained. Cu and Zn are added by dissolving the necessary amount of the corresponding salts, $CuSO_2$ and $ZnCl_2$, directly in the peptide solution. Metal ions are always added in sub-stoichiometric concentrations in order to limit the presence of free metal ions in solution, which would give spurious contributions to the XAS signal.
25 μl of the solutions prepared as described above are directly transferred in a 1 mm thick plastic holder closed by two Kapton windows, as shown in the left panel of 3.4, and rapidly frozen in liquid nitrogen. Spectra have been acquired at the D2 bending magnet beamline of the EMBL c/o DESY Hamburg (see Fig. 3.4, right panel). The samples have been kept at 20K throughout the whole measurement session in order to limit possible radiation damage. The synchrotron was operating at 4.5 GeV with ring currents ranging from 90 to 150 mA. A Si(111) double-crystal monochromator has been used to scan X-ray energies around Cu and Zn K-edge. Harmonic rejection was achieved by a focusing mirror (cut-off energy at 20.5 keV) and a monochromator detuning to 50% of its peak intensity. Fluorescence signal was recorded by a 13 elements Ge solid state detector (Industries Inc., Meriden, CT, USA).
In each run several (from 16 to 27) spectra are collected and averaged. After

Figure 3.4: Left Panel: Sample holder closed by glued Kapton windows. Right Panel: The EMBL D2 beamline experimental hutch.

background subtraction, the resulting spectrum is normalized, and the EXAFS signal, i.e. the χ(k), is extracted using the Kemp software [112]. The normalization and χ(k) extraction procedures used are those described in paragraph 2.3.1.

3.1.5 XAS Data Analysis

Qualitative Comparisons

Before performing a quantitative EXAFS analysis on the acquired spectra, it is worth comparing them to extract qualitative information. The 10 spectra (five fragments in complex with either Cu or Zn) reveal indeed interesting patterns of similarities and differences that are summarized below, where the equal sign indicates that they show identical spectral features in the region under consideration, while the similar sign is used when they are slightly different.
For what concerns the XANES region (see Fig. 3.5), by looking separately at Cu and Zn spectra one can notice that
Cu samples (Fig. 3.5, upper panel)
Cu-Aβ(1-16) = Cu-Aβ(1-28) = Cu-Aβ(1-40) $\simeq$ Cu-Aβ(5-23) $\simeq$ Cu-Aβ(17-40)
Zn samples (Fig. 3.5, lower panel)
Zn-Aβ(1-16)=Zn-Aβ(1-28)$\neq$Zn-Aβ(1-40)$\neq$Zn-Aβ(5-23)$\neq$Zn-Aβ(17-40)
When the same qualitative comparison is done in the EXAFS region (see Fig. 3.6)

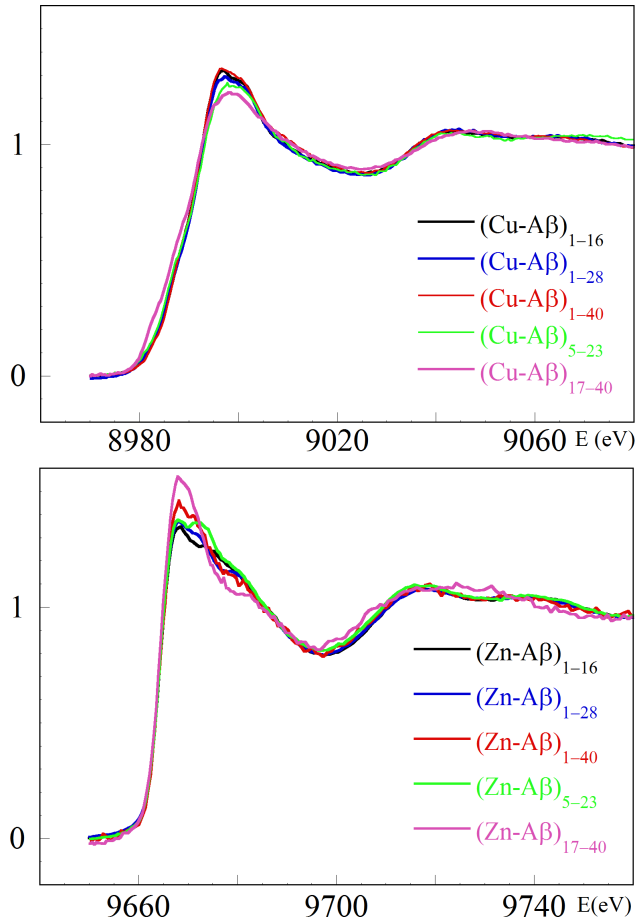

Figure 3.5: Comparison of the five spectra in the XANES region at the Cu K-edge (upper panel) and Zn K-edge (lower panel).

one can see that:

Cu samples (Fig. 3.6, upper panel)

Cu-Aβ(1-16)=Cu-Aβ(1-28)=Cu-Aβ(1-40)$\neq$Cu-Aβ(5-23)$\neq$Cu-Aβ(17-40)

Zn samples (Fig. 3.6, lower panel)

Zn-Aβ(1-16)=Zn-Aβ(1-28)=Zn-Aβ(1-40)=Zn-Aβ(5-23)$\neq$Zn-Aβ(17-40)

Furthermore, spectra of Cu-Aβ(17-40) and Zn-Aβ(17-40) are respectively identical to those of Cu and Zn in buffer in the absence of the peptide (Fig. 3.7). This last observation confirms that Aβ(17-40) is not able to bind Cu nor Zn ions, hypothesis that also justifies the absence of conformational changes revealed by FTIR measurements.

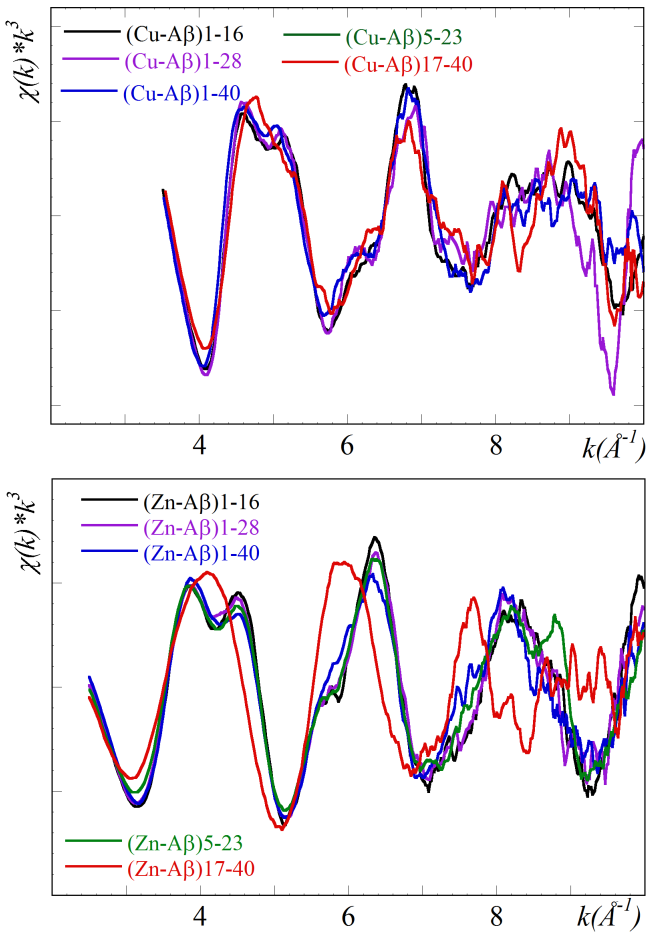

Figure 3.6: Comparison of the five spectra in the EXAFS region at the Cu K-edge (upper panel) and Zn K-edge (lower panel).

A few interesting observations can be made from the previous qualitative analysis.

The observation that all the fragments in complex with Zn, with the only exception of Aβ(17-40), show identical EXAFS features indicates that the local environment around Zn ions is the same in all of them. This finding confirms that the metal binding site is comprised in the first 16 aminoacids and that the first 4 residues do not play any role in Zn binding.

The only notable difference between Zn and Cu at this qualitative level is that in the latter case not only Cu-Aβ(17-40) is different from the remaining ones, but also Cu-Aβ(5-23).

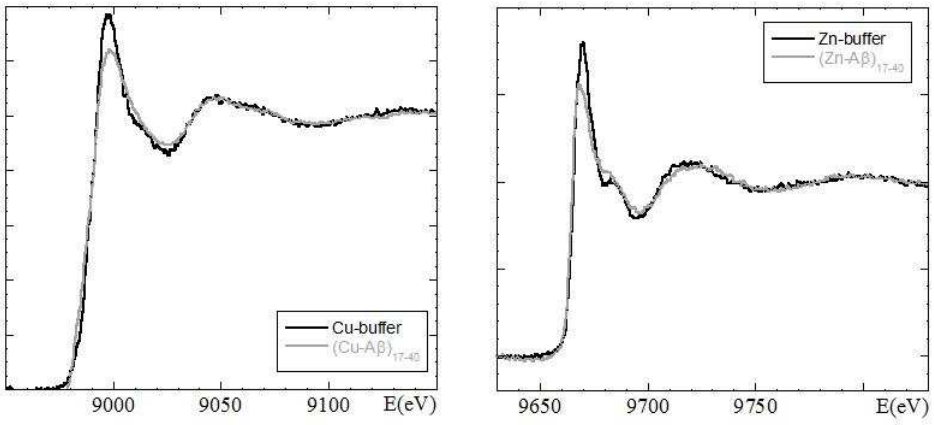

Figure 3.7: XANES region of the Cu-Aβ(17-40) (left panel) and Zn-Aβ(17-40) (right panel) complexes superimposed to the correspondent metals dissolved in buffer.

The finding that Cu-Aβ(1-16), Cu-Aβ(1-28) and Cu-Aβ(1-40) show identical spectral features indicates that the metal binding site is comprised in the first 16 residues. However the difference observed in the Cu-Aβ(5-23) spectrum is suggestive of a role played by the N-terminal region in the Cu coordination.
A last observation is about the differences among the various XANES spectra. In Zn containing complexes, there are significative differences in the shape of the main peak. In particular, the symmetry around the maximum is progressively lost when going from the Zn-Aβ(1-40) sample to Zn-Aβ(5-23), passing through Zn-Aβ(1-16). The loss of peak symmetry is known to be associated to a decreased geometrical symmetry of the metal-binding site [118][119]. Taking into account that these spectra are essentially identical in the EXAFS region, the XANES spectral differences should be due to small geometrical dissimilarities in the atomic arrangement around the metal and not to differences in the number and distances of the amino acidic residues primarily bound to the absorber.
For what concerns Cu containing complexes (upper panel of Fig. 3.5), there are much less pronounced differences in the shape of the main peak, thus possibly indicating a lower flexibility of the Cu binding region.

Quantitative Analysis

A quantitative analysis of the XANES region in general requires a very well established knowledge of the geometry around the absorber. In our case, due to the lack of this knowledge, the only quantitative analysis can be performed in the EXAFS region.
The EXAFS data have been analyzed and fitted employing the EXCURV98 package [99]. The theoretical absorption coefficient is calculated by taking into account single and multiple scattering contributions. Because of the lack of X-ray diffraction data on the systems subject of our analysis, reasonable starting models have been selected among the protein structures collected in the Protein Data Bank [113], with a particular attention to the metal binding sites specifically collected in the Metalloprotein Database and Browser (MDB) [114].
Following the so-called restrained refinement procedure described by Binsted *et al.* [115], we have chosen to treat as a rigid body the internal geometry of the Histidine imidazole ring as well as that of the Tyrosine phenyl ring. The remaining degrees of freedom of the Histidine and Tyrosine metal bound residues are the distance between the bound nitrogen of the imidazole ring and the metal and the distance between the bound oxygen of the Tyrosine hydroxyl group and the metal, respectively.
Taking into account the observations of the previous comparative analysis, EXAFS quantitative analysis is limited to the following spectra:
1- Cu-Aβ(1-16) is analyzed as the prototype of the group containing Cu-Aβ(1-28) and Cu-Aβ(1-40);
2- Cu-Aβ(5-23), that is different from the previous three;
3- Zn-Aβ(1-16) is analyzed as the prototype of the group containing Zn-Aβ(1-28), Zn-Aβ(1-40) and Zn-Aβ(5-23) spectra.
Cu-Aβ(17-40) and Cu-Aβ(17-40) are not analyzed because they show spectra that are identical to the corresponding metals in buffer.
In order to compensate for the amplitude decrease, both the experimental and the fitted χ(k) spectra are multiplied by a factor k^3. For each fit, a two-panels plot is drawn. In the left panel, the theoretical signal (in black) is superimposed to the experimental one (in gray). In the right panel, the modulus of the corresponding FT's are shown.

The best fit for Cu-Aβ(1-16) (Fig. 3.8) is obtained using a geometrical model in which, besides three histidine residues and one tyrosine, an oxygen atom possibly belonging to a water molecule or to an amino acid other than His or Tyr is also included.

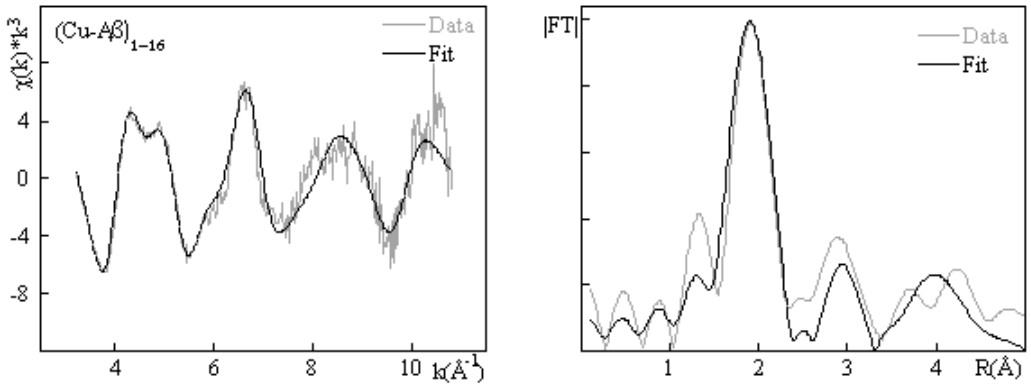

Figure 3.8: Best fit and corresponding FT of Cu-Aβ(1-16).

As already explained in section 2.3.3, there is an EXAFS feature associated with His residues that is easily recognizable, therefore their presence can be almost unambiguously detected. This is not the case for the other aminoacids. In the present case, however, the presence of a Try residues has been proposed in the literature [29][36] and it is confirmed by our FTIR spectra. There is in fact a peak in FTIR spectra, located at 1515cm^{-1}, which is characteristic of the C-OH group of the Tyr phenyl ring. As shown in Fig. 3.9 this C-OH peak is present in the Aβ(1-16) fragment in the absence of Cu ions, while it disappears when Cu concentration is increased from 0 to twice Aβ concentration. In contrast, Zn ions do not affect the intensity of this peak, thus suggesting that Tyr is involved in Cu, but not in Zn binding.
We should signal, however, that a model in which the Tyr oxygen is replaced by the nitrogen of the N terminus gives rise to a fit only marginally worse than the one proposed here. As a consequence the possibility of a Cu coordination with the N-terminal nitrogen cannot be rejected only on the basis of these XAS data.

The best-fit geometry obtained for Cu-Aβ(1-16) has been used as a starting model for Cu-Aβ(5-23), but we could't obtain a satisfactory fit. Taking into

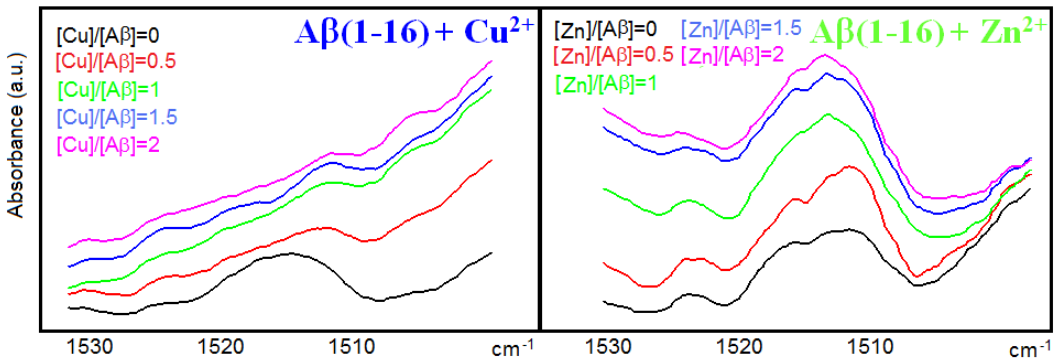

Figure 3.9: FTIR spectra of Aβ(1-16) in the absence of metal ions and in the presence of Cu (left panel) or Zn (right panel) ions.

account the structure proposed in [35], where Cu is bound to two His residues, two oxygen atoms and the N-terminal group, a starting model has been built. With this model we succeeded in obtaining a good fit (Fig. 3.10). The fact that, by cutting out the first four amino acids, the number of coordinated histidines passes from three to two, is a strong indication that His6 is the third residue normally bound to the metal. Considering its position in the aminoacidic sequence, His6 is indeed the one which is most likely affected by the removal of the first 4 residues. We then made the reasonable hypothesis that His6 would be substituted by the N-terminus in Cu binding of Aβ(5-23). Furthermore, in analogy with the Cu-Aβ(1-16) model, one of the oxygen atoms can be possibly attributed to the tyrosine, while the other one reasonably belongs to a water molecule.

For the reasons explained above, in the case of Zn complexes the analysis has been limited to the spectrum of Zn-Aβ(1-16). Again, various starting configurations with different number of His residues bound to the metal have been used. None of the models used for Cu complexes has lead to a satisfactory fit.

The best fit to the data, shown in Fig. 3.11, is instead obtained by including four His residues and one oxygen atom in the Zn coordination sphere. Taking into account FTIR data (see Fig. 3.9), this oxygen atom is not attributable to the Tyr residue. The structure proposed here is of particular relevance because, recalling that each Aβ peptide only contains three histidine residues, it means that at least two different peptides are involved in the Zn binding.

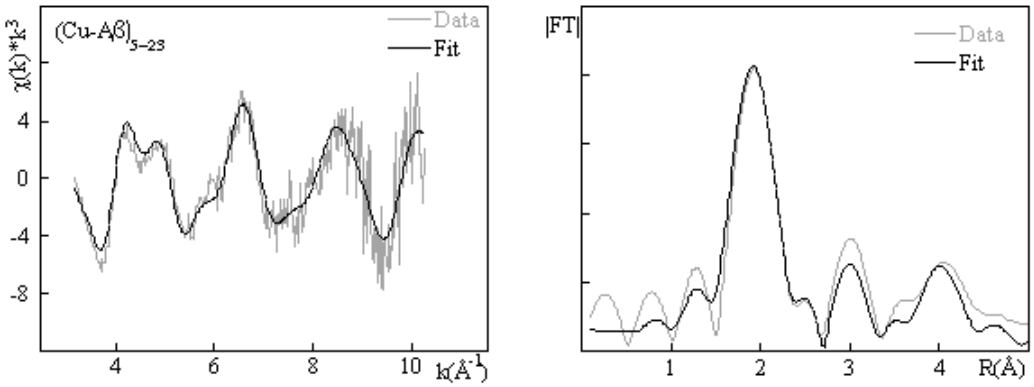

Figure 3.10: Best fit and corresponding FT of Cu-Aβ(5-23).

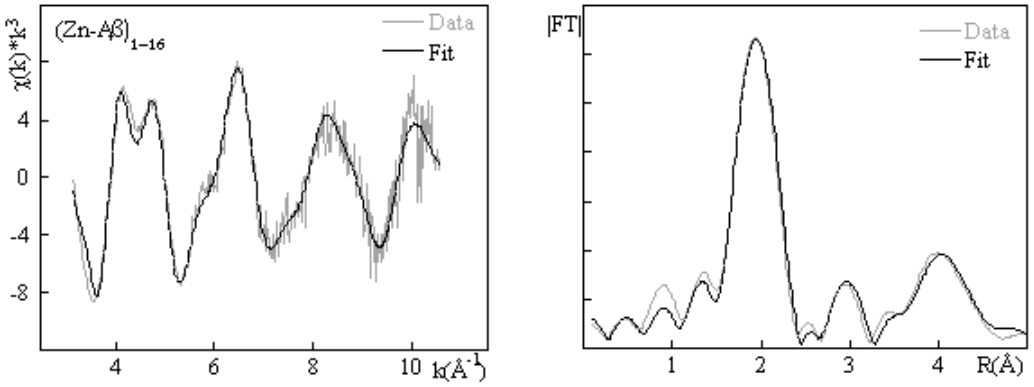

Figure 3.11: Best fit and corresponding FT of Zn-A$\beta(1-16)$.

In Table 3.1 the best fit parameters characterizing the atomic arrangement around the absorber of the three analyzed samples, namely the number, N, of coordinated chemical groups (atom or residue), the distance, r, from the absorber of the coordinated atom (or of the leading atom of the coordinated residue) and the corresponding Debye-Waller (DW) factors, are reported. For each sample the Fermi energy shift, ΔE_F, and the quality factor, R, of the fit are also reported. In order to limit the number of refined parameters, some of the distances (marked with an asterisk) have been constrained to vary together. Furthermore, the DW factors of the same coordination shell have also been constrained to vary together.

A sketch of the three-dimensional geometries corresponding to the best fit struc-

Residue	**N**	**r**$\pm\delta$**r** (Å)	**DW**$\pm\delta$**DW**(Å^2)
	Sample	**Cu-Aβ(1-16)**	
His	3	1.95* ± 0.01	0.002 ± 0.001
Tyr	1	2.06 ± 0.01	0.002 ± 0.001
O	1	1.95* ± 0.01	0.002 ± 0.001
		ΔE_F=(-10.6 ± 0.7) eV	R= 28%
	Sample	**Cu-Aβ(5-23)**	
His	2	1.99* ± 0.01	0.003 ± 0.001
Tyr	1	1.99* ± 0.01	0.003 ± 0.001
N-ter	1	1.99* ± 0.01	0.003 ± 0.001
O	1	2.27 ± 0.01	0.003 ± 0.001
		ΔE_F=(-13.8 ± 0.4) eV	R= 40%
	Sample	**Zn-Aβ(1-16)**	
His	2	1.96 ± 0.01	0.003 ± 0.001
His	2	2.00* ± 0.01	0.003 ± 0.001
O	1	2.00* ± 0.01	0.003 ± 0.001
		ΔE_F=(-6.5 ± 0.2) eV	R= 23%

Table 3.1: Metal-Aβ complexes best fit parameters. Distance marked with an asterisk have been constrained to the same values during the fitting procedure. The statistical errors are written next to each parameter.

tures is given in Fig. 3.12. In this Figure the structure of the amino acidic residues directly involved in the metal binding are taken from the pdb produced by the Excurve program, while the green ribbon is just to suggest the mode in which the peptides are supposed to fold around the metal binding site.

3.1.6 Discussion and Conclusions

Our XAS measurements performed on various length fragments of the Aβ(1-40) peptide in complex with either Cu or Zn have been collected with the aim of determining the precise location and structure of the metal-binding site. The conclusions presented here below come out from the combined analysis of XAS,

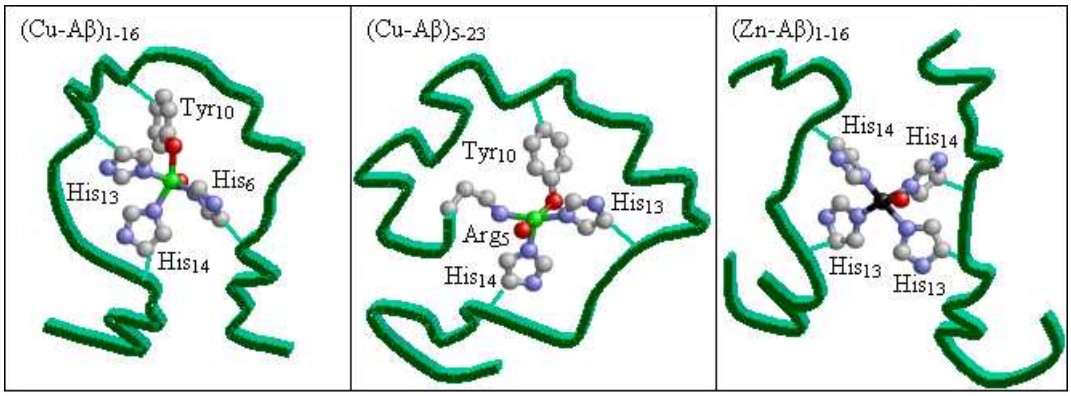

Figure 3.12: Sketches of best fit models. The ball and stick part is obtained from the PDB files directly produced by EXCURVE. The green ribbon is just a cartoon of peptide folding.

OD and FTIR measurements.

OD and FTIR measurements have shown that the effect of Cu and Zn ions on Aβ aggregation propensity and secondary structure are different.

Furthermore, XANES spectra have suggested that the local environment around Cu ions is rather stable, while Zn endows a larger flexibility to the complexes.

EXAFS spectra are compatible with Cu-Aβ(1-16) bound to three histidines (His6, His13, and His14) and two oxygen atoms. This geometry is consistent with an intra-peptide coordination mode with the metal bound to residues all belonging to the same peptide molecule. The last conclusion is strengthened by FTIR results, because the observed variation of Aβ secondary structure is suggestive of an intra-peptide binding mode.

The intra-peptide binding geometry gives rise to a rather rigid and stable coordination mode, which is well preserved in the three fragments Aβ(1-16), Aβ(1-28) and Aβ(1-40). This intra-peptide coordination mode seems to be stable also in the presence of slight variations in the experimental conditions. In fact the geometrical model we obtained here is substantially the same we obtained in a previous work [116] for the Aβ(1-40) in complex with Cu dissolved in TRIS buffer.

The study of Aβ(5-23) behavior allows to draw interesting conclusions on the role played by residues in the N-terminal region of the peptide. The XAS fits suggest

indeed to attribute the difference of its EXAFS spectrum compared with that of all the other Cu complexes to the absence of one Cu-His coordination, which seems to be substituted by the N-terminus. This indicates that the N-terminus has a role, which can be either direct or indirect, in Cu binding.
For what concerns the Zn complexes analysis, in agreement with models suggested by other groups (see in particular [28]), our results are compatible with the presence of a kind of Aβ peptides network where the Zn stabilizes the structure making a bridge between histidines (see [117]) belonging to adjacent peptides. This structural arrangement is possibly allowed by the more pronounced propensity of Zn to form flexible and open coordination geometries.
Our interpretation of XAS fits results is supported by complementary sedimentation and FTIR measurements, which show that differences in metal coordination are correlated with the different abilities of Zn and Cu to promote aggregation and secondary structure switching. Interestingly, Zn is always more effective than Cu in promoting aggregation, while it has smaller (or no) effect on the peptide secondary structure.
Also by taking into account previous results present in the literature, it is worth noting that Zn binding appears to be more sensitive to experimental conditions. In particular, in our previous XAS study [116] we noticed that the coordination geometry was different depending on the different sample preparation procedures (namely, in solution or in a re-dissolved pellet). Furthermore the spectrum of Zn-Aβ(1-40) dissolved in TRIS buffer resulted to be different from the spectrum presented here, where instead NEMO buffer is used.
All the structural observations reported above are consistent with data already present in the literature, but in addition our study gives a strong indication towards the hypothesis that inter-molecular complexes formation is promoted by Zn ions.
Our model confirms that Cu is bound to Aβ in monomeric complexes, which are reported not to be neurotoxic [11]. It is generally accepted that the real neurotoxic species are the aggregated or oligomeric forms of Aβ (not the fibrils found in senile plaques), and experimental evidences suggest that a dimeric structure, similar to the one proposed here in the presence of Zn, may be the precursor to more extensive pathologic aggregation [13].

Some preliminary medical tests aimed at identifying *in vivo* the effect on metal ions concentration in AD evolution have been performed by the CNR Trento group on 30 AD patients (unpublished data). The cognitive decline associated to the disease has been monitored every 6 months for two years by the MMSE (Mini Mental State Examination) cognitive screening. In almost all the patients a decrease in the MMSE index has been observed, indicating the loss of mental capabilities and thus the progression of AD. The slope of MMSE change with time was taken as an index of disease worsening. Looking at Fig. 3.13, where the MMSE (negative) slope of each patient is plotted versus the Zn or Cu concentration, the authors observe that there is a (weak) correlation with the concentration of Zn in the blood. On the contrary, the Cu concentration is weakly anti-correlated with MMSE. No correlation is found instead neither with different metals (e.g. Fe and Al) concentration or with other potentially relevant parameters, like free radicals and total antioxidant status, measured in the blood of the patients. This indication is in good agreement with our experimental evidences that claim a different kind of interaction between Aβ peptides and Cu or Zn.

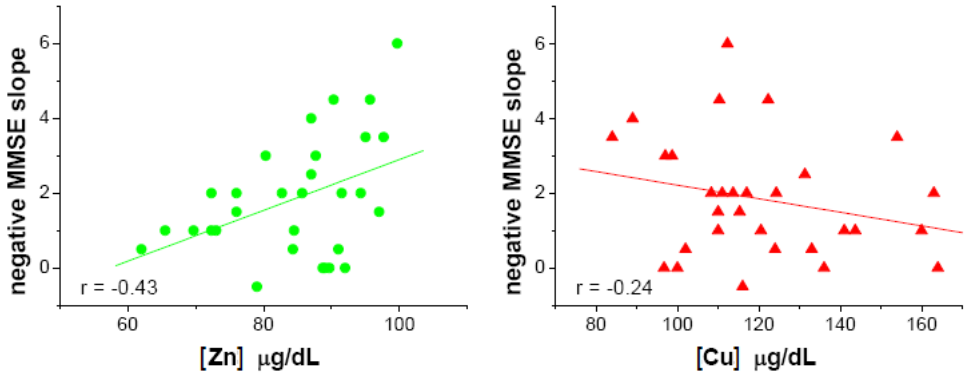

Figure 3.13: Correlation between the rate of cognitive decline (MMSE negative slope) and the average concentration of Zn (left panel) and Cu (right panel) in the blood from a set of 30 patients monitored for two years.

Of course, a lot of efforts are still needed in order to obtain a more detailed comprehension on Aβ peptides behavior in the presence of metal ions. A suitable tool for these studies are the *ab initio* simulations. In our group we have

started a long-term project in which Car-Parrinello (CP) type simulations [120] are used. CP has been largely and very successfully used in many research areas ranging from solid-state physics to biological systems. An obvious limitation to the use of CP simulations is the foreseeable very short length of the trajectory (few picoseconds for systems of the size one is interested in this kind of studies). In any case already a few picosecond trajectory can give useful information on structural problems like those we face here (i.e. identification of primary metal ligands). Obviously, adequate long and accurate numerical investigations are necessary in order to have a general overview on this challenging problem, but, thanks to the foreseeable forthcoming scaling up of the available CPU times by some 10^3 factor, one can hope to be soon able to simulate systems of biological interest of realistic size and for physical times of the order of the nanosecond.

3.2 Cu and Zn PrP complexes

In this section I am going to describe XAS experiments performed on the PrP octarepeat subdomain in the presence of Cu and Zn ions.
This work is performed in collaboration with the group lead by Prof.Glenn Millhauser in the University of California Santa Cruz, that has been responsible for sample characterization and EPR measurements (in particular Ann Spevacek has been directly responsible for sample manipulation during the beamtime), and with Olivier Proux, who contributed in XAS data acquisition and analysis.
In a previous work from our group [102] XAS spectroscopy has been used to explore the Cu site geometry in PrP peptides containing one, two and four-octarepeats and the whole recombinant form of bovine PrP. In the paper a model in which the Cu coordination mode depends on the [Cu]:[octarepeat] concentration has been proposed. The model has been found to be in nice agreement with the EPR results from [121] showing that Cu can be found in three different coordination modes thus indicating the presence of three types of "components" whose relative fraction depends on the [Cu]:[octarepeat] concentration ratio.
More recently, EPR measurements carried out by the same group [55] have shown that the presence of Zn modulates the Cu binding mode to the synthetic PrP tetra-octarepeat peptide. In particular it has been suggested that, even if Zn is not able to displace Cu, increased Zn concentration can progressively change the way Cu is bound to the tetra-octarepeat. At the same time, it is observed that the Cu titration curve is different according to whether Zn is present or not.
In the work discussed here the possibility offered by XAS spectroscopy of looking at the structure around the two metal ions while they are simultaneously present in the same sample is exploited.

3.2.1 EPR Results

As mentioned above, EPR results suggest three Cu coordination modes characterized by the following three atomic environments
1. Component 1 (C1): 3N1O (1N from His + 2N from Gly + 1O)
2. Component 2 (C2): 3N2O (3N from His + 2O). Two N are in the same plane as the two O, while the third N is axial.

3. Component 3 (C3): 3N1O / 4N (all N atoms are supposed to belong to His imidazole rings).

In Fig. 3.14 the dependence of the various component fractions as a function of the total Cu bound concentration (x and y axis are both in equivalents, where 1 equivalent corresponds by definition to the PrP concentration) is shown. In the figure the behavior of a fourth component, C1_w, is drawn. This component corresponds to a fraction of the C1 component where two Cu ions are found rather near (i.e. at a distance between 3.5 and 6 Å), thus causing a broadening of the EPR spectrum.

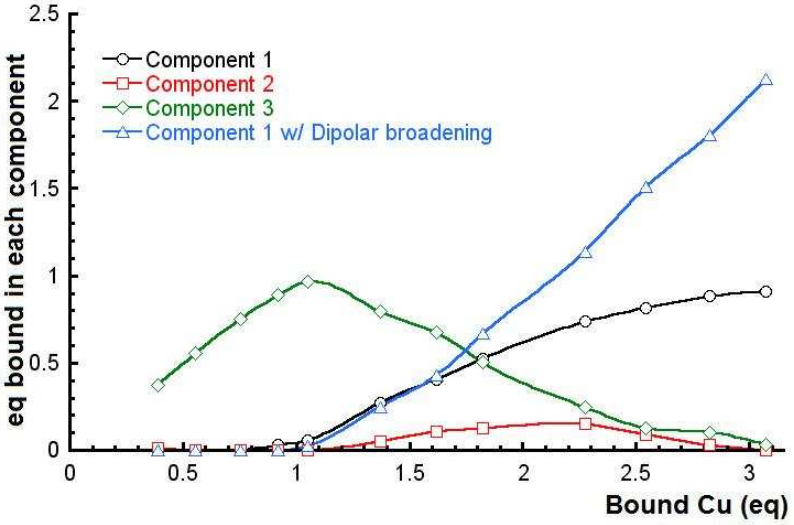

Figure 3.14: Cu coordination modes versus Cu equivalents.

In Fig. 3.15 the effect of the Zn presence is illustrated. Component fractions are plotted as functions of the total Cu bound. Components C1, C1_w and C2 of Fig. 3.14 are grouped together (red line), while component 3 (green line) is separately plotted in the absence of Zn (full line) and in the presence of 300 μM of Zn.

Fig. 3.15 clearly shows that the Cu coordination mode is indeed modified by the Zn presence. In particular it is seen that the effect of Zn ions is stronger at low Cu concentration and tends to disappear at high Cu concentration. Furthermore, at low Cu concentrations, the presence of Zn induces an increase of the components C1 and C2, thus pushing the system towards coordination modes

where the number of His's bound to Cu is lower.

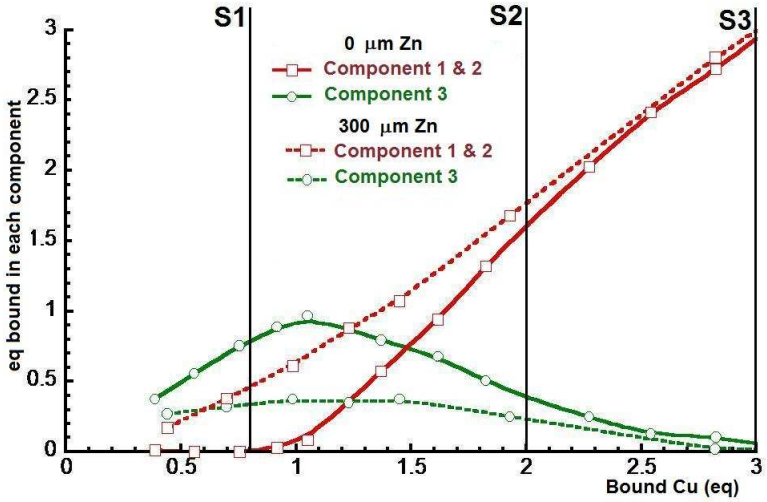

Figure 3.15: Cu coordination modes in the absence (full lines) and in the presence (dotted lines) of Zn versus Cu equivalents. Components C1, C1_w and C2 are grouped together (red lines), while component 3 (green line) is separately plotted. Three vertical lines are drawn to underline the Cu concentration of XAS measured samples (see Table 3.2).

It is important to note that Zn is EPR silent, thus EPR measurements do not allow to know how Zn affects Cu binding, namely by directly displacing Cu or by inducing an indirect structural modification. XAS instead can tell us whether and how Zn binds to PrP or not. We then acquired XAS spectra of samples with different Cu concentrations both in the absence and in the presence of Zn, recording spectra at both Cu and Zn K-edges.

3.2.2 XAS Data Analysis

Sample Preparation and XAS data acquisition

Starting from a 0.2 mM tetra-octarepeat solution, three samples containing Cu at 0.16 mM, 0.4 mM and 0.6 mM concentrations, corresponding to 0.8, 2 and 3 equivalents, respectively (see Figs. 3.14 and 3.15), have been prepared. Each sample is further subdivided into two sub-samples, and in one of them 0.6 mM Zn is added. Furthermore two buffer solutions, where 2.0 mM of Cu and Zn,

respectively, are dissolved, have also been prepared. The list of the samples subjected to XAS measurements is given in Table 3.2.

Sample	[Cu]mM	[Zn]mM	[His]mM	Cu (eq)	Edge
S1	0.16	0.0	0.8	0.8	Cu
S2	0.4	0.0	0.8	2	Cu
S3	0.6	0.0	0.8	3	Cu
S1_Zn	0.16	0.6	0.8	0.8	Cu, Zn
S2_Zn	0.4	0.6	0.8	2	Cu, Zn
S3_Zn	0.6	0.6	0.8	3	Cu, Zn
B_Cu	2.0	0.0	0.0	-	Cu
B_Zn	0.0	2.0	0.0	-	Zn

Table 3.2: PrP samples subjected to XAS measurements.

In the first column of Table 3.2 the samples subjected to XAS measurements are reported. The first three samples, S1, S2 and S3, do not contain Zn, while the following three, S1_Zn, S2_Zn and S3_Zn are the corresponding samples in the presence of Zn. In the last two rows the reference samples (buffers) are reported. In the following four columns Cu, Zn and His concentration, and Cu bound equivalents (as in Fig. 3.14 and Fig. 3.15) are given. In the last column the metal edge at which the spectrum has been collected is given.
Experiments are performed at the Cu and Zn K-edges on the BM30b beamline of the European Synchrotron Radiation Facility (Grenoble, France) [122]. The storage ring was operated in 16 bunches mode at 6 GeV with a ∼90 mA current. The beam energy was selected using a Si(220) double-crystal monochromator with an experimental resolution close to the theoretically predicted one (namely 0.5 eV) [123]. The beam size on the sample was approximately 300 x 200 μm (H x V). Due to the low concentration of Cu and Zn, spectra were recorded in fluorescence mode using a 30-element solid state Ge detector. Finally, to avoid photodegradation and spectra evolution during XAS measurements, the samples were cooled to -260 °C using a liquid helium cryostat.

Qualitative Analysis

To gain a first understanding of the structural properties of the metal (Zn and Cu) coordination modes, similarities and differences among the measured spectra are examined. A qualitative, but systematic comparison of the XANES and/or EXAFS regions of the spectra is performed considering the following sets of data.
-Cu K-edge data: the spectrum of Cu in buffer (B_Cu) is compared with the spectra of the samples at different Cu concentrations both in the presence (Sn_Zn) and in the absence (Sn) of Zn.
For each Cu concentration the spectra in the presence and in the absence of Zn, i.e. (Sn_Zn) vs. (Sn) for each n, are compared.
-Zn K-edge data: the spectrum of Zn in buffer (B_Zn) is compared with the spectrum of each Zn containing sample at different Cu concentrations (Sn_Zn), as well as the spectra of those among themselves.

In Fig. 3.16 the comparison of the spectrum of Cu in buffer with those of samples at different Cu concentrations in the absence of Zn is shown. All comparisons in the XANES region are made among normalized spectra. The normalization is standardly performed as described in 2.3.1 by using the software ATHENA [91]. In the XANES region it is quite evident, mainly looking at the shape of the white line, that the spectrum of Cu in buffer is rather different from that of Cu bound to the peptide.
In the EXAFS region, the Cu buffer spectrum is different from that of all the other samples and furthermore S2 and S3 spectra are very similar between themselves, but significantly different from that of S1. This qualitative observation is in agreement with EPR results. In fact, at low Cu concentration (sample S1) only the component C3 is present, the fraction of which decreases with increasing Cu concentration. Indeed, the fraction of component C3 is already very low at 2 Cu eq's (sample S2) and completely disappears at 3 Cu eq's (sample S3), as seen in Fig. 3.15.
It is also interesting to compare the three samples S1, S2 and S3 with (gray lines) and without (black lines) Zn (see Fig. 3.17). Samples S1 and S2 are rather noisy due to the low Cu concentration, but looking at sample S3 is quite evident that the presence of Zn doesn't affect the Cu coordination in the high Cu concentra-

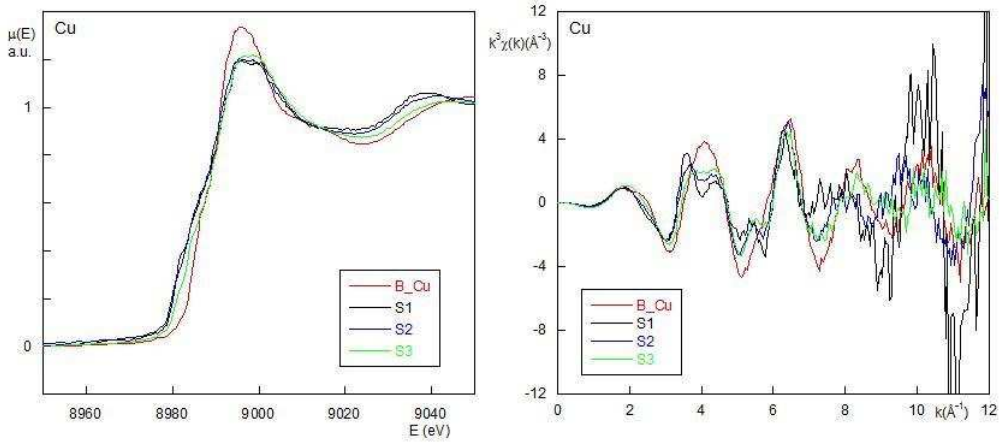

Figure 3.16: Comparison among B_Cu and S1, S2 and S3 in the XANES (left panel) and EXAFS (right panel) regions.

tion region, while the differences are more relevant, as expected, in the low Cu concentration region.

A similar analysis as the one carried out before is performed when the spectra registered at the Zn K-edge at different Cu concentrations (samples Sn_Zn in Table 3.2) are compared with the buffer (B_Zn) spectrum. XANES and EXAFS region comparisons are reported in Fig. 3.18, which shows that the spectrum of S1_Zn is significantly different from that of Zn in buffer, while spectra of the samples where the Cu concentration is higher (S2_Zn and S3_Zn) are almost identical between themselves and very similar to the spectrum of Zn in buffer. In other words, the local Zn environment in the S1_Zn sample is significantly different from that of Zn in solution, thus proving that at least a fraction of Zn is bound to the peptide.

Quantitative Analysis

Cu K-edge spectra

Due to the very low Cu concentration of samples S1 and S2, the only samples in which the signal to noise ratio is sufficiently good to allow a reliable quantitative analysis are S3 and S3_Zn. It should be said, however, that these two are the least interesting samples. In fact, according to EPR data (see Fig. 3.15), the presence of Zn doesn't affect the Cu coordination mode. Indeed, at the Cu

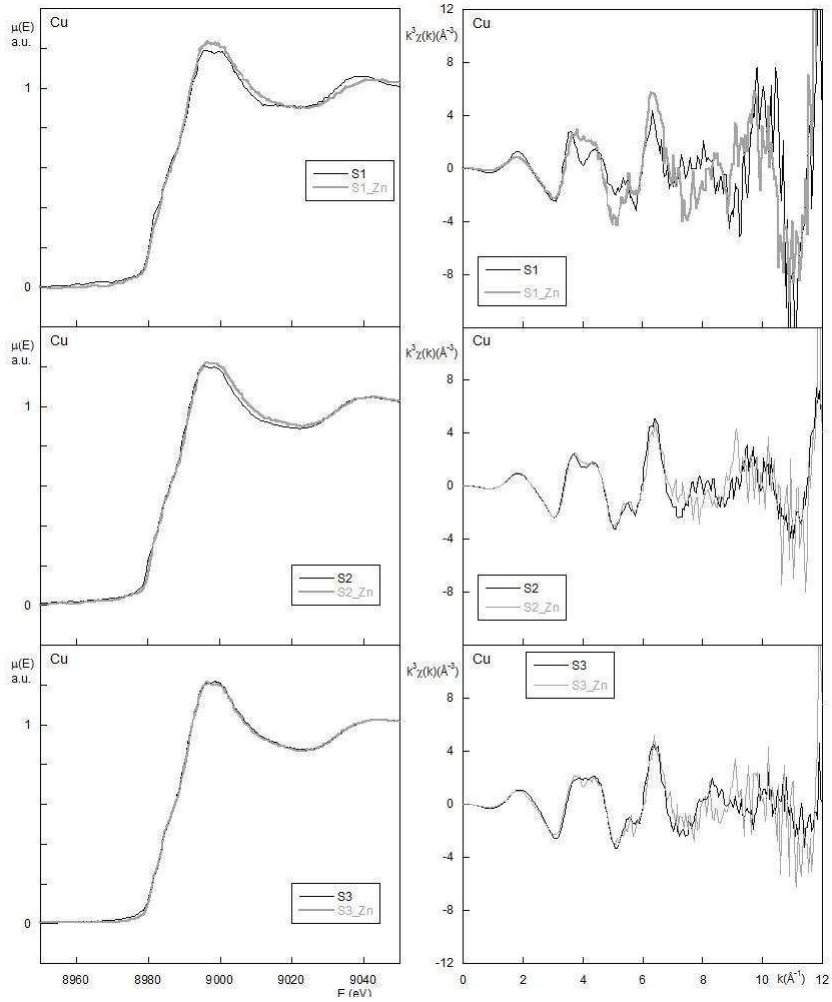

Figure 3.17: Comparison between S1 and S1_Zn, S2 and S2_Zn, S3 and S3_Zn in the XANES (left panels) and EXAFS (right panels) regions.

concentration present in sample S3, EPR data show that only component C1 is present. In C1 the Cu is supposed to have the same coordination mode that has been solved by diffraction data [124], namely it is bound to one Histidine, to two Glycine residues and to a water molecule.

A fit of the XAS spectra of S3 and S3_Zn samples was then performed exploiting the available crystallographic data. It should be noted that the sample S3_Zn displays a lower signal to noise ratio than S3 due to the fact that the number of spectra that have been averaged is lower because, for technical reasons, many of the collected spectra had to be discarded.

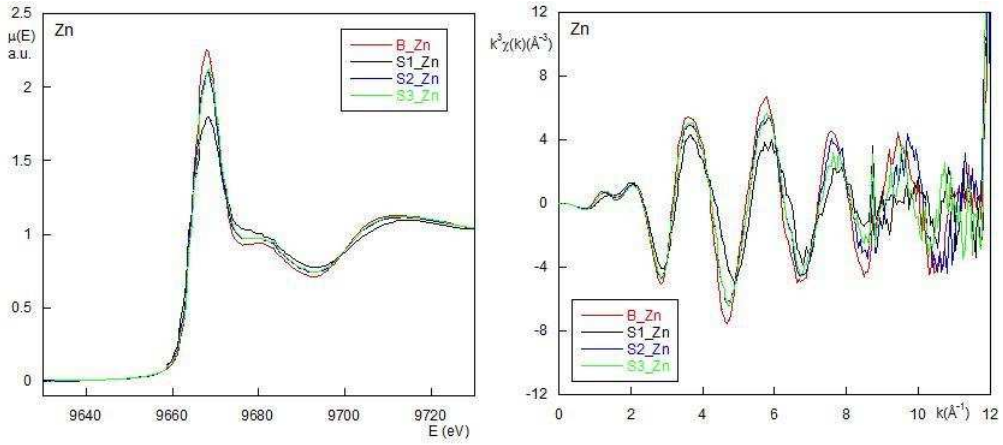

Figure 3.18: Comparison among B_Zn and S1_Zn, S2_Zn and S3_Zn at the Zn K-edge in the XANES (left panel) and EXAFS (right panel) regions.

Figs. 3.19 and 3.20 show experimental (black lines) and best fit (gray lines) spectra. In the right panels the corresponding FT are also plotted. Table 3.3 shows the parameters of the fits compared with structural information coming from the XRD data.
The distances of the three nitrogen atoms on one side and all the σ^2 on the other, are constrained during the fit. Following the restrained refinement procedure [115], the internal geometry of the Histidine imidazole ring is treated as a rigid body.

Atom	**r**(Å)[**XRD**]	**r**±δ**r**(Å)[**S3**]	**DW**±δ**DW**(Å^2)[**S3**]	**r**±δ**r**(Å)[**S3_Zn**]	**DW**±δ**DW**(Å^2)[**S3_Zn**]
N(His)	1.99	1.94 ± 0.01	0.004 ± 0.001	1.93 ± 0.01	0.004 ± 0.001
N(Gly)	2.00	1.94 ± 0.01	0.004 ± 0.001	1.93 ± 0.01	0.004 ± 0.001
N(Gly)	1.92	1.94 ± 0.01	0.004 ± 0.001	1.93 ± 0.01	0.004 ± 0.001
O(Gly)	2.07	2.07 ± 0.02	0.004 ± 0.001	2.07 ± 0.03	0.004 ± 0.001
O(H_2O)	2.38	2.40 ± 0.01	0.004 ± 0.001	2.38 ± 0.01	0.004 ± 0.001

Table 3.3: S3 and S3_Zn best fit parameters. Distance marked with an asterisk have been constrained to the same values during the fitting procedure. The statistical errors are written next to each parameter.

A look at the Table 3.3 shows that structural distances characterizing the Cu atomic environment in S3 and S3_Zn samples are very similar to each other and well consistent with crystallographic data, confirming that, irrespective of Zn

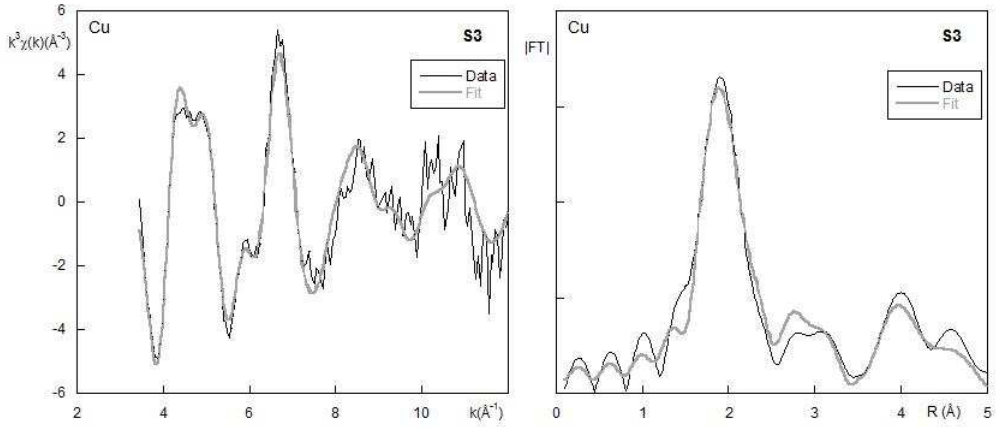

Figure 3.19: S3 sample best fit. Experimental (black lines) and best fit (gray lines) spectra are drawn in left panel. In the right panel the corresponding FT are plotted.

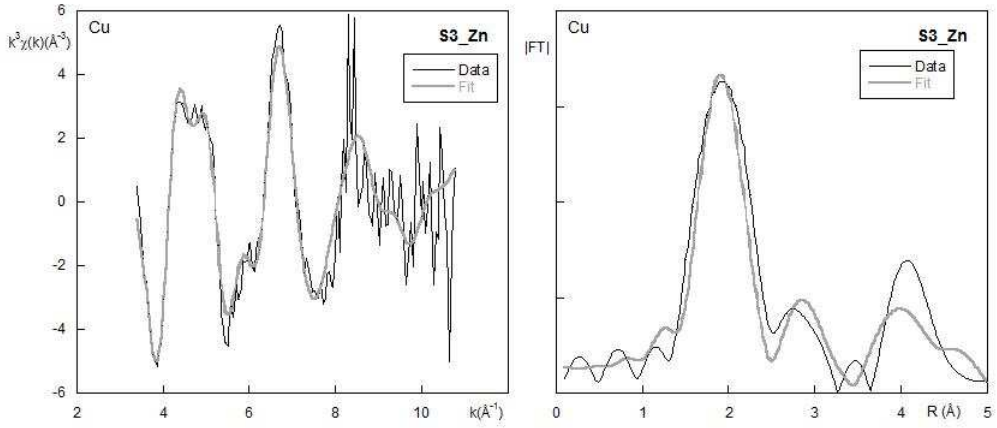

Figure 3.20: S3_Zn sample best fit. Experimental (black lines) and best fit (gray lines) spectra are drawn in left panel. In the right panel the corresponding FT are plotted.

presence, Cu in S3 and S3_Zn sample finds itself in the same geometrical arrangement as in component C1.

Zn K-edge samples

In order to perform the quantitative analysis of Zn spectra, the reasonable assumption that the Zn is present in the samples in two different structural con-

figurations, one corresponding to Zn in solution and a second one corresponding to Zn in complex with the peptide, is made. At this point, since the geometrical information that one can extract from the XAS data is the result of an average of all the signals coming from the occurring structural environments, an estimate of the relative fraction in which these two Zn coordination modes are present is necessary.

At a given His concentration, $[His]_{tot}$, the His fraction available for Zn coordination, $[His]_{av}$, is

$$[His]_{av} = [His]_{tot} - [His]_{Cu}, \tag{3.2}$$

where $[His]_{Cu}$ is the fraction that is already occupied by Cu. On the other hand, the total amount of Zn in the sample, $[Zn]_{tot}$, is distributed between Zn bound to the peptide, $[Zn]_{His}$, and Zn free in solution, $[Zn]_{free}$

$$[Zn]_{tot} = [Zn]_{His} - [Zn]_{free}, \tag{3.3}$$

Was the number of Zn-bound His's known, one would be able to relate $[Zn]_{His}$ to $[His]_{av}$. Lacking this information, in the following four different models (termed M1, M2, M3 and M4 in the discussion below) in which we assume that Zn is coordinated to 1, 2, 3 or 4 His's, will be examined. For simplicity bound Zn will be assumed to be present in the sample in only one of these four coordination modes. Under these simplifying assumptions $[Zn]_{His}$ can be written as

$$[Zn]_{His} = \frac{[His]_{av}}{n}, \tag{3.4}$$

with n is the number of His's supposed to be bound to Zn.

In order to estimate $[His]_{Cu}$ in Eq.(3.2), EPR results are exploited. EPR data show in fact that, in the presence of Zn and at 0.8 equivalents Cu, about 45% of Cu is found in component C3 and the remaining 55% is in component C1 (Fig. 3.15). In other words, all Cu ions are involved in some kind of peptide binding and none of them can be fully substituted by Zn.

This implies that the amount of His bound to Cu can be estimated from the obvious formula

$$[His]_{Cu} = 0.45 \cdot 0.16mM \cdot 4 + 0.55 \cdot 0.16mM \cdot 1 = 0.38mM, \tag{3.5}$$

Then, using Eq.(3.2), one gets

$$[His]_{av} = [His]_{tot} - [His]_{Cu} = (0.8 - 0.38)mM = 0.42mM, \qquad (3.6)$$

In Table 3.4 the concentration of His-bound Zn (column 3) together with the corresponding concentration of free Zn (column 4) for each of the considered models (column 1) are reported.

Model	n His	$[Zn]_{His}$ (in percentage)	$[Zn]_{free}$ (in percentage)
M1	1	0.42 mM (70%)	0.18 mM (30%)
M2	2	0.21 mM (35%)	0.39 mM (65%)
M3	3	0.14 mM (23%)	0.46 mM (77%)
M4	4	0.11 mM (18%)	0.49 mM (82%)

Table 3.4: Concentration of His-bound and free Zn.

Before performing this detailed analysis, the spectrum of sample B_Zn is fitted in order to extract the best structural parameters for the Zn free in solution. The best fit of the EXAFS data shown in Fig. 3.21 is obtained by assuming that Zn is coordinated to 6 oxygen atoms located at a distance of 2.07 Å in an octahedral geometry.

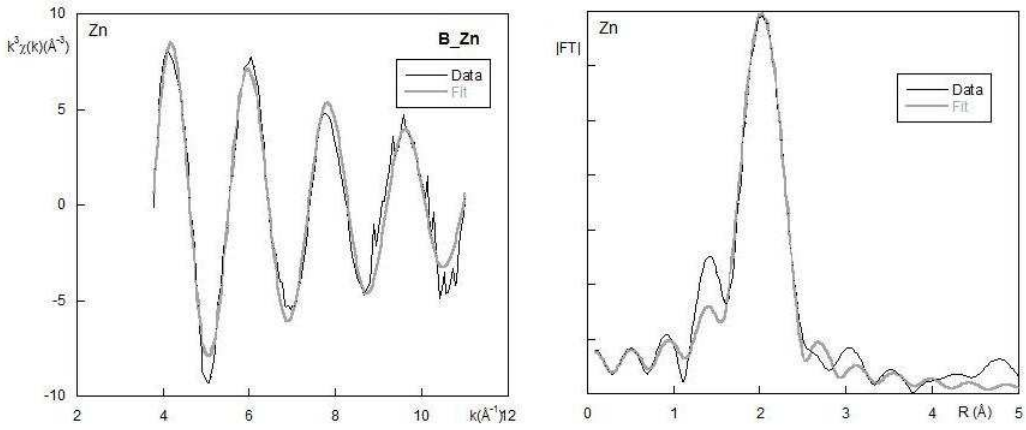

Figure 3.21: B_Zn sample best fit. Experimental (black lines) and best fit (gray lines) spectra are drawn in left panel. In the right panel the corresponding FT are plotted.

As for the S1_Zn EXAFS spectrum four different fits (see Fig. 3.22) have been performed according to the number of His assumed to be bound to Zn. In each case a fraction of Zn remains free in solution. The Zn concentrations used in the fits (computed using Eqs.(3.3) and (3.4)) are those reported in Table 3.4. In all the fits only the distance and relative position of the nearest neighbor atoms in the His-bound Zn environment are taken as free parameters, while Zn free in solution is kept coordinated to six oxygens at a distance of 2.07 Å.
It is rather clear from Fig. 3.22 that, by increasing the number of His residues (from M1 to M4) assumed to be bound to a single Zn ion and correspondingly increasing the percentage of Zn free in solution (see Table 3.4), the quality of the fit significantly decreases.
The quality of the fits can be quantitatively estimated through the quality factor, R. R happens to be unacceptably high for M3 and M4 models, namely 49% and 60% respectively. On the contrary it decreases to acceptable values, 34% and 35%, in the case of M1 and M2.

3.2.3 Discussion and Conclusions

The XAS analysis of the metal-PrP complexes presented here, besides confirming the results of EPR experiments about the Cu coordination modes, provides new insights on the role played by Zn in the Cu coordination mode.
For what concerns the Cu samples, XAS analysis shows that, at high Cu concentration (sample S3), the local environment around the metal ion is the same as in the XRD structure. The fit of sample S3_Zn confirms that this coordination mode is unaffected by the presence of Zn ions. The qualitative comparison among spectra acquired in the absence and in the presence of Zn also shows that samples S1 is significantly different from S2 and S3, as expected according to EPR results. In addition, it is observed that the Cu coordination mode is significantly different in samples S1 and S1_Zn, thus confirming a stronger effect of the Zn presence in the low Cu concentration region.
For what concerns the Zn samples, XAS is used to determine the local environment around the Zn ion, which is instead EPR silent. Both the qualitative and the quantitative analysis show that a fraction of Zn is bound to the peptide.

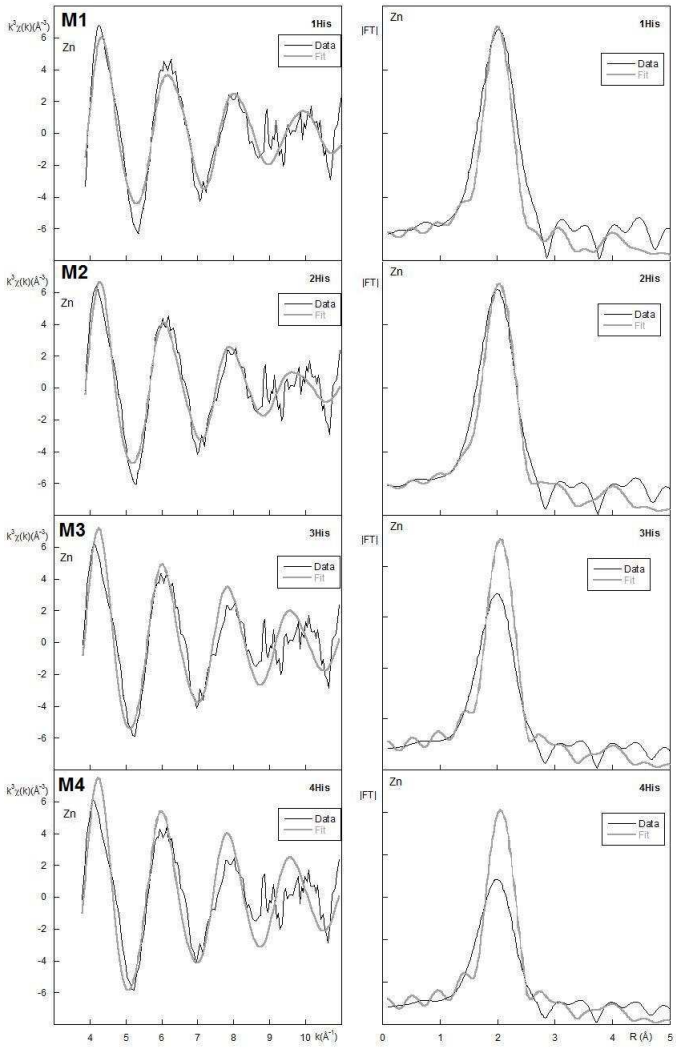

Figure 3.22: S1_Zn sample best fits, corresponding to four different models (M1, M2, M3 and M4) in which Zn is coordinated to 1, 2, 3 or 4 His residues are plotted. Experimental (black lines) and best fit (gray lines) spectra are drawn in left panels. In the right panels the corresponding FT are plotted.

This finding is the answer to a question left open by the EPR measurements, that are not able to establish whether the effect of Zn on Cu coordination mode was indirect or due to a competition for the binding at the same site.
In addition, XAS analysis allowed to solve, even within the crude approximations made in building the considered structural models, the coordination mode of the Zn bound to the peptide. There are indeed sufficient qualitative and quantitative

reasons to discard M3 and M4 models, in which the Zn is bound to 3 or 4 His residues, thus we can conclude that Zn is bound to 1 or 2 His residues, although it is not possible to distinguish between model M1 and M2.

3.3 The S local environment in human Neuromelanin

As described in paragraph 1.5.3, an accurate characterization of the structure of NM is an essential step in understanding its physiological role in ageing and its pathological role in PD. In this section an XAS study [125] aimed at the characterization of the local environment around S in NM is presented.
The work has been done in collaboration with P.R.Crippa from the University of Parma, M.Eisner from Texas University, L.Zecca from CNR-Milan and F.Vicentin, who is the responsible of the beamline at the Brazilian Synchrotron Light Laboratory where XAS data have been collected.

3.3.1 Samples Description

In order to investigate the local structure around S in human NM, samples of three different groups have been prepared and subjected to XAS measurements: natural melanin, synthetic melanins and model compounds. Natural melanin is extracted directly from human brains as described below. Synthetic melanins are prepared using the same class of chemical reactions involved in the biosynthesis of natural melanins. Model compounds have been chosen for their structural similarity with natural melanin. Here below there is the description of the protocols used to prepare the samples.

-Natural Melanins
Natural NM is isolated as described in [67] from the cerebellum of people who died at different ages with no evidence of neurologic or psychiatric disorders. Tissues are collected during autopsies carried out within 48 h after death. The pathological examination performed on normal subjects included in this study did not show neurologic or vascular macroscopic alterations. In particular, a histological examination didn't reveal the presence of Lewy bodies or other pathological markers.
In order to extract the NM, an aliquot of 3.0 g brain tissue is introduced into a 130 ml plastic centrifuge tube, then 90 ml water is added, and the mixture is

shaken. Tubes are centrifuged at 18000 g for 15 min, and the resulting pellet is washed twice with 90 ml phosphate buffer (50 mM, pH 7.4). The sample is then incubated for 3 h at 37°C with 60 ml Tris buffer (50 mM, pH 7.4) containing sodium dodecyl sulfate (5 mg/ml) and L-cysteine (15 mM). The suspension is centrifuged at 18000 g for 20 min and the supernatant is removed, then the resulting pellet is incubated for 3 h at 37°C with 20 ml of the same solution. The NM is separated by centrifugation as above, washed twice with 5 ml NaCl solution (9 mg/ml), and finally washed with 3 ml water. The sample is then suspended in 2 ml methanol, centrifuged, and the supernatant fluid is removed. The sample is finally resuspended in 1 ml hexane, centrifuged, and after eliminating the supernatant fluid, the pigment is dried under nitrogen flow and placed in vacuum for 14 hours.

-Synthetic Melanins

Three synthetic melanins have been prepared, namely DAC, obtained from auto-oxidation of dopamine and cysteine, DEC, obtained from enzymatic oxidation of dopamine and cysteine and DOPEC, prepared by L-DOPA and cysteine enzymatic oxidation.

In order to get the same S content as the NM, DAC is prepared according to the following procedure. Dopamine (1.96 mmol) and cysteine (0.03 mmol) are dissolved in a flask containing 200 ml of 0.05 M sodium phosphate buffer (pH 7.4). The solution, protected from light, is allowed to auto-oxidize in air at 37°C. After 108 h, the suspension is centrifuged (10000 rpm for 10 min), and 200 ml of freshly prepared phosphate buffer containing 0.03 mmol of cysteine is added to the melanin sample obtained in this way. The reaction is continued for another 24 h, and at the end the resulting brown suspension is transferred into centrifuge glass tubes and centrifuged (10000 rpm for 10 min). The precipitated melanin is resuspended in 5 ml of 1% acetic acid, centrifuged, and washed with 5 ml of water. Then, it is let to react twice with 0.15 M Na_2 EDTA and washed with water. The synthetic melanin is dialyzed in order to remove salts and other low molecular weight substances. After the drying procedure described above, the final yield is 30% of the initial amount of dopamine.

DEC is prepared by dissolving an amount of 0.39 mmol of dopamine into a flask

containing 200 ml of 0.05 M sodium phosphate buffer (pH 7.4), together with 61 mg of cysteine and 7 mg of tyrosinase (EC 1.14.18.1, Sigma, St. Louis, MO, USA). The solution is left to react at 37°C for 90 hours. Then the reaction is stopped by decreasing the pH to 3.0 with 30% acetic acid. The suspension is transferred into glass tubes and centrifuged (10000 rpm for 10 min) at 25°C. The precipitate of melanin is resuspended in 7 ml of 0.05 M Tris buffer (pH 7.4) containing 5 mg/ml of sodium dodecylsulfate and allowed to incubate at 37°C for 2 h. Then it is washed with 10 ml of NaCl (9 mg/ml) and, after centrifugation, the melanin is let to react twice with 20 ml of 0.15 M Na_2 EDTA for 8 h, in order to remove every trace of metals. The suspension is centrifuged, and the precipitate washed with 10 ml water. Finally, it is washed with acetone and dried as described above. The final yield is 47% of the initial amount of dopamine.
In order to prepare DOPEC, the tyrosinase enzyme is added to a stirred solution containing 0.51 mmol of L-DOPA in 100 ml phosphate buffer 0.05 M at pH 7 to catalyze the reaction. After 30 s, 1.0 mmol of L-cysteine dissolved in the same buffer is added, and after 24 hours the solution is made acidic (pH 3.5) by adding HCl. The centrifugation precipitate is washed three times with a pH 3.5 HCl solution and then with acetone. Finally, it is dried as described above.

-Model Compounds

Two model compounds, namely decarboxytrichochrome C and cysteine, have been prepared. These two molecules, whose structures are shown in Fig. 3.23, have been chosen because they represent prototypes of different chemical structures in which S can be found in NM.
Cysteine is indeed found in the peptidic part bound to NM and amounts to about 0.5% [68]. Being the other sulfur-containing aminoacid, namely methionine, not present in the peptidic part, cysteine accounts for all the sulfur atoms present in the peptidic part. The local environment around S in cysteine is moreover significantly different from the one found in the decarboxytrichochrome C. The cysteine S is bound only to light atoms and there are no aromatic rings. Cysteine is bought from SigmaAldrich (purity 98%) and it is used without further purification.
In decarboxytrichochrome C the two S atoms present are inside an aromatic ring.

Decarboxytrichochrome C (purity 96%) is a kind gift by Prof.S.Ito and it has been prepared as described in the work of Ye *et al.* [132]. In Table 3.5 a list of

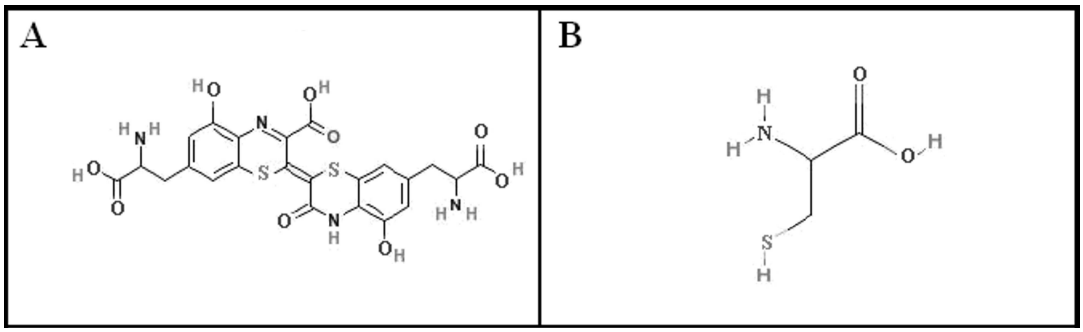

Figure 3.23: Chemical composition of **(A)** decarboxytrichochrome C and **(B)** cysteine residue.

the studied samples is given.

Sample	Features
NM	NM isolated from cerebellum
DEC	Synthetic Melanin
DAC	Synthetic Melanin
DOPEC	Synthetic Melanin
Cysteine	Model Compound
Decarboxytrichochrome C	Model Compound

Table 3.5: List of samples subjected to XAS measurements.

3.3.2 XAS Data Collection

XAS data at the S K-edge have been collected at the D04B bending magnet beam line of the Brazilian Synchrotron Light Laboratory. A Si (111) double crystal monochromator is used throughout the study. X-ray spectra are recorded in total electron yield mode by collecting the sample drain current, I_{TEY}, with an electrometer (Keithley 617). TEY detection method instead of transmission has been chosen because in the S K-edge energy range the Auger electron yield, which provides the main contribution to the total TEY, is higher than the fluorescence

yield. The probability of emission of Auger electrons increases indeed with decreasing atomic number of the absorbing atom [126], as clearly shown in Fig. 2.3. Before hitting the sample, the beam goes through a 0.75 μm sheet of aluminum foil in order to measure the impinging drain current, I_0. It can be shown that in TEY detection, the ratio I_{TEY}/I_0 is to a good approximation proportional to the absorption coefficient [133].

3.3.3 XAS Data Reduction

The analysis of NM XAS data is limited to the XANES region of the spectrum, because for higher energies the recorded signal is essentially flat. This can be due to a number of different phenomena. It is well known that the signal amplitude decreases monotonically with energy in the EXAFS region [127] in a way that depends on the absorber and that is especially fast for light absorbers, such as S [128].

A second possible reason is that the TEY detection method, when used in experiments with insulating specimens as in our case, suffers from charging problems [129]. This feature tends to significantly reduce the intensity of the collected signal at large energies (i.e. in the EXAFS region).

Finally, in our case the local environment around the absorbing atom is most reasonably composed only by light atoms that possibly result in a disordered environment.

In order to be consistently compared and analyzed, XANES data have been reduced according to the following protocol.

First of all, in order to get rid of spurious background contributions affecting the shape of the spectrum, a linear term fitted through the pre-edge region is subtracted from the XAS spectrum.

Secondly, to allow the comparison among different spectra, a normalization procedure is performed, because data have been taken on samples with different, to a large extent unknown, S concentrations. The normalization of data to unit S concentration is in this case a delicate step as the energy range of the available data is very short, thus preventing from employing the standard normalization procedure.

A different method must therefore be derived. After the pre-edge subtraction, the area, A, under the spectrum is computed. Then, each spectrum is normalized by dividing it by A.
This procedure must be checked to be (largely) independent of the energy interval over which the area A is computed. It has been tested by applying it to data taken from [116], in which the whole EXAFS region is present and the standard normalization procedure is also possible. The test shows that the "new" normalization procedure is only weakly dependent on the energy interval over which the area is computed and that the results obtained in all considered energy intervals are compatible with the ones obtained using the standard procedure, thus allowing to use this new method in the cases, as the one at hand here, where data are available only in a short energy range.
In a further step the edge energies of the various spectra have to be appropriately matched. There is indeed a small (never larger than 0.5 eV), though visible (because around the edge energy E_0 the spectrum is very steep) shift in the edge energy among the various samples.
One can estimate the total error on the final determination of the edge energy to be of the order of 0.4 eV, because of the beam energy resolution, of the absolute calibration of the energy axis and of the ambiguity in the definition of the edge energy itself due to the numerical procedure by which the first derivative of the spectrum is computed and its maximum determined. Taking into account these effects, before performing the analysis all spectra have been shifted by matching their steep rise.
Also the possibility of attributing edge energy differences to different S oxidation states has been taken into account, but it revealed to be not suitable for the systems under analysis. Indeed, systematic studies [130] [131] on S compounds have shown that samples where S is present in different oxidation states may have the same edge energy, and conversely different geometries with S in the same oxidation state lead to appreciable differences (even on the order of a few eV) in the edge energy position.

3.3.4 A semi-quantitative approach to XANES data analysis

In order to interpret the different features among the various spectra in terms of different geometries around the S absorber, two strategies have been used.
A first analysis is made by simply looking at differences among spectra. A qualitative comparison of natural and synthetic melanins spectra is reported in Fig. 3.24. Looking at synthetic melanins, there are small detectable differences between DOPEC and DEC, while the differences between these two and DAC are more pronounced. Furthermore, the DOPEC spectrum looks the most similar to that of NM.

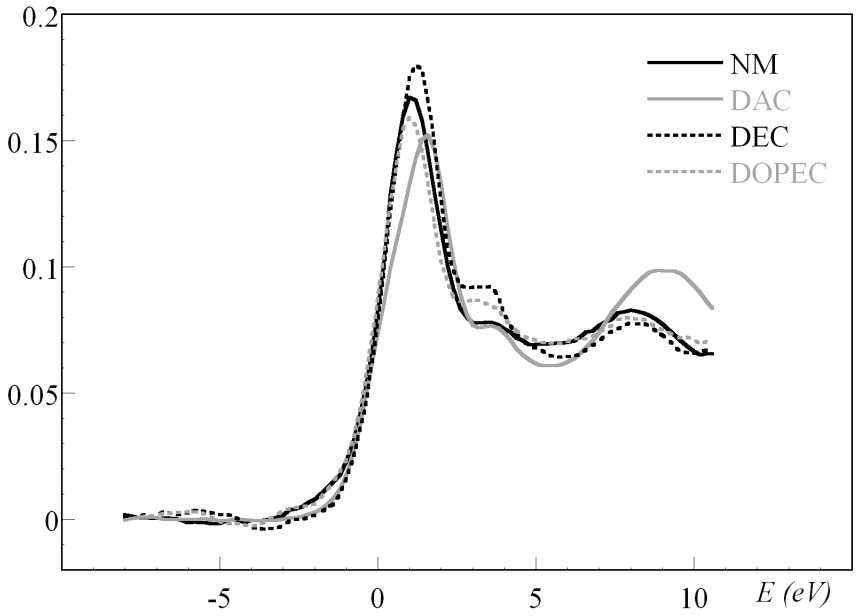

Figure 3.24: Comparison among normalized spectral data of human (NM: black solid line) and synthetic melanins (DAC: gray solid line, DEC: black dotted line, DOPEC: gray dotted line).

Fig. 3.25 shows that the spectral features of the two model compounds are significantly different among them and with respect to human NM. In particular, one clearly sees that bumps and dips are located at significantly different energies.
A second, more refined analysis consists of quantifying the difference between

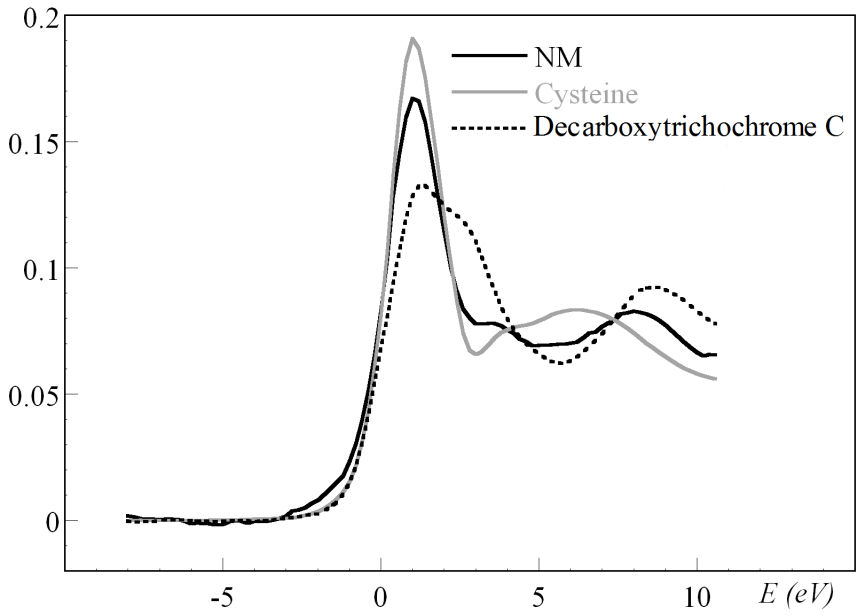

Figure 3.25: Comparison among spectral data of human NM (NM: black solid line) and the two model compounds (cysteine: gray solid line, decarboxytrichochrome C: black dotted line).

the spectra of two generic samples n and m, using the following simple formula

$$\Delta I_{nm} = \sum |y_m(E_k) - y_n(E_k)| \tag{3.7}$$

where $y_i(E_k)$ is the value of the subtracted and normalized i-th spectrum at the (shifted) energy, E_k. The sum extends over a chosen range of energies. ΔI_{nm} is then a measure of sample pair similarity. This analysis has been performed on the natural and synthetic melanins, and the results are collected in Table 3.6. The errors associated to the numbers reported in the table can be estimated to be less than 1%.

In order to separate the contributions to ΔI_{nm} of the different parts of the spectrum, the (3.7) formula has been applied by using the same energy upper limit, E_{Max}=10.6 eV, with two different values for E_{min} namely by excluding (E_{min}=2.0 eV, $\Delta I_{nm} - A$) or including (E_{min}=-2.0 eV, $\Delta I_{nm} - B$) the white-line. Of course the two sets of values of ΔI_{nm} obtained in these ways are numerically different, but they lead to essentially the same order in pair similarity (see third and fifth

Pair	$\Delta I_{nm} - A$	Order	$\Delta I_{nm} - B$	Order
NM-DOPEC	0.05	1	0.03	1
NM-DEC	0.08	2	0.05	3
DEC-DOPEC	0.09	3	0.04	2
NM-DAC	0.14	4	0.09	4
DAC-DEC	0.15	5	0.10	5
DAC-DOPEC	0.16	6	0.10	5

Table 3.6: Spectral differences excluding $\Delta I_{nm} - A$ and including $\Delta I_{nm} - B$ the white-line.

columns of Table 3.6). In particular, ΔI_{nm} is minimum for the NM-DOPEC pair, followed by the NMDEC and DEC-DOPEC pairs, while DAC spectrum is the most different from all the others.

3.3.5 The S local environment: XANES Analysis

The analysis procedure described in the previous paragraph allows to obtain useful semi-quantitative information on spectral similarities among human NM and synthetic compounds. Although a fully quantitative analysis of the XANES spectra is not possible in this case, a more quantitative strategy can be applied. The key observation here is that the XAS spectra of samples such as NM on the one hand, or DAC, DEC and DOPEC on the other, where the absorbing atom can be present in more than one structure, can in principle be obtained as the sum of (appropriately normalized) model compound spectra, weighted by the percentage of the absorbing atom present in each component [95][134]. In the case under examination the absorbing S atom can exist in two different coordination modes, namely in a cysteine-like and in a benzothiazine-like environment. This in principle simple procedure is formally described as the minimization of a χ^2-like function between the experimental spectrum, $y_j(E_k)$, and a theoretical spectrum, $y_{th}(E_k)$, obtained as the linear combination of two other spectra, $y_m(E_k)$ and $y_n(E_k)$. In order to maintain the correct normalization, the weights

used in the linear combination should sum up to 1. This gives

$$y_{th}(E_k) = py_m(E_k) + (1-p)y_n(E_k) \tag{3.8}$$

and the function to be minimized, $R_{[j,mn]}$, is therefore

$$R_{[j,mn]} = \sum_{k=1}^{N} \frac{[y_j(E_k) - py_m(E_k) - (1-p)y_n(E_k)]^2}{\sigma_j(E_k)^2} \tag{3.9}$$

where N is the number of points included in the fit and $\sigma_j(E_k)$ is the estimated statistical error on the normalized data. For simplicity in constructing the function $R_{[j,mn]}$ errors are only attributed to the fitted spectral data.
The minimization of $R_{[j,mn]}$ is straightforward and gives for the best fit value of p the elementary formula:

$$p_{[j,mn]} = \sum_{k=1}^{N} \frac{[y_j(E_k) - y_n(E_k)][y_n(E_k) - y_m(E_k)]}{\sigma_j(E_k)^2} [\sum_{k=1}^{N} \frac{[y_n(E_k) - y_m(E_k)]^2}{\sigma_j(E_k)^2}]^{-1} \tag{3.10}$$

This strategy is used to determine the presence of different components in a sample with unknown structure. In particular, the spectrum of NM and synthetic neuromelanins will be fitted as the sum of the spectra of cysteine and decarboxytrichochrome C. The results obtained by minimizing the likelihood function $R_{[j,mn]}$ are collected in Table 3.7. In column 4 the value of R per degree of freedom (R_{dof}), computed by assuming that the data points included in the computation of R are all statistically independent, is given. A fit is to be considered good when R_{dof} is around 1. The upper panel of Table 3.7 refers to the case where the sum of (3.9) runs over a range of energies that includes the white line, while the lower panel contains the results obtained when the energy region covering the white line is excluded from the sum. The reliability of the method is proved by noting that, within the errors, the values of p reported in both panels of Table 3.7 are the same.
Figs. 3.26, 3.27, 3.28 and 3.29 show the fits obtained by using the percentage written in upper (gray line) and lower (broken line) panel of Table 3.7. Experimental spectra are drawn as solid black line.
The fits obtained including or excluding the white line are essentially indistinguishable, except in the case of DEC. It should be noticed that DEC shows a

Sample	Cysteine	Trichochrome	R_{dof}
NM	64	36	0.92
DOPEC	55	45	1.95
DEC	60	40	1.25
DAC	19	81	5.24
	E_{min}=-2 eV	E_{Max}=10.6 eV	

Sample	Cysteine	Trichochrome	R_{dof}
NM	62	38	0.64
DOPEC	56	44	1.14
DEC	48	52	0.98
DAC	20	80	6.59
	E_{min}=2 eV	E_{Max}=10.6 eV	

Table 3.7: Best fit values of p. In the upper panel considered data are in the energy interval -2.0 to 10.6 eV, which includes the main peak, while in the lower panel the energy interval goes from 2.0 to 10.6 eV and thus does not include the main peak.

more intense white line with respect to NM and DOPEC. The most important conclusion one can draw looking at Figs. 3.26- 3.29 and at the data of Table 3.7 is that a good fit with the NM spectral data is obtained by assuming that S is present in the sample in the cysteine-like and benzothiazine-like environment at the level of about p=64% and (1-p)=36%, respectively, with an uncertainty that can estimated to be $\Delta p \simeq 0.05$. Rather good fits are also obtained for the synthetic melanins DOPEC and DEC. In the case of DOPEC, the values of p are completely insensitive to whether the points under the white line are included or not in the fit, while this is not the case for DEC. The fit to the synthetic neuromelanin DAC data is, in contrast, definitely not good. This may be put in relation to what is indirectly known about its structure on the basis of its preparation process. DAC is, in fact, produced in an auto-oxidation process at the end of which cysteine is removed. It is then not surprising that one cannot fit its spectrum by employing cysteine in addition to decarboxytrichochrome C.

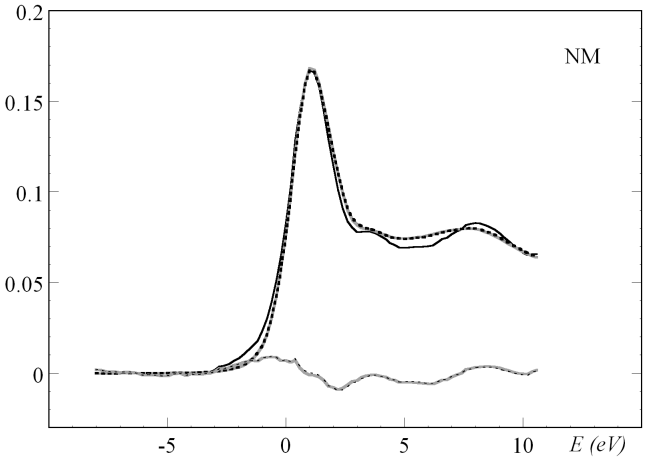

Figure 3.26: NM best fit spectra obtained either by including (gray solid line) or excluding (black dotted line) the white line contribution are drawn superimposed to normalized experimental data (black solid line). The corresponding difference spectra are also shown.

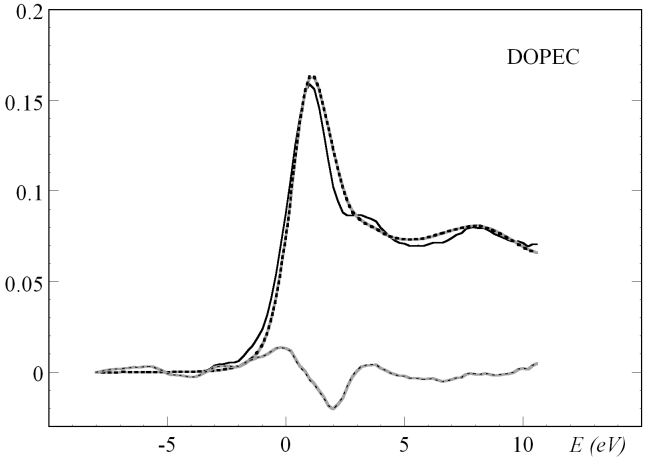

Figure 3.27: DOPEC best fit spectra obtained either by including (gray solid line) or excluding (black dotted line) the white line contribution are drawn superimposed to normalized experimental data (black solid line). The corresponding difference spectra are also shown.

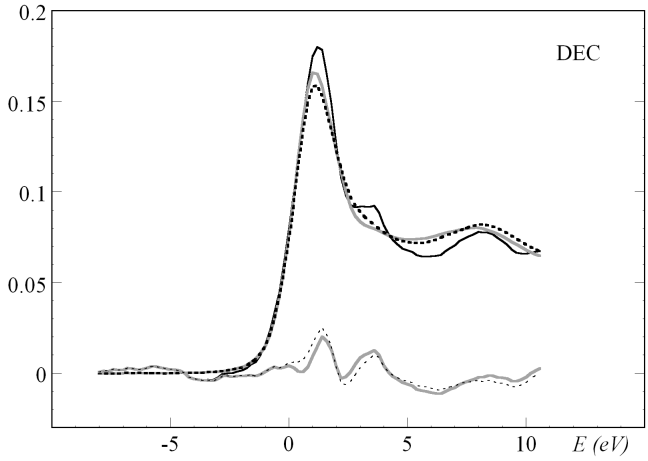

Figure 3.28: DEC best fit spectra obtained either by including (gray solid line) or excluding (black dotted line) the white line contribution are drawn superimposed to normalized experimental data (black solid line). The corresponding difference spectra are also shown.

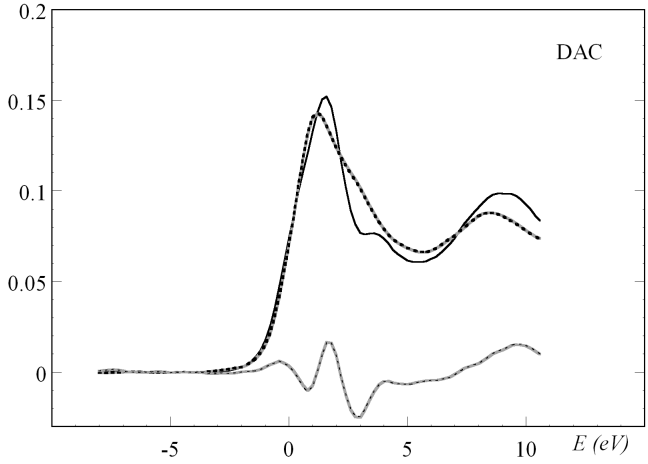

Figure 3.29: DAC best fit spectra obtained either by including (gray solid line) or excluding (black dotted line) the white line contribution are drawn superimposed to normalized experimental data (black solid line). The corresponding difference spectra are also shown.

3.3.6 Discussion and Conclusions

The investigation presented here shows the presence of heterocyclic S of the benzothiazine type in synthetic and human NM. Although previous studies [135] [70]

reported that chemical degradation of pheomelanins and natural NM generates the typical molecules that derive from benzothiazine rings, a direct and nondestructive demonstration of this fact was still missing. The XAS analysis shows in particular that the S environment of NM is similar to the one present in the synthetic melanins produced by enzymatic oxidation, thus suggesting that NM biosynthesis likely involves enzymatic oxidation.

Interestingly the presence of different percentages of the S-containing constituents could be quantitatively assessed through the XAS analysis of the S atomic site. S in NM appears in two different structural coordination modes, namely either bound to a benzothiazine-like ring or present in a cysteine-like environment, in the ratio 64%-36%.

The whole investigation was possible owing to the extraordinary potentialities offered by the XAS spectroscopy, which has been very rarely used in the study of S in biological molecules. In this case, however, it has proved to be a very sensitive technique able to identify even small differences among structurally similar compounds. A quantitative XAS analysis would be probably able to give further details on the local environment around S in these compounds, and to this purpose the results of this study can be exploited to plan and interpret new measurements.

Chapter 4

The active site of human Prolidase

In this chapter another interesting application of XAS to a biologically relevant problem, that is the structural characterization of the metal binding sites in the human prolidase, is presented. The disorder characterized by the deficiency of prolidase content is not at all a neurodegenerative disease. For this reason I devoted a separate chapter to the problem, where both the biomedical introduction and the experimental results are reported together.

The work has been done in collaboration with the Biochemistry Department at the University of Pavia, where the samples have been prepared and characterized, and with Carlo Meneghini from the 'Roma Tre' University. A grateful thanks goes to Wolfram Meyer-Klaucke, who helped us in all the steps of XAS data acquisition.

4.1 Structure and function of human Prolidase

Human prolidase is a protein which deficiency is at the basis of a rare and fatal disease. The work presented here [136] is aimed at understanding the role of different metal ions in modulating prolidase enzymatic activity by characterizing the structure of metal binding sites.

4.1.1 Prolidase and Prolidase Deficiency

Human prolidase is a metalloenzyme that cleaves the iminodipeptides containing a proline or hydroxyproline residue at the C-terminal end of a protein. Because of its function, it is an important enzyme in the latest stages of protein catabolism, particularly of those molecules rich in iminoacids such as collagen [137]. It is known that mutations in prolidase gene cause prolidase deficiency, a rare autosomal recessive connective tissue disorder characterized by intractable skin lesion, mental retardation and respiratory tract infections [138].
The mechanism of prolidase catalysis is still largely unknown. However, prolidase belongs to the so-called 'pita-bread' enzyme family [139], which are characterized by a common reaction mechanism [140]. This family of enzymes takes indeed its name from the presence of a common fold that contains a metal center flanked by well-defined substrate binding pockets. All these enzymes are able to cleave amido-, imido- and amidino-containing peptides bonds, exhibiting relatively narrow substrate specificities when compared to the other metallo-aminopeptidases. Many proteins belonging to the prolidase family have been studied, and in all cases it has been shown that divalent cations such as Zn(II), Mn(II) or Co(II) are necessary for enzymatic activity. In addition, it has been observed that prolidases exist either as monomers or as dimers and that the active site consists of a dinuclear metal clusters coordinated by identical sets of amino acidic residues [141].
There are a few studies aimed at characterizing the structure and behavior of human prolidase. Besides data extrapolated from comparative studies on prolidase from other organisms, recently the 3D structure of human prolidase has been solved. Two structures of this protein are, in fact, deposited in PDB, one with Na(I) (PDB ID: 2iw2) and the other one with Mn(II) (PDB ID: 2okn) in

the active site.
Anyway, the best characterized prolidase in terms of structure and catalytic site composition is the one isolated from the archaeon *Pyrococcus furiosus* (Pfprol) recombinantly produced in *E.coli* [142]. The Pfprol displays a 28% identity with human prolidase and, like the human enzyme, it is a homodimer with 2 subunits. Each monomer has a dinuclear metal cluster requiring Co(II) for full activity, but in the crystallization process these native Co(II) ions are substituted by Zn(II) ions [139].
There also exist full crystallographic data on the 3D structure of the prolidase from the related *Pyrococcus horikoshii* OT3 archaeon (PDB ID: 1wy2) (about 28% identity with human enzyme and 80% identity with Pfprol). From the analysis of known structures five amino acids have been identified as metal-binding residues. It has been demonstrated in fact that mutations at these amino acid sites, namely Glu413, Asp277, Glu453 are relevant also for the structural stability and activity of human prolidase [138].
Few years ago the human prolidase in prokaryotic and eukaryotic hosts has been synthesized by Lupi *et al.*. They showed that the recombinant enzyme has a molecular weight of 57 kDa and has optimal activity at pH=pH7.8 and T=50°C. Furthermore Mn is required for its full activity. They also demonstrated that the thermal stability of recombinant and endogenous enzyme are pretty similar [143].

4.1.2 Experimental Details

Sample preparation and characterization

Recombinant human prolidase is produced in BL21 *E. coli* cells as fusion protein with an N-terminal His tag. The His tag is attached because, thanks to its high affinity for metal ions, it allows to purify the protein using affinity chromatography. The protein is incubated for 1 h at 50°C with Mn, as described in [143]. After the purification, the His tag is removed using an Xa digestion factor, then the protein is extensively dialyzed against 10 mM TrisHCl pH 7.8, 0.57 mM dithiothreitrol (DTT) and 300 mM NaCl.
Two different protein preparations, P1 and P2, purified independently from glyc-

erol stock of transformed bacteria, are obtained for XAS study. The two independent preparations are concentrated by a quick dialysis against PEG 20000 to reduce the sample volume to 100 μl keeping the protein in solution. Protein concentration is determined by the method of Lowry [144] using bovine serum albumin as standard. Taking into account that the recombinant enzyme is obtained mainly in dimeric form, as determined by gel filtration chromatography [145], the two different protein preparation solutions, P1 and P2, are found to have a concentration of (32 $\pm$ 3) μM and (78 $\pm$ 8) μM, respectively. It is found that a large amount of Zn is present in both preparations probably originating from the Zn ions present into bacteria cells. An overview of the prepared samples is given in Table 4.1. The amount of divalent metals present in solution

	[Protein] (μm)	[Mn]	[Zn]
MeP1	(32 $\pm$ 3)	(28 $\pm$ 3) μM	(90 $\pm$ 10) μM
MeP2	(78 $\pm$ 8)	(55 $\pm$ 6) μM	(750 $\pm$ 70) μM
MnB	0	(2.0 $\pm$ 0.1) mM	0
ZnB	0	0	(2.0 $\pm$ 0.1) mM

Table 4.1: Protein and metal concentrations of preparations MeP1 and MeP2 (Me = Mn/Zn).

is measured using inductively coupled plasma-mass spectrometry (ICP-MS) on a Perkin Elmer instrument. Indeed, while the ratio [protein]:[Mn] concentration is 1:1 for both samples, the ratio [protein]:[Zn] is about 1:3 in sample P1 and it reaches the value 1:10 in sample P2. Recalling that each protein molecule can host at most four metal ions in the active sites (there is a dinuclear site for each of the two monomers), in the case of sample P1 the totality of the available metal ions is bound to the protein. On the contrary, in the case of sample P2, an excess of Zn ions is possibly free in solution.

The enzymatic activity is evaluated according to the method proposed by Myara [146], i.e. by using absorption spectroscopy to detect the quantity of substrate, namely the Gly-Pro dipeptide, processed by the enzyme. The specific enzymatic activity is measured with no further addition of both Mn and Zn ions and found to be (2.3 $\pm$ 0.7) 10^3 μmol proline $hour^{-1}$ mg^{-1}. Activity is also measured in

excess (10 mM) of either Mn or Zn. At such high concentration all the four active sites are assumed to be homogeneously loaded with Mn or Zn, respectively. At 10 mM $MnCl_2$ the specific activity is 9500 ± 7 μmol proline $hour^{-1}$ mg^{-1}, while at 10 mM $ZnCl_2$ it was 800 ± 40 μmol proline $hour^{-1}$ mg^{-1}. These values are about four times higher and three times lower than basal activity, respectively.

XAS Data Collection

XAS data have been collected at the D2 bending magnet beam line of the EMBL Outstation Hamburg at DESY. The synchrotron was operating at 4.5 GeV with ring currents ranging from 90 to 149 mA. A Si[111] double crystal monochromator and a focusing mirror with a cut-off energy of 21.5 keV have been used. Spectra were recorded in fluorescence mode using a 13-elements Ge solid-state detector (Canberra, Meriden, CT, USA). The samples were kept at 20 K in a He close-cycle cryostat (Oxford Instruments) throughout the whole measurement session. Upon measurement, 25 μl of each sample are transferred in a 1-mm thick plastic holder closed by two Kapton windows, rapidly frozen in liquid nitrogen and immediately brought to the experimental hutch.

XAS Data Reduction

For each sample several (from 34 to 47) XAS spectra have been collected and averaged. After background subtraction, the resulting spectrum is normalized using the Kemp software [112] and the spectroscopic signal extracted using the Athena software [91]. Extended X-ray absorption fine structure data are analyzed using the FITEXA software [147], which exploits the FEFF8.2 package [148] for the calculation of backscattering amplitudes, total phase shifts and photoelectron mean free path. The best fit is achieved by minimizing the quantity

$$\xi^2 = \frac{1}{N_p} \sum_{i=1}^{N_p} [k_i(\chi_{exp}(k_i) - \chi_{th}(k_i))]^2 \tag{4.1}$$

where χ_{exp} and χ_{th} are the experimental and theoretical data, respectively, and the sum is over the N_p collected data points. The MINUIT [149] subroutine of CERN library is used for data refinement and statistical error analysis. The fit

quality is measured by the associated R^2-factor defined by the formula

$$R^2 = 100\frac{N_p\xi^2}{W_0^2}\%, \tag{4.2}$$

where

$$W_0 = \sum_i [k_i(\chi_{exp}(k_i))]^2 \tag{4.3}$$

A value of R^2 of about 10% is to be considered satisfactory for complex biological molecules.
In the fitting procedure the experimental data are weighted by a factor k to compensate for the rapid decrease of the XAS signal with increasing k.
In order to get an acceptable signal-to-noise ratio, the analysis is done only over the data of sample P1 at the Zn K-edge (owing to the absence of free Zn in solution) and of sample P2 at the Mn K-edge (owing to the sufficiently high absorber concentration).
The buffer in which protein is dissolved, namely 10 mM Tris-HCl, pH 7.8, 0.57 mM DTT and 0.3 M NaCl has been also subjected to XAS measurement both in presence of 2 mM $MnCl_2$ (MnB) and of 2 mM $ZnCl_2$ (ZnB). The last two samples have been used to check the difference between the structure of the metal free in solution (in buffer in the absence of the protein) and bound to the protein.

4.1.3 XAS Data Analysis

XANES qualitative analysis

Qualitative comparisons of prolidase XANES spectra with the corresponding metal ions in buffer (Fig. 4.1) shows significant structural differences both at the Mn (left panel) and at the Zn (right panel) K-edge.
For what concerns Mn spectra, the significant differences between MnP2 and MnB prove that Mn ions are bound to the protein.
Going to Zn XANES spectra it is quite evident that the ZnP2 displays features which are in between those of spectrum ZnP1 and of buffer solution (ZnB), thus suggesting the hypothesis according to which the Zn excess in sample P2 is free in solution.

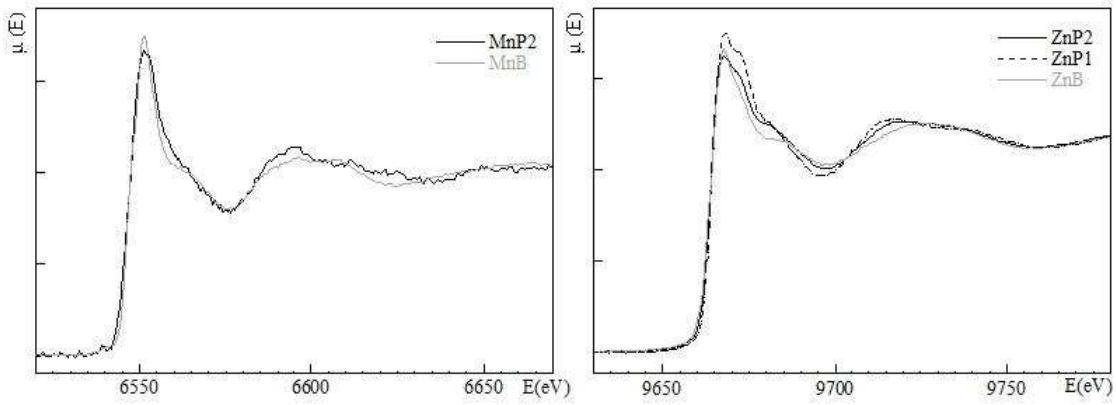

Figure 4.1: Comparison of the XANES spectra at the Mn K-edge of sample P2 (MnP2, black line) and buffer (MnB, gray line). Comparison of the XANES spectra at the Zn K-edge of sample P2 (ZnP2, full black line), P1 (ZnP1, broken black line), and buffer (ZnB, gray line).

EXAFS qualitative analysis

We decided to check the hypothesis of the presence of the Zn free in solution in sample P2 by trying to reproduce the spectrum of ZnP2 as the superposition of a fraction, α, of the ZnP1 and a fraction (1-α) of ZnB spectra. Under this assumption the following formula holds

$$\chi^{th}(k) = \alpha\chi_{ZnP1}(k) + (1-\alpha)\chi_{ZnB}(k), \tag{4.4}$$

where α is determined by minimizing the objective function

$$\begin{aligned} F(\alpha) &= \sum_k k^2 |\chi_{ZnP2}(k) - \chi^{th}(k)|^2 = \\ &= \sum_k k^2 |\chi_{ZnP2}(k) - \alpha\chi_{ZnP1}(k) - (1-\alpha)\chi_{ZnB}(k)|^2 \end{aligned} \tag{4.5}$$

In Eq.(4.5), the sum is extended over the whole k range. The best fit (Fig. 4.2) gives α=(44 $\pm$ 8)%

Interestingly enough, even such a rough analysis ends up with a nice quantitative result, namely, within the error, α is compatible with the hypothesis that in the P2 sample about two-third of the whole amount of Zn is free in solution (see Tab. 4.1). For this reason, the quantitative EXAFS analysis described in the

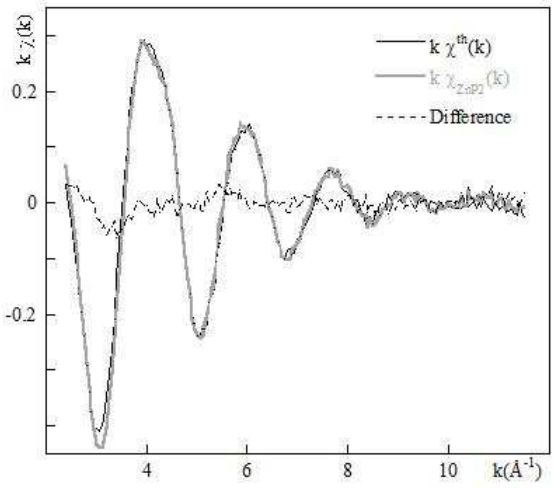

Figure 4.2: Experimental spectrum χ_{ZnP2}(k) (in gray) superimposed to χ^{th}(k) (in black) computed at the best fit value α=(44±8)%

following paragraph is limited, for the Zn K-edge data, to the spectrum of the ZnP1 sample, where all the Zn is supposed to be bound to the protein active sites.

EXAFS quantitative analysis

-Model building

In order to have a good starting model for the quantitative fits, the information available in the PDB, where structures of prolidase expressed in various organisms and in complex with different metal ions are collected, is exploited. However, none of the deposited prolidase structures is found to be simultaneously in complex with two different types of metal ions, therefore the starting model is built using complementary geometrical information coming from the following two structures:

1. Human prolidase in complex with Mn (PDB ID: 2okn);
2. *P. horikoshii* OT3 prolidase in complex with Zn (PDB ID: 1wy2).

The 3D structures of these two complexes are taken as models for the Mn and Zn coordination mode, respectively. In both the cases the protein is a dimer made of two identical monomers (identified as monomer 1 and monomer 2 in the fol-

lowing) and each monomer can host two metal ions in a dinuclear binding site, in which the two ions are bound in structurally distinct configurations (site A and site B, see Fig. 4.3). In each protein molecule there are, therefore, four distinct metal binding sites that are indicated by A1 and A2 (highlighted in green) and B1 and B2 (highlighted in magenta) in Fig. 4.3.

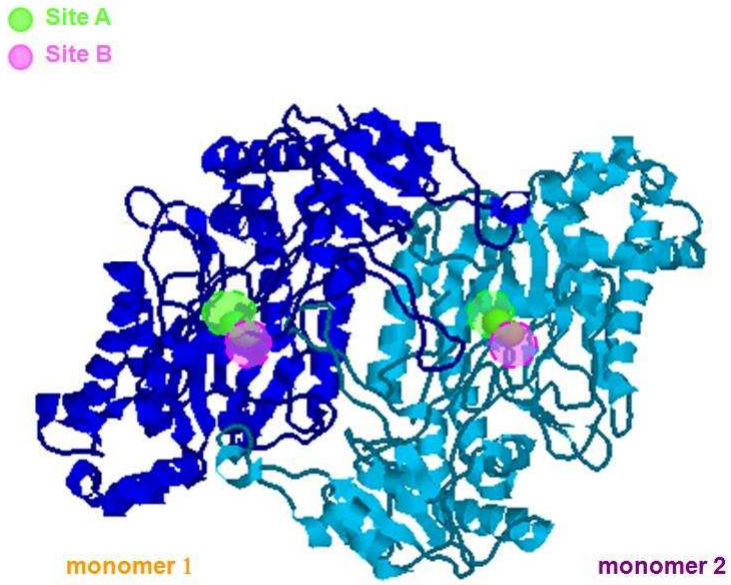

Figure 4.3: A cartoon of the prolidase dimer. Sites A are highlighted in green and sites B in magenta. The crystal structure of human recombinant prolidase is used for the sketch.

In Table 4.2 the metal coordination modes of the two selected structures are summarized by writing the type and the number of atoms bound to the metal ion in the four different sites. It is important to underline that sites of type A, where a His residue is one of the ligands, are different from the sites of type B with respect to the EXAFS signal associated to them. The metal coordination mode in sites A1 and A2 are identical in the crystallographic structure of human prolidase and *P.horikoshii* OT3, while the B sites are different.
Relying on the observation that the concentration ratio [protein]:[Mn] measured in all the samples is 1:1 (see Table 4.1), it is reasonable to assume that out of the four prolidase binding sites one is occupied by a Mn ion and the remaining ones by three Zn ions. Thus the four combinations of metal occupations shown

Complexes	A1	B1	A2	B2
2okn (Mn)	4 O, 1 N (His)	5 O	4 O, 1 N (His)	6 O
1wy2 (Zn)	4 O, 1 N (His)	4 O	4 O, 1 N (His)	4 O

Table 4.2: Metal coordination mode at the A1, B1, A2, B2 sites in the 2okn and 1wy2 complexes.

in Table 4.3 are possible. Actually only two of them (S_1 and S_2) are significantly different. In fact, as remarked above, the site environments S_2' and S_2 are identical because the Mn coordination modes in sites A1 and A2 are identical. The site environments S_1 and S_1' are instead similar, but not exactly equal because (see Table 4.2) in S_1 Mn is coordinated to five oxygen atoms (site B1), while in S_1' it is coordinated to six oxygen atoms (site B2).

Combinations	A1	B1	A2	B2
S_1	Zn	Mn	Zn	Zn
S_2	Mn	Zn	Zn	Zn
S_1'	Zn	Zn	Zn	Mn
S_2'=S_2	Zn	Zn	Mn	Zn

Table 4.3: The four possible metal occupations of sites A1, B1, A2, B2.

Mn K-edge spectrum

The fit at the Mn K-edge is carried out only on the MnP2 EXAFS spectrum because the Mn concentration in sample P1 (see Table 4.1) is too low to yield a sufficiently good experimental signal-to-noise ratio. Since the protein to metal concentration ratio is 1:1, the χ_{MnP2}(k) EXAFS signal is fitted assuming that the Mn coordination mode is unique and structurally of the kind found in the 2okn complex, as reported in Table 4.2. The 3D structures of the three different Mn sites (A1≡A2) listed in the first row of Table 4.1, appropriately modified to host an extra Zn ion next to the Mn absorber, are therefore chosen as starting models.

Among the configurations listed in Table 4.3, the one that gives rise to the best fit is S_1', in which Mn is located in the B2 site. The quality factor of the fit is

rather good giving $R^2 = 11\%$, while a larger value ($R^2 = 15\%$) is obtained if Mn is assumed to be located in the B1 or in the A1≡A2 site.
The best fit spectrum is drawn as a black curve in Fig. 4.4 superimposed to the experimental signal (in gray) together with the corresponding FT. The best fit parameters are reported in Table 4.4.

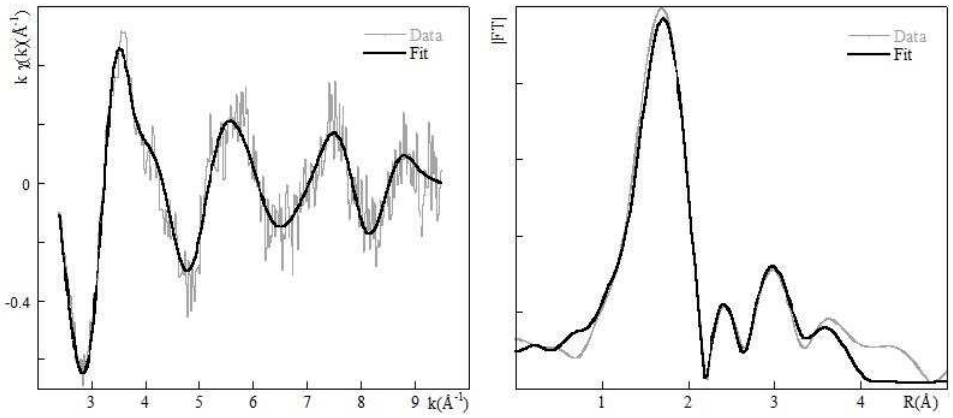

Figure 4.4: Experimental data (gray line) and theoretical fit (black line) at the Mn K-edge (left panel) and corresponding FT (right panel).

Scatterer	**N**	**r**$\pm\delta$**r** (Å)	**DW**$\pm\delta$**DW**(Å^2)
O	6	2.23 ± 0.01	(1.1 ± 0.5)*10^{-3}
Zn	1	3.40 ± 0.01	(1.2 ± 1)*10^{-3}

Table 4.4: Best fit parameters from the MnP2 spectrum.

Zn K-edge spectra

Exploiting the information gathered from the previous fit (i.e., that Mn is located in the B2 site), it is reasonable to assume that the three Zn ions occupy the sites A1, A2 and B1. In this situation the measured EXAFS signal at the Zn K-edge will be the sum of three contributions:
1. χ_{A1}(k), in which the photo-electron is extracted from the Zn ion sitting in site A1 and sees another Zn ion which sits nearby in site B1;
2. χ_{B1}(k), where the extracted photo-electron belongs to the Zn ion located in site B1 and, as before, another Zn ion sits nearby in site A1;
3. χ_{A2}(k), in which the extracted photo-electron comes from the Zn ion located

in site A2 and now time among the near scatterers there is a Mn ion sitting in site B2.

The χ_{ZnP2}(k) spectrum will be therefore given by the sum of these 3 contributions

$$\chi_{ZnP2}(k) = \frac{1}{3}[\chi_{A1}(k) + \chi_{B1}(k) + \chi_{A2}(k)] \tag{4.6}$$

This model allows to very well reproduce the experimental spectrum, as quantitatively confirmed by the obtained R^2=3%. The best fit spectrum is drawn as a black curve in Fig. 4.5 superimposed to the experimental signal (in gray) together with the corresponding FT. The best fit parameters are reported in Table 4.5. It is also very important to underline that the Zn-Mn distance obtained for the fit at Zn K-edge is compatible with the one obtained independently from the fit at Mn K-edge.

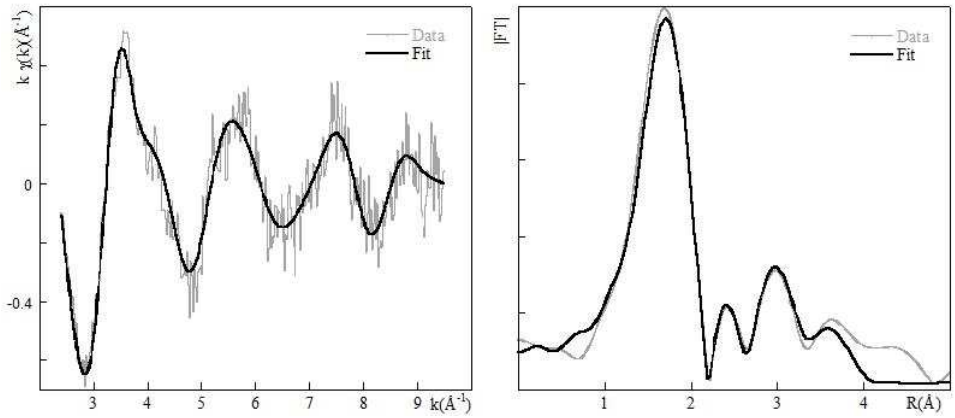

Figure 4.5: Experimental data (gray line) and theoretical fit (black line) at the Mn K-edge (left panel) and corresponding FT (right panel).

Discussion and conclusions

The XAS study presented here, also supported by results obtained using standard laboratory techniques, in particular ICP-MS, provides a biochemical and structural characterization of human prolidase and shows the existence of het-

Site	**Scatterer**	**N**	**r**$\pm\delta$**r** (Å)	**DW**$\pm\delta$**DW**(Å^2)
A1	O	4	2.05 ± 0.01	(1.5 ± 0.4)*10^{-3}
A1	N	1	2.05 ± 0.01	(1.5 ± 0.4)*10^{-3}
A1	Zn	1	3.21 ± 0.04	(2.3 ± 1.5)*10^{-3}
A2	O	4	2.05 ± 0.01	(1.5 ± 0.4)*10^{-3}
A2	N	1	2.05 ± 0.01	(1.5 ± 0.4)*10^{-3}
A2	Mn	1	3.37 ± 0.03	(2.3 ± 1.5)*10^{-3}
B2	O	4	1.90 ± 0.01	(1.5 ± 0.4)*10^{-3}
B2	Zn	1	3.21 ± 0.04	(2.3 ± 1.5)*10^{-3}

Table 4.5: Best fit parameters from the ZnP2 spectrum.

erogeneous dimeric metallic sites in the active form of the protein. Enzymatic activity measurements demonstrate indeed that, even in the presence of an excess of Zn ions, the protein partially retains its activity if at least one, out of the four metal binding sites, is occupied by a Mn ion. Furthermore, as shown in the cartoon of Fig. 4.6, the XAS data analysis allows to solve the atomic structure around each metal binding site.

It is worth remarking that the recombinant human prolidase preparations is preincubated in the presence of $MnCl_2$ and, at the end of the various purification steps, only one Mn ion per dimer is present. Our analysis has allowed the identification of the site wherein the purified dimeric enzyme one Mn ion remains bound to the protein, after the successive Mn substitutions by Zn in the other sites.

Actually it is still unclear whether the presence of Zn ions bound to the high affinity His-related A1 and A2 sites is an artifact of the preparation procedure or whether it also occurs *in vivo*. This last is not an unrealistic hypothesis as the concentration of Zn in biological systems is usually much larger than that of Mn. Indeed, one might argue that the presence of heteromeric dinuclear sites is important for in vivo protein activity regulation [150], with Zn having a structural function and Mn a role in promoting protein activity.

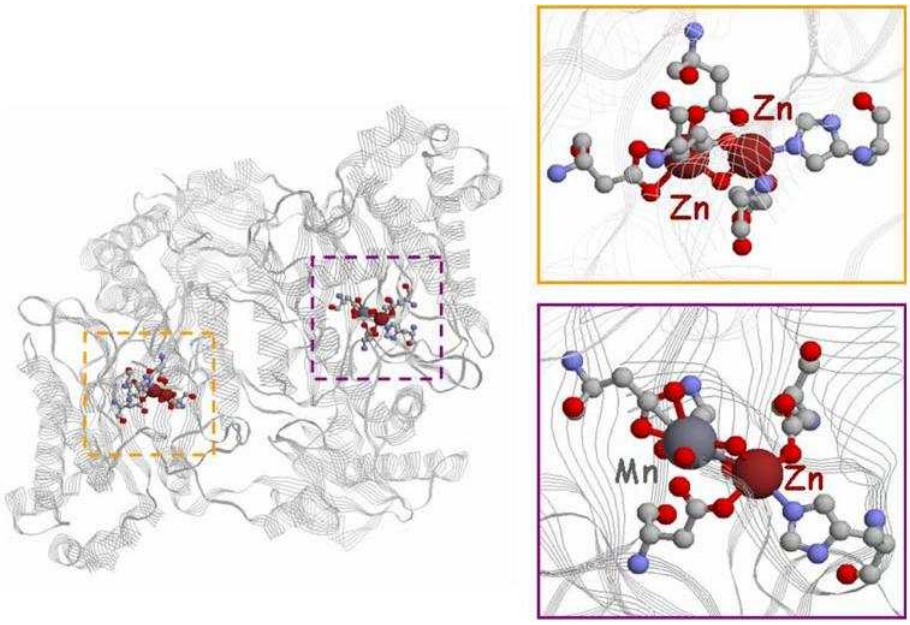

Figure 4.6: A cartoon of the geometries of the four prolidase metal binding sites as derived from XAS data analysis.

Chapter 5

Conclusions

In this concluding chapter I first summarize the main results of the work reported in the thesis and then I underline the common mechanisms present in the studied biological systems. A second section is dedicated to future perspectives. Some of them refer to projects and collaborations which have already been started, even though they are in a preliminary stage, some others are for the moment ideas, but that can be concretely realized within the framework defined in this thesis.

5.1 Summary

The unifying theme of this thesis is the XAS study of the structural pathogenetic protein modifications underlying the development of neurodegenerative diseases. Indeed an important section is dedicated to the study of the interaction of Cu and Zn ions with the Aβ peptides and to their role in AD pathogenesis. The most interesting finding which emerges from this work is that Cu and Zn ions have different coordination modes and hence different behaviors in association with Aβ peptides. In particular, XAS measurements show that Cu coordination is consistent with an intra-peptide coordination mode, while the Zn coordination suggests an inter-peptide binding mode. This, together with the results of OD and FTIR measurements, indicates that Zn happens to be more effective than Cu in promoting Aβ aggregation.
Also in the interaction with the PrP octarepeat subdomain (PrP is the protein that is known to be involved in TSEs diseases) these two metals appear to behave differently. EPR measurements in fact clearly show that the Cu affinity for the peptide is higher than that of Zn and that Cu can bind PrP in basically three different ways according to the [Cu]:[PrP] concentration ratio. XAS measurements, combined with EPR results, besides demonstrating that Zn ions affect the Cu coordination mode, allow to determine the Zn coordination mode to PrP.
The other important subject of this thesis is the study of the local environment around S in human NM (a molecule that plays an important role in PD etiology) and synthetic melanins prepared with different procedures. The analysis of the XANES region of spectra acquired at the S K-edge shows that the S environment in human NM is similar to the one present in the synthetic melanins produced by enzymatic oxidation, thus suggesting that NM biosynthesis likely involves enzymatic oxidation.
Finally, XAS was employed to study the metal binding sites of human Prolidase, whose deficiency is known to be related to the "prolidase deficiency disease". In particular, XAS puts in evidence that Mn and Zn ions are simultaneously present in the protein yielding accurate information about the local environment of the two metals. Enzymatic activity measurements show that the protein is active in the presence of Zn ions if at least one out of the four metal binding sites is

occupied by a Mn ion. The XAS data analysis allows to solve separately the atomic structure of each metal binding site.

5.1.1 AD, TSEs and PD: Similarities and Inter-relationships

It is worth remarking that the biological problems examined in this thesis are strictly related. First of all, AD, TSEs and PD all belong to the PCD's family, a class of diseases associated with the misfolding of some specific protein. Furthermore, in the insurgence of these diseases metals have been suggested to play an important role either through metal induced conformational changes or because they are involved in free radicals and other neurotoxic factors production. In the following, a short description of the common biological and structural mechanisms involved in AD, TSEs and PD pathogenesis is given.
AD and TSEs share many common features [153]. In both cases proteins with similar properties of aggregation and accumulation in the brain (Aβ and PrP, respectively) are involved. The main similarities are the conserved histidine metal-binding domains, certain transmembrane recognition motifs, the presence of methionine residues and the location of the conserved tyrosine residues. High affinity metal binding sites, characterized by the presence of His residues, are present both in Aβ and PrP. Interactions with metal ions, most specifically with Cu and Zn, have important roles in the biochemistry of the proteins and mediates peptides misfolding and aggregation.
Interestingly enough it has been shown that PrP^C may play a critical role in the pathogenesis of AD by interacting with beta-secretase BACE1 and inhibiting its activity. Indeed it has been reported in [151] that cellular overexpression of PrP^C inhibits APP β-secretase cleavage and reduces Aβ formation. Conversely, depletion of PrP^C in mouse cells leads to an increase in Aβ peptides levels. The authors also showed that two mutants forms of PrP, that are associated with familial human prion diseases, are not able to inhibit the β-secretase cleavage of APP. Taking into account all these results, a recent study [152] suggests that in the normal brain there is a feedback loop where PrP^C exerts an inhibitory effect on BACE1 to decrease Aβ and the amyloid intracellular domain (AICD) production. PrP^C is a kind of receptor for Aβ oligomers and the expression of PrP^C

appears to be controlled by AICD. In turn, AICD upregulates PrP^C expression, thus maintaining the inhibitory effect of PrP^C on BACE1. In AD this feedback loop is disrupted, and an increased level of Aβ oligomers binds PrP^C preventing the latter to regulate BACE1 activity.

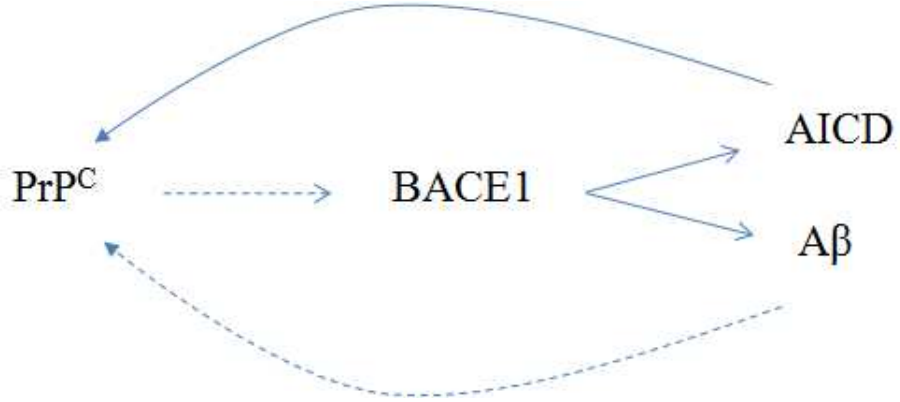

Figure 5.1: Feedback loop among PrP, BACE1, Aβ and AICD. Continuous lines represent an upregulatory effect, while broken lines represent an inhibitory effect.

There are also common features in AD and PD pathogenesis. The most striking ones are the similarities between Aβ peptides and α synuclein aggregation processes. Of even broader interest in the context of this thesis is the parallelism between Aβ and NM [154].
First of all, both molecules accumulate with ageing, which is the greatest risk factor for AD and PD. Secondly, although their structures are definitively different, they have been supposed to play similar roles in neuroprotection, in particular in maintaining the correct metal ion balance. The presence of metals is, in fact, required to catalyze Aβ and NM production. These proteins have high metal affinities and are thus able to generate stable complexes, playing in this way a protective role against metal toxicity.
Finally, both Aβ and NM are involved in similar aspects of neuronal death processes underlying AD and PD diseases, respectively. For example, both molecules can activate microglia, inducing release of toxic factors such as tumor necrosis factor-α, interleukin-6 and nitric oxide.
According to the physio-chemical conditions, both NM and Aβ seem to be able to participate in cell death and protection. In the case of PD, NM levels are high in SN dopaminergic neurons that are the most prone to degeneration. How-

ever, it is not at all clear if this NM is part of the toxic events that underlie PD or a protective response that may slow down the development of the disease. Similarly Aβ peptides may have neuroprotective properties as a result of their ability to trap metals, thus removing toxic species such as oligopeptides. A careful analysis of these effects may therefore lead to a deeper understanding of the role played by Aβ and NM in neurodegenerative processes and provide some insight into possible common mechanisms in the pathogenesis of these devastating pathologies.

5.2 Future Perspectives

The investigation presented in this thesis is aimed at improving our understanding of the biological and bio-medical processes which are relevant in the pathogenesis of neurodegenerative diseases, mainly through the determination of structural features of involved proteins and molecules. This section describes some new directions of experimental studies which can be performed exploiting the methods and the ideas described in this work.

5.2.1 Metal Ions-Aβ Peptides Complexes

The study of metal-Aβ complexes has been for many years a hot topic in biophysical research. Many aspects of this problem have been gradually clarified, but there is still a lot of work to do in order to obtain a complete and consistent picture of the situation. In the following a number of further experiments are described that would be of much help to clarify the structure of the metal site as well as the complex biochemical processes that are at the basis of the development of AD, TSE and PD.

Let us start with AD. Here it would be of great importance to make XAS experiments on Aβ peptides with punctually modified amino acidic sequence with the respect to the normal protein. A selective substitution of the residues involved in metal binding can indeed help to better understand the specificity of single amino acids residues in metal binding. This approach has been already successfully tried using many different techniques (see for example [26] and [35]). To complete these studies it would be interesting to also use XAS in order to detect with atomic resolution the effects of the changes in the local structure around the metal. In particular, the chemical modification of the His residues present in the sequence or their substitution with Alanine residues could help in determining their specific role in Cu and/or Zn binding. Also the substitution of Tyr10 would be interesting, because it would allow to clarify whether this residue is directly bound to the metal or not.

Another relevant question that deserves a dedicated investigation is the study of the behavior of Aβ peptides in complex with metal other than Cu or Zn. A metal which should be considered is Fe, because it has been shown to be present

at increased concentrations in amyloid plaques [23]. XAS has never been used to study Fe-Aβ complexes, while there exists many cases where XAS has been successfully used for structural studies of Fe containing biological complexes. The experience we gained in dealing with Cu- and Zn-Aβ complexes can thus be instrumental in performing XAS studies of Fe-Aβ complexes.
Another metal which has been often considered to be relevant because of its not fully elucidated relationships with Aβ is Al. Significant Al concentrations in the brain of AD patients have been well established [155] [156], but its role in the aetiology of the disease is still controversial [157].
In order to clarify this point we have started a project, in collaboration with the Prof. Zatta's group in the Biology Department of the University of Padova, with the goal of acquiring XAS measurements on Al-Aβ peptides complexes. We have made some preliminary tests on these systems at the LUCIA beamline c/o the Swiss Light Source. The tests were essentially aimed at defining a suitable experimental set up by which spectra in the Al K-edge energy range (the Al K-edge energy is 1560 eV, thus much lower than the edge-energy of higher Z elements such as Cu and Zn) could be taken with sufficiently good noise-to-signal ratio. A number of problems, such as the absorption of water and the choice of the nature of the membrane holder to be used to contain the sample, arise in this energy range. Appropriate measurement protocols have yet to be developed.

5.2.2 Metal Ions-PrP Complexes

Although a lot of work has already been done to elucidate metal ions-PrP interactions, there are obviously many questions waiting for an answer. For instance, it would be very interesting to carry out an exhaustive XAS study of the Zn binding modes in the absence of Cu ions. We recall that in the measurements discussed in this thesis, the Zn coordination mode has been only studied in the presence of Cu ions. Planning a new set of measurements of Zn-complexes in the absence of Cu ions (analogously to what has been done with Cu) at different [Zn]:[PrP] concentration ratios would then allow us to complete the characterization of the Zn binding mode.

5.2.3 Neuromelanin

For what concerns the researches related to NM, the work described in this thesis could be extended acquiring new data on natural melanins extracted from different brain regions in association with data on other type of model compounds. In addition new theoretical tools for a more quantitative analysis on the XANES region should be developed to allow for a more reliable interpretation of this part of the XAS spectrum.
Another interesting line of investigation could be the study of the interaction between NM and Fe ions. Given the high affinity of NM for Fe, it should not be too difficult to set up a plan aimed at performing XAS measurements of natural NM at the iron K-edge.

Abbreviations

Aβ: Beta Amyloid
AD: Alzheimer's Disease
AEY: Auger Electron Yield
AICD: Amyloid Intracellular Domain
CAA: Cerebral Amyloid Angiopathy
CD: Circular Dichroism
CNS: Central Nervous System
CP: Car-Parrinello
DETPA: Diethylene Triamine Pentaacetic Acid
DTT: Dithiothreitrol
DFT: Density Functional Theory
EPR: Electron Paramagnetic Resonance
EXAFS: Extended X-ray Absorption Fine Structure
FEL: Free Electron Laser
FTIR: Fourier Transform Infrared Spectroscopy
ICP-MS: Inductively Coupled Plasma - Mass Spectrometry
LC: Locus Coeruleus
MDB: Metalloprotein Database and Browser
MMSE: Mini Mental State Examination
MRI: Magnetic Resonance Imaging
NEMO: N-ethyl morpholine
NMR: Nuclear Magnetic Resonance
PEG: Polyethylene Glycol

PET: Positron Emission Tomography

PDB: Protein Data Bank

PrP: Prion Protein

SR: Synchrotron Radiation

TEY: Total Electron Yield

UV-Vis: Ultra Violet-Visible

XAFS: X-ray Absorption Fine Structure

XANES: X-ray Absorption Near Edge Spectroscopy

XAS: X-ray Absorption Spectroscopy

XRD: X-Ray Diffraction

Bibliography

[1] L.Stryer (1995) *Biochemistry.* W.H.Freeman & Company.

[2] S.Morante *Metal ions and protein aggregation: the case of Prion protein and β-amyloids.* PhD school lectures, University of Rome "Tor Vergata".

[3] K.J.Barnham, C.L.Masters, A.I.Bush (2004) *Neurodegenerative diseases and oxidative stress.* Nature Reviews Drug Discovery 3: 205-214.

[4] S. Morante (2008) *Metal ions and protein aggregation: the case of Prion protein and β-amyloids.* Invited review in Biophysical Inquiry into Protein Aggregation and Amyloid Diseases, eds. D. Bulone and P.L. San Biagio, Research Signpost Edition, Ch. 3.

[5] D.J.Selkoe (2003) *Protein folding in fatal ways.* Nature 426: 900-905.

[6] C.M.Dobson (2003) *Protein folding and misfolding.* Nature 426: 884-890.

[7] K.Blennow, M.J.de Leon, H.Zetterberge (2006) *Alzheimers disease.* Lancet 386: 387-403.

[8] D.J. Selkoe (2001) *Alzheimers disease: genes, proteins ant therapy.* Physiological Reviews 81: 741-766.

[9] C.Haass, M.C.Schlossmarcher, A.Y.Hung (1992) *Amyloid beta-peptide is produced by cultured cells during normal metabolism.* Nature 359: 322-325.

[10] P.K.Panegyres (2001) *The functions of the amyloid precursor protein gene.* Review of Neuroscience 12: 1-39.

[11] G.M.Shankar, S.Li, T.H.Mehta, A.Garcia-Munoz, N.E.Shepardson, I.Smith, F.M.Brett, M.A.Farrell, M.J.Rowan, C.A.Lemere, C.M.Regan, D.M.Walsh, B.L.Sabatini, D.J.Selkoe (2008) *Amyloid-β protein dimers isolated directly from Alzheimers brains impair synaptic plasticity and memory.* Nature Medicine 14: 837-842.

[12] A.Goate, M.C. Chartier-Harlin, M.Mullan, J.Brown, F.Crawford, L.Fidani, L.Giuffra, A.Haynes, N.Irving, L.James, R.Mantparallel, P.Newton, K.Rooke, P.Roques, C.Talbot, M.Pericak-Vance, A.Roses, R.Williamson, M.Rossor, M.Owenparallel, J.Hardy (1991) *Segregation of a missense mutation in the amyloid precursor protein gene with familial Alzheimers disease.* Nature 349: 704-706.

[13] A.Rauk (2009) *The chemistry of Alzheimers disease.* Chemical Society Reviews 38: 2698-2715.

[14] M.L.Hemming, J.E.Elias, S.P.Gygi, D.J.Selkoe (2008) *Proteomic Profiling of c-Secretase Substrates and Mapping of Substrate Requirements.* PLoS Biology 6: 2314-2328.

[15] A.I.Bush (2003) *The metallobiology of Alzheimers disease.* Trends in Neuroscience 26: 207-214.

[16] E.E.Smith, S.M.Greenberg (2009) *β-amyloid, blood vessels and brain function.* McGraw-Hill, New York, U.S.A.

[17] W.E.Klunk, H.Engler, A.Nordberg, Y.Wang, G.Blomqvist, D.P.Holt, M.Bergstrom, I.Savitcheva, G.Huang, S.Estrada, B.Ausen, M.L.Debnath, J.Barletta, J.C.Price, J.Sandell, B.J.Lopresti, A.Wall, P.Koivisto, G.Antoni, C.A.Mathis, B.Lngstrom (2004) *Imaging Brain Amyloid in Alzheimers Disease with Pittsburgh Compound-B.* Annals of Neurolology 55: 306-319.

[18] E.Kandel, J.Schwartz, T.Jessell (2000) *Principles of Neural Science.* Stroke 40: 2601-2606.

[19] Y.Biran, C.L.Masters, K.J.Barnham, A.I.Bush, P.A.Adlard (2009) *Pharmacotherapeutic targets in Alzheimer's disease.* Journal of Cellular and Molecular Medicine 13: 61-86.

[20] M.P.Cuajungco, K.Y.Faget, X.Huang, R.E.Tanzi, A.I.Bush (2000) *Metal chelation as a potential therapy for Alzheimers disease.* Annals of the New York Academy of Sciences 920: 292-304.

[21] P.J.Crouch, L.W.Hung, P.A.Adlard, M.Cortes, V.Lal, G.Filiz, K.A.Perez, M.Nurjono, A.Caragounis, T.Du, K.Laughton, I.Volitakis, A.I.Bush, Q.X.Li, C.L.Masters, R.Cappai, R.A.Cherny, P.S.Donnelly, A.R.White, K.J.Barnham *Increasing Cu bioavailability inhibits Aβ oligomers and tau phosphorylation.* Proceedings of the National Academy of Science 106: 381-386.

[22] J.F.Boas, S.C.Drew, C.C.Curtain (2008) *Applications of electron paramagnetic resonance to studies of neurological disease.* European Biophysics Journal 37: 281-294.

[23] M.A.Lovell, J.D.Robertson, W.J.Teesdale, J.L.Campbell, W.R.Markesbery (1998) *Copper, iron and zinc in Alzheimers disease senile plaques.* Journal of Neurological Science 158: 47-52.

[24] L.M.Miller, Q.Wang, T.P.Telivala, R.J.Smith, A.Lanzirotti, J.Miklossy (2006) *Synchrotron-based infrared and X-ray imaging shows focalized accumulation of Cu and Zn co-localized with β-amyloid deposits in Alzheimer's disease.* Journal of Structural Biology 155: 30-37.

[25] R.A.Cherny, C.S.Atwood, M.E.Xilinas, D.N.Gray, W.D.Jones, C.A.McLean, K.J.Barnham, I.Volitakis, F.W.Fraser, Y.S.Kim, X.Huang, L.E.Goldstein, R.D.Moir, J.T.Lim, K.Beyreuther, H.Zheng, R.E.Tanzi, C.L.Masters, A.I.Bush (2001) *Treatment with a copper-zinc chelator markedly and rapidly inhibits beta-amyloid accumulation in Alzheimers disease transgenic mice* Neuron 30: 665-676.

[26] C.D.Syme, R.C.Nadal, S.E.J.Rigby, J.H.Viles (2004) *Copper binding to the amyloid-beta (Abeta) peptide associated with Alzheimers disease: fold-*

ing, coordination geometry, pH dependence, stoichiometry, and affinity of Abeta-(1-28): insights from a range of complementary spectroscopic techniques. Journal of Biological Chemistry 279: 18169-18177.

[27] S.Zirah, S.A. Kozin, A.K.Mazur, A.Blond, M.Cheminant, I.Segalas-Milazzo, P.Debey, S.Rebuffat (2005) *Structural Changes of Region 116 of the Alzheimer Disease Amyloid-Peptide upon Zinc Binding and in Vitro Aging.* Journal of Biological Chemistry 281: 2151-2161.

[28] C.D.Syme, J.H.Viles (2006) *Solution 1H NMR investigation of Zn^{2+} and Cd^{2+} binding to amyloid-beta peptide (Abeta) of Alzheimers disease* Biochimica Biophysica Acta 1764: 246-256.

[29] Q.F.Ma, J.Hu, W.H.Wu, H.D.Liu, J.D.Du, Y.Fu, Y.W.Wu, P.Lei, Y.F.Zhao, Y.M.Li (2006) *Characterization of copper binding to the peptide amyloid-beta(1-16) associated with Alzheimers disease.* Biopolymers 83: 20-31.

[30] S. Morante (2008) *The role of metals in beta-amyloid peptide aggregation: X-Ray spectroscopy and numerical simulations.* Current Alzheimer Research 5: 508-524.

[31] E.Gaggelli, H.Kozlowski, D.Valensin, G.Valensin (2006) *Copper Homeostasis and Neurodegenerative Disorders (Alzheimers, Prion, and Parkinsons Diseases and Amyotrophic Lateral Sclerosis).* Chemical Reviews 106: 1995-2044.

[32] V.Streltsov (2008) *X-ray absorption and diVraction studies of the metal binding sites in amyloid β-peptide.* European Biophysics Journal 37: 257-263.

[33] V.A.Streltsov, S.J.Titmuss, V.C.Epa, K.J.Barnham, C.L.Masters, J.N.Varghese (2008) *The structure of the Amyloid -peptide high affinity Copper II binding site in Alzheimers Disease.* Biophysical Journal 95: 3447-3456.

[34] J.W.Karr, H.Akintoye, L.J.Kaupp, V.A.Szalai (2005) *N-Terminal Deletions Modify the Cu^{2+} Binding Site in Amyloid-β).* Biochemistry 44: 5478-5487.

[35] T.Kowalik-Jankowska, M.Ruta, K.Wisniewska, L.Lankiewicz (2003) *C oordination abilities of the 116 and 128 fragments of b-amyloid peptide towards copper(II) ions: a combined potentiometric and spectroscopic study.* Journal of Inorganic Biochemistry 95: 270282.

[36] C.C.Curtain, F.Ali, I.Volitakis, R.A.Chernyi, R.S.Norton,K.Beyreuther, C.J.Barrow, C.L.Masters, A.I.Bush, K.J.Barnham (2001) *Alzheimers Disease Amyloid-b Binds Copper and Zinc to Generate an Allosterically Ordered Membrane-penetrating Structure Containing Superoxide Dismutase-like Subunits.* Journal of Biological Chemistry 276: 2046620473.

[37] V.Tougu, A.Karafin, P.Palumaa (2008) *Binding of zinc(II) and copper(II) to the full-length Alzheimers amyloid-b peptide.* Journal of Neurochemistry 104: 12491259.

[38] J.Dong, J.E.Shokes, R.A.Scott, D.G.Lynn (2006) *Modulating Amyloid Self-Assembly and Fibril Morphology with Zn(II).* Journal of the American Chemical Society 128: 3540-3542.

[39] . J.Danielsson, R.Pierattelli, L.Banci, A.Graslund (2007) *High-resolution NMR studies of the zinc-binding site of the Alzheimers amyloid β-peptide.* FEBS Journal 274: 4659.

[40] D.J.Stevens (2008) *Metal binding behavior of the prion protein and relevance to disease progression.* PhD Thesis, Univeristy of California Santa Cruz.

[41] . S.B.Prusiner (1998) *Prions.* In Nobel Lectures: 74-129.

[42] R.A.Moore, L.M.Taubner, S.A.Priola (2009) *Prion protein misfolding and disease.* Current Opinion in Structural Biology 19: 1422.

[43] . J.Collinge, M.Rossor (1996) *A new variant of prion disease.* Lancet 347: 916-917.

[44] F.Guerrieri (2008) *Computer Simulations of Biomolecules: the case of the N-terminal PrP Cu binding site.* PhD Thesis, Univeristy of Roma 'Tor Vergata'.

[45] R.Gabizon, M.P.McKinley, D.Groth, S.B.Prusiner (1988) *Immunoaffinity, Purification and Neutralization of Scrapie Prion Infectivity.* Proceedings of the National Academy Science USA 85: 6617-6621.

[46] K.Basler, B.Oesch, M.Scott, D.Westaway, M.Wlchli, D.F.Groth, M.P.McKinley, S.B.Prusiner, C.Weissmann (1986) *Scrapie and cellular PrP isoforms are encoded by the same chromosomal gene.* Cell 46: 417-428.

[47] K.Pan, M.Baldwin, J.Nguyen, M.Gasset, A.Serban, D.Groth, I.Melhorn, Z.Huang, R.J.Fletterick, F.E.Cohen, S.B.Prusiner (1993) *Conversion of α-helices into β-sheets features in the formation of the scrapie prion proteins.* Proceedings of the National Academy Science USA 90: 10962-10966.

[48] W.Goldmann, N.Hunter, K.T.Martin, M.Dawson, J.Hope (1991) *Different forms of the bovine PrP gene have five or six copies of a short, G-C-rich element within the protein-coding exon.* Journal of General Virology 72: 201-204.

[49] C.Hiraga, A.Kobayashi, T.Kitamoto (2009) *The number of octapeptide repeat affects the expression and conversion of prion protein.* Biochemical and Biophysical Research Communications 382: 715-719.

[50] E.Gaggelli, F.Bernardi, E.Molteni, R.Pogni, D.Valensin, G.Valensin, M.Remelli, M.Luczkowski, H.Kozlowski (2005) *Interaction Of The Human Prion PrP(106-126) Sequence With Copper(II), Manganese(II), And Zinc(II): NMR and EPR Studies.* Journal of the American Chemical Society 127: 996-1006.

[51] G.L.Millhauser (2007) *Copper and the Prion Protein: Methods, Structures, Function, and Disease.* Annual Review of Physical Chemistry 58: 299-320.

[52] S.Simoneau, H,Rezaei, N.Sals, G.Kaiser-Schulz, M.Lefebvre-Roque, C.Vidal, J.Fournier, J.Comte, F.Wopfner, J.Grosclaude, H.Schätzl, C.I.Lasmzas (2007) *In Vitro and In Vivo Neurotoxicity of Prion Protein Oligomers.* PLOS Pathogens 3: 1175-1186.

[53] N.Singh, D.Das, A.Singh, M.L.Mohan (2008) *Prion Protein and Metal Interaction: Physiological and Pathological Implications.* Current Issues of Molecular Biology 12: 99-108.

[54] G.S.Jackson, I.Murray, L.L.Hosszu, N.Gibbs, J.P.Waltho, A.R.Clarke, J.Collinge (2001) *Location and properties of metal-binding sites on the human prion protein.* Proceedings of the National Academy Science USA 98: 8531-8535.

[55] E.D.Walter, D.J.Stevens, M.P.Visconte, G.L.Millhauser (2007) *The Prion Protein is a combined Zinc and Copper binding protein: Zn^{2+} alters the distribution of Cu^{2+} coordination modes.* Journal of the American Chemical Society 129: 15440-15441.

[56] C.S.Burns, E.Aronoff-Spencer, G.Legname, S.B.Prusiner, W.E.Antholine, G.J.Gerfen, J.Peisach, G.L.Millhauser (2003) *Copper coordination in the full-length, recombinant prion protein.* Biochemistry 42: 6794-803.

[57] L.R.Brown, D.A.Harris (2003) *Copper and zinc cause delivery of the prion protein from the plasma membrane to a subset of early endosomes and the Golgi.* Journal of Neurochemistry 87: 353-63.

[58] A.Giese, M.Buchholz, J.Herms, H.A.Kretzschmar (2005) *Mouse brain synaptosomes accumulate copper-67 efficiently by two distinct processes independent of cellular prion protein.* Journal of Molecular Neuroscience 27: 347-54.

[59] J.L.Eriksen, Z.Wszolek, L.Petrucelli (2005) *Molecular Pathogenesis of Parkinson Disease.* Archives of Neurology 62: 353-357.

[60] A.Wood-Kaczmar, S.Gandhi, N.W.Wood (2006) *Understanding the molecular causes of Parkinsons disease.* TRENDS in Molecular Medicine 12: 521-528.

[61] A.J.Lees, J.Hardy, T.Revesz (2009) *Parkinson's Disease.* Lancet 373: 2055-2066.

[62] J.B.Schulz (2008) *Update on the pathogenesis of Parkinson's Disease.* Journal of Neurology 255: 3-7.

[63] B.Thomas, M.F.Beal (2007) *Parkinson's Disease.* Human Molecular Genetics 16: R183-R194.

[64] M.S.Goldberg, P.T.Lansbury (2000) *Is there a cause-and-effect relationship between alpha-synuclein fibrillization and Parkinsons disease?* Nature Cell Biology 2: E115-E119.

[65] G.Prota (1992) *Melanins and Melanogenesis.* Academic Press Inc., San Diego, USA.

[66] H.Fedorow, F.Tribl, G.Halliday, M.Gerlach, P.Riederer, K.L.Double (2005) *Neuromelanin in human dopamine neurons: Comparison with peripheral melanins and relevance to Parkinsons disease* Progress in Neurobiology 75: 109-124.

[67] L.Zecca, R.Fariello, P.Riederer, D.Sulzer, A.Gatti, D.Tampellini (2002) *The absolute concentration of nigral neuromelanin, assayed by a new sensitive method, increases throughout the life and is dramatically decreased in Parkinson's disease.* FEBS Letters 510: 216-220.

[68] L.Zecca, P.Costi, C.Mecacci, S.Ito, M.Terreni, S.Sonnino (2000) *Interaction of Human Substantia Nigra Neuromelanin with Lipids and Peptides.* Journal of Neurochemistry 74: 1758-1765.

[69] L.Zecca, D.Tampellini, M.Gerlach, P.Riederer, R.G.Fariello, D.Sulzer (2001) *Substantia nigra neuromelanin: structure, synthesis, and molecular behaviour.* Journal of Clinical Pathology 54: 414-418.

[70] K.Wakamatsu, K.Fujikawa, F.A.Zucca, L.Zecca, S.Ito (2003) *The structure of neuromelanin as studied by chemical degradative methods.* Journal of Neurochemistry 86: 1015-1023.

[71] M.Fasano, B.Bergamasco, L.Lopiano (2006) *Is neuromelanin changed in Parkinsons disease? Investigations by magnetic spectroscopies.* Journal of Neural Transmission 113: 769-774.

[72] P.R.Crippa, Q.J.Wang, M.Eisner, S.C.Moss, L.Zecca, P.Zachack, T.Gog (1996) *Structure of human neuromelanin by X-ray diffraction:comparison with synthetics.* Pigment Cell Research Supplement 5: 72.

[73] W.D.Bush, J.Garguilo, F.A.Zucca, A.Albertini, L.Zecca, G.S.Edwards, R.J.Nemanich, J.D.Simon (2006) *The surface oxidation potential of human neuromelanin reveals a spherical architecture with a pheomelanin core and a eumelanin surface.* Proceedings of the National Academy of Sciences USA 103: 14785-14789.

[74] J.J.Rehr and R.C.Albers (2000) *Theoretical approaches to x-ray absorption fine structure.* Review of Modern Physics 72: 621-645.

[75] S.Mobilio (2003) *Interaction between radiation and matter: an introduction.* In "Synchrotron Radiation: Fundamentals, Methodologies and Application", SIF Conference Proceedings Vol 82.

[76] Y.Joly (2001) *X-ray absorption near edge structure calculations beyond the muffin-tin approximation.* Physical Review B 63: 125120-125129.

[77] J.G.Norman (1976) *Non-empirical versus empirical choices for overlapping-sphere radii ratios in SCF-Xα-SW calculations on ClO_4^- and SO_2.* Molecular Physics 31: 1191-1198.

[78] J.J.Boland, S.E.Crane, J.D.Baldeschwieler (1982) *Theory of extended X-ray absorption fine structure: single and multiple scattering formalism.* Journal of Chemical Physics 77: 142-153.

[79] E.A.Stern (1988) *Theory of EXAFS.* In X-ray Absorption, D.C.Koningsberger and R.Prins editors, Chemical Analysis 92, Wiley Interscience.

[80] N.Dimakis,M.AI-Akhras, G.Bunker (1999) *Rapid single- and multiple-scattering EXAFS Debye-Waller factor calculations on active sites of metalloproteins.* Journal of Synchrotron Radiation 6: 266-267.

[81] N.Dimakis, G.Bunker (2006) *Ab Initio Self-Consistent X-Ray Absorption Fine Structure Analysis for Metalloproteins.* Biophysical Journal: Biophysical Letters L87-L89.

[82] S.Mobilio and A.Balerna (2003) *Introduction to the main properties of Synchrotron Radiation.* In "Synchrotron Radiation: Fundamentals, Methodologies and Application", SIF Conference Proceedings Vol 82.

[83] H.N.Chapman, A.Barty, M.J.Bogan, S.Boutet, M.Frank, S.P.Hau-Riege, S.Marchesini, B.W.Woods, S.Bajt, W.H.Benner, R.A.London, E.Plönjes, M.Kuhlmann, R.Treusch, S.Düsterer, T.Tschentscher, J.R.Schneider, E.Spiller, T.Möller, C. Bostedt, M.Hoener, D.A.Shapiro, K.O.Hodgson, D.Van Der Spoel, F.Burmeister, M.Bergh, C.Calenab, G.Huldt, M.M.Seibert, F.R.N.C.Maia, R.W.Lee, A.Szöke, N.Timneanu, J.Hajdu (2006) *Femtosecond diffractive imaging with a soft-X-ray free-electron laser.* Nature Physics 2: 839-843.

[84] H.N.Chapman (2009) *X-ray imaging beyond the limits.* Nature Materials 8: 299-301.

[85] G.Margaritondo, Y.Hwu, G.Tromba (2003) *Synchrotron Light: from basics to coherence and coherence-related applications* In "Synchrotron Radiation: Fundamentals, Methodologies and Application", SIF Conference Proceedings Vol 82.

[86] P.Fornasini (2003) *Introduction to X-ray absorption spectroscopy.* In "Synchrotron Radiation: Fundamentals, Methodologies and Application", SIF Conference Proceedings Vol 82.

[87] *X-ray Data Booklet.* http://xdb.lbl.gov/

[88] P.A.Lee, P.H.Citrin, P.Eisenberg, B.M.Kincaid (1981) *Extended X-ray absorption fine structure - its strenghts and limitations as a structural tool.* Reviews of Modern Physics 53: 769-806.

[89] S.Morante *X-ray Absorption Spectroscopy: a powerful tool for the investigation of the role of metals in promoting activation and aggregation of biological molecules.* PhD school lectures, University of Rome "Tor Vergata".

[90] T.M.Hayes and J.B.Boyce (1982) In H.Ehrenreich, F.Seitz, D.Turnbull (Academic, New York). Solid State Physics, 37: 173.

[91] B.Ravel (2008) *ATHENA user's guide.* http://cars9.uchicago.edu/ ravel/software/exafs/.

[92] M.Benfatto, A.Congiu-Castellano, A.Daniele, S.Della Longa (2001) *MXAN: a new software procedure to perform geometrical fitting of experimental XANES (X-ray Absorption Near Edge Structure) spectra.* Journal of Synchrotron Radiation 8: 267-269.

[93] A.L.Ankudinov, B.Ravel, J.J.Rehr, S.D.Conradson (1998) *Real Space Multiple Scattering Calculation of XANES.* Physical Review B 58: 7565-7576.

[94] M.Benfatto, S.Della Longa, Y.Qin, Q.Li, G.Pan, Z.Wu, S.Morante (2004) *The role of Zn in the interplay among Langmuir-Blodgettmultilayer and myelin basic protein: a quantitative analysis of XANES spectra.* Biophysical Chemistry 110: 191-201.

[95] P.Frank, K.O. Hodgson (2000) *Defining Chemical Species in Complex Environments Using K-Edge X-ray Absorption Spectroscopy: Vanadium in Intact Blood Cells and Henze Solution from the Tunicate Ascidia ceratodes.* Inorganic Chemistry 39: 6018-6027.

[96] G.Smolentsev, A.Soldatov (2006) *Quantitative local structure refinement from XANES: multi-dimensional interpolation approach.* Journal of Synchrotron Radiation 13: 1929.

[97] B.K.Teo (1981) *Novel method for angle determinations by EXAFS via a new multiple-scattering formalism.* Journal of the American Chemical Society 103: 3990-4001.

[98] A.Filipponi, A.Di Cicco, T.A.Tyson, C.R.Natoli (1991) *Ab-initio modelling of X-ray Absorption spectra.* Solid State Communication 78: 265-268.

[99] N.Binsted (1998) *EXCURV98: CCLRC Daresbury Laboratory computer program.* CCLRC Daresbury Laboratory, Warrington, Cheshire, UK.

[100] N.Binsted, R.W.Strange, S.S.Hasnain (1992) *Constrained and restrained refinement in EXAFS data analysis with curved wave theory.* Biochemistry 31: 12117-12125.

[101] N.J.Blackburn, S.S.Hasnain, G.P.Diakun, P.F.Knowles, N.Binsted, C.D.Garner (1983) *An extended x-ray absorption fine structure study of the copper and zinc sites of freeze-dried bovine superoxide dismutase* Biochemical Journal 213: 765-768.

[102] S.Morante, R.Gonzalez-Iglesias, C.Potrich, C.Meneghini, W.Meyer-Klaucke, G.Menestrina, M.Gasset (2004) *Inter- and intra-octarepeat Cu(II) site geometries in the prion protein: implications in Cu(II) binding cooperativity and Cu(II)-mediated assemblies.* Journal of Biological Chemistry 279: 11753-11759.

[103] L.Redecke, W.Meyer-Klaucke, M.Koker, J.Clos, D.Georgieva, N.Genov, H.Echner, H.Kalbacher, M.Perbandt, R.Bredehorst, W.Vlter, C.Betzel (2005) *Comparative analysis of the human and chicken prion protein copper binding regions at pH 6.5.* Journal of Biological Chemistry 280: 13987-13992.

[104] C.Meneghini, S.Morante (1998) *The active site structure of tetanus neurotoxin resolved by multiple scattering analysis in X-Ray absorption spectroscopy.* Biophysical Journal 75: 1953-1963.

[105] B.K.Teo, P.A.Lee PA (1979) *Ab initio calculations of amplitude and phase functions for extended X-ray absorption fine structure spectroscopy.* Journal of the American Chemical Society 101: 2815-2832.

[106] G.C.Ferreira, R.Franco, A.Mangravita, G.N. George (2002) *Unraveling the Substrate-Metal Binding Site of Ferrochelatase: An X-ray Absorption Spectroscopic Study.* Biochemistry 41: 4809-4818.

[107] V.Minicozzi, F.Stellato, M.Comai, M. Dalla Serra, C.Potrich, W.Meyer-Klaucke, S.Morante (2008) *Identifying the Minimal Cu and Zn Binding Site Sequence in Amyloid Beta Peptides.* Journal of Biological Chemistry 283: 10784-10792.

[108] Y.Yoshiike, K.Tanemura, O.Murayama, T.Akagi, M.Murayama, S.Sato, X.Sun, N.Tanaka, A.Takashima (2001) *New Insights on How Metals Disrupt Amyloid beta - Aggregation and Their Effects on Amyloid-beta Cytotoxicity.* Journal of Biological Chemistry 276: 32293-32299.

[109] V.P.S.Chauhan, A.Chauhan, J.Wegiel (2001) *Fibrillar amyloid beta-protein forms a membrane-like hydrophobic domain.* Neuroreport 12: 587-590.

[110] R.Squitti, P.M.Rossini, E.Cassetta, F.Moffa, P.Pasqualetti, M.Cortesi, A.Colloca, L.Rossi, A.FinazziAgr (2002) *D-penicillamine reduces serum oxidative stress in Alzheimer's disease patients.* European Journal of Clinical Investigation 32: 51-59.

[111] G.Menestrina, V.Cabiaux, M.Tejuca (1999) *Secondary structure of sea anemone cytolysins in soluble and membrane bound form by infrared spectroscopy.* Biochemical and Biophysical Research Communications 254: 174-180.

[112] M.Korbas, D.Fulla Marsa, W.Meyer-Klaucke (2006) *KEMP: A program script for automated biological x-ray absorption spectroscopy data reduction.* Review of Scientific Instruments 77: 063105.

[113] H.M.Berman, J.Westbrook, Z.Feng, G.Gilliland, T.N.Bhat, H.Weissig, I.N.Shindyalov, P.E.Bourne (2000) *The Protein Data Bank.* Nucleic Acids Research 28:235242.

[114] J.M.Castagnetto, S.W.Hennessy, V.A.Roberts, E.D.Getzoff, J.A.Tainer, M.E.Pique (2002) *MDB: the Metalloprotein Database and Browser at The Scripps Research Institute.* Nucleic Acids Research 30: 379382.

[115] N.Binsted, R.W.Strange, S.S.Hasnain (1992) *Constrained and restrained refinement in EXAFS data analysis with curved wave theory.* Biochemistry 31: 12117-12125.

[116] F.Stellato, G.Menestrina, M.Dalla Serra, C.Potrich, R.Tomazzolli, W.Meyer-Klaucke, S.Morante (2006) *Metal binding in amyloids beta peptides shows both intra- and inter-peptide model.* European Biophysical Journal 35: 340-351.

[117] T.Miura, K.Suzuki, N.Kohata, H.Takeuchi (2000) *Metal binding modes of Alzheimers amyloid b-peptide in insoluble aggregates and soluble complexes.* Biochemistry 39: 7024-7031.

[118] C.R.Natoli, M.Benfatto (1986) *A unifying scheme of interpretation of X-ray absorption spectra based on multiple scattering theory.* Journal de Physique Colloques (France) 47:C811-C823.

[119] T.A.Tyson, K.O.Hodgson, C.R.Natoli, M.Benfatto (1992) *General multiple-scattering scheme for the computation and interpretation of x-ray-absorption fine structure in atomic clusters with applications to SF6, GeCl4, and Br2 molecules.* Physical Review B 46:5997-6019.

[120] V.Minicozzi, S.Morante, G.C.Rossi, F.Stellato, N. Christian, K. Jansen (2008) *The role of metals in aggregation. Experiments and ab initio simulations.* International Journal of Quantum Chemistry 108: 1992-2015.

[121] M.Chattopadhyay, E.D.Walter, D.J.Newell, P.J.Jackson, E.Aronoff-Spencer, J.Peisach, G.J.Gerfen, B.Bennett, W.E.Antholine, G.L.Millhauser (2005) *The octarepeat domain of the prion protein binds Cu(II) with three distinct coordination modes at pH 7.4.* Journal of the American Chemical Society 127: 12647-12656.

[122] O.Proux, X.Biquard, E.Lahera, J.J.Menthonnex, A.Prat, O.Ulrich, Y.Soldo, P.Trvisson, G.Kapoujvan, G.Perroux, P.Taunier, D.Grand, P.Jeantet, M.Deleglise, J.P.Roux, J.L.Hazemann (2005) *FAME: A new beamline for X-ray absorption investigations of very-diluted systems of environmental, material and biological interests.* Physica Scripta 115: 970-973.

[123] O.Proux, V.Nassif, A.Prat, O.Ulrich, E.Lahera, X.Biquard, J.J.Menthonnex, J.L.Hazemann (2005) *Feedback system of a liquid*

nitrogen cooled double-crystal monochromator: design and performances. Journal of Synchrotron Radiatiation 13: 59-68.

[124] C.S.Burns, E.Aronoff-Spencer, C.M.Dunham, P.Lario, N.I.Avdievich, W.E.Antholine, M.M.Olmstead, A.Vrielink, G.J.Gerfen, J.Peisach, W.G.Scott, G.L.Millhauser (2002) *Molecular Features of the Copper Binding Sites in the Octarepeat Domain of the Prion Protein.* Biochemistry 41: 3991-4001.

[125] P.R.Crippa, M.Eisner, S.Morante, F.Stellato, F.C.Vicentin, L.Zecca (2009) *A XAS Study of the Sulphur Environment in Human Neuromelanin and its Synthetic Analogues.* European Biophysical Journal, DOI: 10.1007/s00249-009-0462-9.

[126] H.Ebel (2004) *Quantitative analysis by X-ray induced total electron yield (TEY) compared to XRFA.* Powder Diffraction 19:90-96.

[127] M.E.Fleet (2005) *XANES spectroscopy of sulphur in Earth materials.* Canadian Mineralogy 43: 1811-1838.

[128] J.Stohr, C.Noguera, T.Kendelewicz (1984) *Auger and photoelectron contributions to the electron-yield surface extended X-ray absorption fine-structure signal.* Physical Review B 30: 5571-5579.

[129] D.Vlachos, A.J.Craven, D.W.McComb (2005) *Specimen charging in X-ray absorption spectroscopy: correction of total electron yield data from stabilized zirconia in the energy range 250915 eV.* Journal of Synchrotron Radiation 12: 224-233.

[130] J.Prietzel, J.Thieme, U.Neuhausler, J.Susini, I.Kogel-Knabner (2003) *Speciation of sulphur in soils and soil particles by X-ray spectroscopy.* European Journal of Soil Science 54: 423-433.

[131] G.N.George, M.L.Gorbaty (1989) *Sulphur K-edge X-ray absorption spectroscopy of petroleum asphaltenes and model compounds.* Journal of the American Chemical Society 111: 3182-3186.

[132] T.Ye, L.E.Lamb, K.Wakamatsu, S.Ito, J.D.Simon (2003) *Ultrafast absorption and photothermal studies of trichochrome C in solution.* Photochemical and Photobiological Sciences 2: 821-823.

[133] S.M.Heald (1988) In X-ray Absorption, D.C.Koningsberger and R.Prins editors, Chemical Analysis 92, Wiley Interscience.

[134] I.J.Pickering, R.C.Prince, T.Divers, G.N.George (1998) *Sulfur K-edge X-ray absorption spectroscopy for determining the chemical speciation of sulfur in biological systems.* FEBS Letters 441: 11-14.

[135] G.Odh, R.Carstam, J.Paulson, A.Wittbjer, E.Rosengren, H.Rorsman (1994) *Neuromelanin of the human substantia nigra: a mixed type melanin.* Journal of Neurochemistry 62: 2030-2036.

[136] R.Besio, S.Alleva, A.Forlino, A.Lupi, C.Meneghini, V.Minicozzi, A.Profumo, F.Stellato, R.Tenni, S.Morante (2009) *Identifying the structure of the active sites of human recombinant prolidase.* European Biophysical Journal, DOI: 10.1007/s00249-009-0459-4.

[137] P.M.Royce, B.Steinmann (2002) *Prolidase deficiency.* In Connective tissue and its heritable disorders, Wiley-Liss, New York, USA.

[138] A.Lupi, R.Tenni, A.Rossi, G.Cetta, A.Forlino (2008) *Human prolidase and prolidase deficiency: an overview on the characterization of the enzyme involved in proline recycling and on the effects of its mutations.* Amino Acids 35: 739-752.

[139] M.J.Maher, M.Ghosh, A.M.Grunden, A.L.Menon, M.W.Adams, H.C.Freeman, J.M.Guss (2004) *Structure of the prolidase from Pyrococcus furiosus.* Biochemistry 43: 2771-2783.

[140] W.T.Lowther, B.W.Matthews (2002) *Metalloaminopeptidases: common functional themes in disparate structural surroundings.* Chemical Reviews 102: 4581-4608.

[141] T.H.Tahirov, H.Oki, T.Tsukihara, K.Ogasahara, K.Yutani, K.Ogata, Y.Izu, S.Tsunasawa, I.Kato (1998) *Crystal structure of methionine*

aminopeptidase from hyperthermophile, Pyrococcus furiosus. Journal of Molecular Biology 284: 101-124.

[142] X.Du, S.Tove, K.Kast-Hutcheson, A.M.Grunden (2005) *Characterization of the dinuclear metal center of Pyrococcus furiosus prolidase by analysis of targeted mutants.* FEBS Letters 579: 6140-6146.

[143] A.Lupi, S.Della Torre, E.Campari, R.Tenni, G.Cetta, A.Rossi, A.Forlino (2006) *Human recombinant prolidase from eukaryotic and prokaryotic sources Expression, purification, characterization and long-term stability studies.* FEBS Journal 273: 5466-5478.

[144] O.H.Lowry, N.J.Rosebrough, A.L.Farr, R.J.Randall (1951) *Protein measurement with the folin phenol reagent.* Journal of Biological Chemistry 193: 265-275.

[145] A.Lupi, R.Tenni, A.Rossi, G.Cetta, A.Forlino (2008) *Human prolidase and prolidase deficiency: an overview on the characterization of the enzyme involved in proline recycling and on the effects of its mutations.* Amino Acids 35: 739-752.

[146] I.Myara, C.Charpentier, A.Lemonnier (1982) *Optimal conditions for prolidase assay by proline calorimetric determination: application to iminodipeptiduria.* Clinica Chimica Acta 125: 193-205.

[147] http://webusers.fis.uniroma3.it/meneghini/

[148] S.I.Zabinsky, J.J.Rehr, A.Ankudinov, R.C.Albers, M.J.Eller (1995) *Multiple scattering calculations of X-ray absorption spectra.* Physical Review B 52: 2995-3009.

[149] F.James (1994) *MINUIT: function minimization and error analysis reference manual version 94.1.* CERN Program Library D506.

[150] K.Willingham, M.J.Maher, A.M.Grunden, M.Ghosh, M.W.Adams, H.C.Freeman, J.M.Guss (2001) *Crystallization and characterization of the prolidase from Pyrococcus furiosus.* Acta Crystallographica D Biological Crystallography 57: 428-430.

[151] E.T.Parkin, N.T.Watt, I.Hussain, E.A.Eckman, C.B.Eckman, J.C.Manson, H.N.Baybutt, A.J.Turner, N.M.Hooper (2007) *Cellular prion protein regulates β-secretase cleavage of the Alzheimers amyloid precursor protein.* Prion 3 [Epub ahead of print]. Proceedings of the National Academy of Science 104: 11062-11067.

[152] K.A.Kellett, N.M.Hooper (2009) *Prion protein and Alzheimer disease.* Prion 3 [Epub ahead of print].

[153] K.J.Barnham, R.Cappai, K.Beyreuther, C.L.Masters, A.F.Hill (2006) *Delineating common molecular mechanisms in Alzheimers and prion diseases.* TRENDS in Biochemical Sciences 31: 465-472.

[154] K.S.J.Rao, M.L.Hegde, S.Anitha, M.Musicco, F.A.Zucca, N.J.Turro, L.Zecca (2006) *Amyloid β and neuromelaninToxic or protective molecules? The cellular context makes the difference.* Progress in Neurobiology 78: 364-373.

[155] D.Drago, M.Bettella, S.Bolognin, L.Cendron, J.Scancar, R.Milacic, F.Ricchelli, A.Casini, L.Messori, G.Tognon, P.Zatta (2008) *Potential pathogenic role of β-amyloid(1-42)aluminum complex in Alzheimers disease.* The International Journal of Biochemistry and Cell Biology 40: 731-746.

[156] J.R.Walton (2006) *Aluminum in hippocampal neurons from humans with Alzheimer's disease.* NeuroToxicology 27: 385-394.

[157] P.Zatta, R.Lucchini, S.J. van Rensburg, A.Taylor (2003) *The role of metals in neurodegenerative processes: aluminum, manganese, and zinc.* Brain Research Bullettin 62: 15-28.